University of Nevada, Reno

Thermal Infrared Radiative Forcing By Atmospheric Aerosol

A dissertation submitted in partial fulfillment of
the requirements for the degree of Doctor of
Philosophy in Physics

By

Narayan Adhikari

William P. Arnott, Ph. D. /Dissertation Advisor

August, 2014

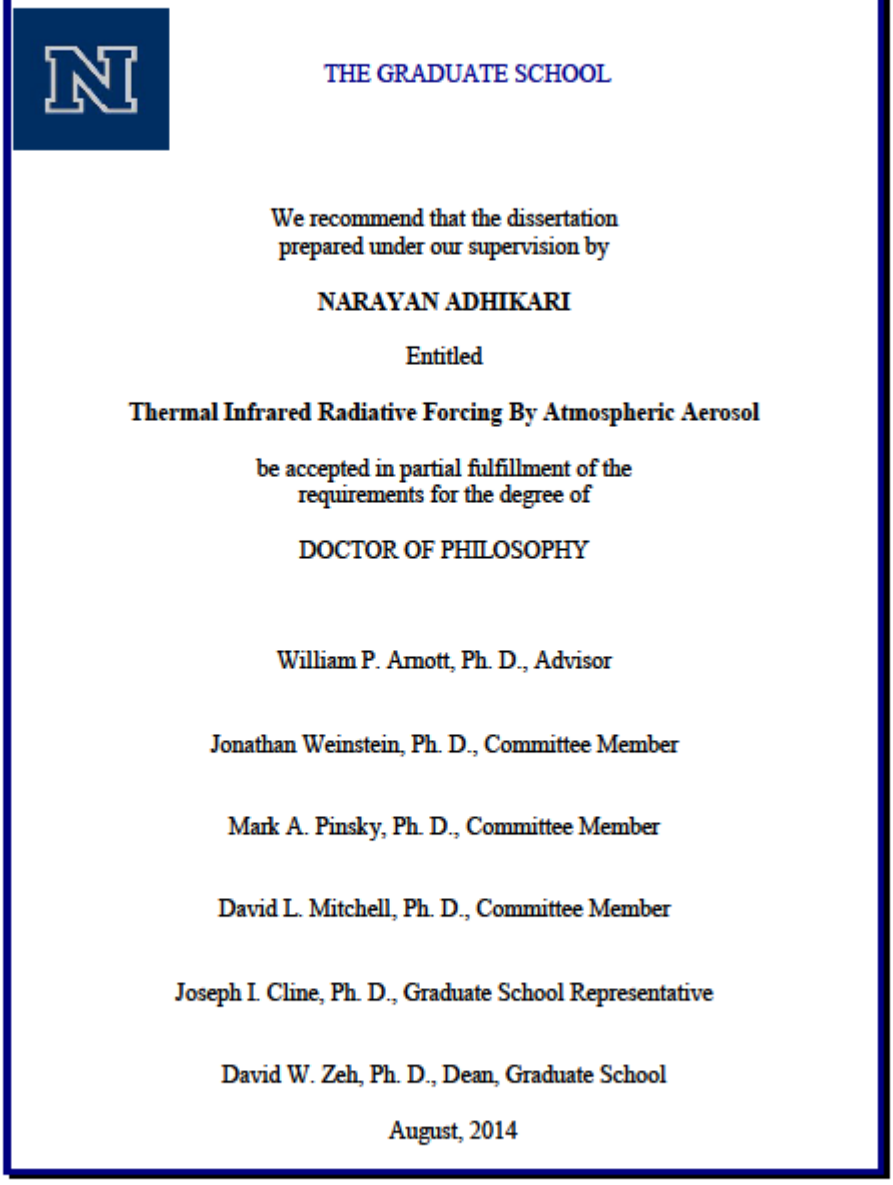

THE GRADUATE SCHOOL

We recommend that the dissertation
prepared under our supervision by

NARAYAN ADHIKARI

Entitled

Thermal Infrared Radiative Forcing By Atmospheric Aerosol

be accepted in partial fulfillment of the
requirements for the degree of

DOCTOR OF PHILOSOPHY

William P. Arnott, Ph. D., Advisor

Jonathan Weinstein, Ph. D., Committee Member

Mark A. Pinsky, Ph. D., Committee Member

David L. Mitchell, Ph. D., Committee Member

Joseph I. Cline, Ph. D., Graduate School Representative

David W. Zeh, Ph. D., Dean, Graduate School

August, 2014

Abstract

The work mainly focuses on the study of thermal infrared (IR) properties of atmospheric greenhouse gases and aerosols, and the estimation of the aerosol-induced direct longwave (LW) radiative forcing in the spectral region 5-20 μm at the Earth's surface (BOA; bottom of the atmosphere) and the top of the atmosphere (TOA) in cloud-free atmospheric conditions. These objectives were accomplished by conducting case studies on clear sky, smoky, and dusty conditions that took place in the Great Basin of the USA in 2013. Both the solar and thermal IR measurements and a state-of-the-science radiative transfer model, the LBLDIS, a combination of the Line-By-Line Radiative Transfer Model and the Discrete Ordinate Radiative Transfer (DISORT) solver were employed for the study. The LW aerosol forcing is often not included in climate models because the aerosol effect on the LW is often assumed to be negligible. We lack knowledge of aerosol characteristics in the LW region, and aerosol properties exhibit high variability. We have found that the LW TOA radiative forcing due to fine mode aerosols, mainly associated with small biomass burning smoke particles, is + 0.4 W/m^2 which seems to be small, but it is similar to the LW radiative forcing due to increase in CO_2 concentration in the Earth's atmosphere since the preindustrial era of 1750 (+ 1.6 W/m^2). The LW radiative forcing due to coarse mode aerosols, associated with large airborne mineral dust particles, was found to be as much as + 5.02 W/m^2 at the surface and + 1.71 W/m^2 at the TOA. All of these significant positive values of the aerosol radiative forcing both at the BOA and TOA indicate that the aerosols have a heating effect in the LW range, which contributes to counterbalancing the cooling effect associated with the aerosol radiative forcing in the shortwave (SW) spectral region. In the meantime, we have found that LW radiative forcing by aerosols is highly sensitive to particle size and complex refractive indices of the aerosol constituents.

We have also demonstrated that LW aerosol radiative forcing is somewhat sensitive to the water vapor content in the atmosphere, and increases with the dryness of the atmosphere. This evidence supports our argument that the Great Basin area of the USA, which usually has extremely dry atmospheric conditions, can be an appropriate place to study the dry-desert aerosol climate forcing in a regional scale.

An analysis of aerosol IR backscattering shows that the effect significantly contributes to both the BOA and TOA IR forcings, even if the aerosols do not exhibit absorption at all in the thermal IR. The general LW radiative forcing is, therefore, associated with both the absorption and scattering effects of the aerosols. Neglecting LW scattering will result in an underestimation of LW radiative forcing by aerosols.

Finally, the discrepancy between the FTIR-observed and modeled radiance with aerosols indicates a significant uncertainty, which demands further research on the LW optical properties of fine and coarse mode aerosol.

Acknowledgement

It is my great pleasure to offer my deepest gratitude to my supervisor W. Patrick Arnott, whose relentless guidance, encouragement, and support throughout the extent of this project has made this work successful.

I would like to thank my committee members for serving on my committee and the invaluable time and guidance they have provided during my final progression toward graduation.

I highly acknowledge my teachers, colleagues, friends, the staff at the University of Nevada, Reno (UNR), and well-wishers around the world for their kind cooperation and well wishes. I appreciate the Department of Physics at UNR for the financial support during my study.

I am indebted to the Atmospheric & Environmental Research (AER) Radiative Transfer Working Group, especially Matthew Alvarado and Karen Cady-Pereira, who helped me for using the LBLRTM. I would like to thank David D. Turner and Aronne Merrelli for their great cooperation for setting up and running the LBLDIS.

I am grateful to my parents and grandparents who are, in fact, a great source of inspiration for my every academic achievement.

Most of all, I heartily honor my wonderful wife, Saru, who sacrificed her every precious moment and personal desire for the sake of my study. I would like to express my deep compassion for my lovely sons, Vision and Angeles, who were deprived of great moments with me during the project.

Table of Contents

List of Tables

List of Figures

1 INTRODUCTION

1.1 General overview of infrared and aerosol issues

Electromagnetic radiation is the vital player in the Earth's radiative energy budget. Radiation is broadly categorized into two portions, shortwave (solar) and longwave (terrestrial) radiation. The shortwave (SW) radiation lies in the wavelength range 0.1-4 μm and longwave (LW) in the range 4-100 μm. The latter is also referred to as thermal infrared (IR). Over 99% of the radiative energy emitted by the sun (6000 K) that is incident on the top of the Earth's atmosphere (TOA) lies in the SW band. On the other hand, over 99% of the radiative energy emitted by the Earth-atmosphere system (280 K) lies in the LW band (Petty 2006). The Earth's surface and atmosphere absorb both the SW and LW radiation, but emits only LW radiation. Trace gases in the atmosphere such as CO_2, H_2O, CH_4, and O_3 which are called greenhouse gases, mainly absorb and emit in the LW region. Atmospheric particles such as clouds and aerosols absorb and scatter both LW and SW radiation, but emit only LW radiation.

Aerosols are tiny solid or liquid particles suspended in the air, which typically range in size from a few nanometers (nm) to tens of micrometers (μm) in diameter (Seinfeld and Pandis 2006). Examples of aerosols include airborne mineral dust, biomass burning smoke, soot, ashes, sulfates, nitrates, etc. The fine mode aerosol particles such as biomass burning smoke, soot and pollution have sizes less than 1 μm and the coarse mode aerosols such as sea-salts and mineral dust have sizes greater than 1 μm. The coarse mode particles have substantial influence on the radiative fluxes in the LW spectral domain.

The balance between the incoming SW radiation absorbed by the Earth's surface and the atmosphere and the outgoing LW radiation from the atmosphere determine the surface radiative energy budget. For example the net flux F_{net} at the Earth's surface is given by

$$F_{net} = (F_s + F_{ld}) - (AF_s + F_{lu}) \tag{1.1}$$

where F_s , F_{ld}, and F_{lu} are the incoming SW radiative flux, downwelling LW radiative flux, and upwelling LW radiative flux, respectively, and A is the Earth's surface albedo. The radiative fluxes F_{ld} and F_{lu} depend on the amount of greenhouse gases, clouds, and aerosols present in the atmosphere. F_{lu} further strongly depends on the temperature and emissivity of the Earth's surface. Owing to invariability (in terms of structure, composition, and concentration) of the greenhouse gases over time and space, their contribution to the LW fluxes are reasonably well known (Raymond et al. 2009). On the contrary, the contribution of the atmospheric aerosols to the total LW fluxes possesses significant uncertainties due to their highly variable properties (Ge et al. 2010). According to Inter-governmental Panel on Climate Change (IPCC) 2013 report, atmospheric aerosols contribute the largest uncertainty to the estimate of the Earth's changing energy budget, the balance between the incoming solar and outgoing infrared (thermal) radiation from the Earth-atmosphere system. In this dissertation, we use the term 'aerosol radiative forcing' to indicate the difference of fluxes with and without aerosol.

Despite the fact that aerosols can have a large impact on the LW radiative fluxes, aerosol radiative forcing in the LW is not generally included in many climate models (Vogelmann et al. 2003). Though some regional and global scale climate models consider the aerosol radiative effect in the LW spectral domain, only the absorption is taken into account while scattering is still neglected (Dufresne et al. 2002). The large, highly scattering and absorbing aerosols in the LW region can influence local climate features, as well as the global radiation budget (Tegen et al. 1996). Due to a lack of enough knowledge of the LW aerosol properties and difficulties to accurately parameterize the aerosol model, very few studies have been done on aerosol LW radiative forcing (Sicard et al. 2014). Since aerosol LW radiative effect is assumed to be negligible and it involves many uncertainties, most of the works on aerosol radiative forcing have been limited to the SW spectral domain (Markowicz et al. 2003). Even though radiative forcing of the fine mode aerosols is usually small in the LW as compared to their forcing in the SW,

strongly absorbing and scattering coarse mode aerosols have a significant forcing in the LW (Fouquart et al. 1987).

These illustrations motivated us to study the LW radiative effect of the aerosols. The primary objectives of this research are two-fold: to study the optical properties of the aerosols such as biomass burning smoke and mineral desert dust particles, and to quantify their LW radiative forcing in the thermal IR radiation (5-20 μm). Reno, located at 39.527°N and 119.822° W, in the Great Basin of the USA, observed a big biomass burning smoke aerosol from the California Rim Fire in August 2013, and an episode of a large dust outbreak on 24 April 2013. We argue that the dry-desert area of the Great Basin can be an appropriate place for studying the aerosol radiative forcing due to three reasons: First, the Great Basin observes coarse mode particles almost every day and these particles offer non-negligible LW radiative forcing. Dust consists of the major portion of aerosol mass loading, particularly, in near deserts and arid/semi-arid areas (Yang et al. 2007). Second, this area occasionally observes heavy smoke from California wildfires and dust storms during summer and late spring due to its hot and dry conditions. Third, a higher relative humidity can modify the size distribution and refractive index of both water soluble and insoluble components of aerosols: water soluble constituents may undergo particle growth and transformation to an aqueous solution, while water insoluble constituents undergo coating with liquid water or aqueous solution of any soluble components. Due to these effects, the aerosol optical properties (extinction efficiency, single scatter albedo, asymmetry parameter, etc.) and hence the radiative properties (radiative flux) depend significantly on relative humidity (Lubin et al. 2002). Thus taking account of the effect of humidity causes the modeling of the aerosols to become more complex, difficult, as well as erroneous. Also, the radiative forcing of the aerosols is stronger in the drier atmosphere (Liao and Seinfeld 1998). These facts imply that the dry atmospheric condition of the Great Basin can be highly favorable for characterizing the radiative properties of dry-aerosols.

We also present an analysis on the aerosol backscatter of the thermal IR and its influence on the radiative forcing. Such an effect is not yet widely accepted by climate scientists as being important in the thermal IR region.

1.2 Organization of dissertation

The dissertation is structured as follows: Chapter 2 presents the theoretical analysis of aerosol microphysical and optical properties. Chapter 3 describes the instruments and experimental techniques. Radiative transfer models are discussed in Chapter 4. Case studies for dry and clear sky, and smoky and dusty atmospheres are presented in Chapters 5 through 7. The final Chapter presents overall discussion, conclusions, and suggestions for future work.

2 THEORETICAL ANALYSES OF AEROSOL MICROPHYSICAL AND OPTICAL PROPERTIES

2.1 Size distribution function

The size of particles in the atmosphere usually spans a wide range, which results in a large standard deviation in the normal (Gaussian) distribution for fit of the observed particle sizes. Aerosol size distributions are represented by a normal distribution of the logarithm of the particle radii, called lognormal distribution, in which the natural logarithm of radii is normally distributed (Levoni et al. 1997). The lognormal columnar volume size distribution function $\frac{dV(r)}{d\,lnr}$ is given by (Schuster et al. 2006)

$$\frac{dV(r)}{d\,lnr} = \frac{C}{\sqrt{2\pi}}\frac{1}{lnS}\exp\left[-\frac{(\ln r - lnr_m)^2}{2(lnS)^2}\right], \quad (2.1)$$

where C represents the column volume of all particles per cross-section of atmospheric column which is obtained by integrating $\frac{dV(r)}{d\,lnr}$ over all sizes i.e.

$$C = \int_{r_{min}}^{r_{max}} \frac{dV(r)}{d\,lnr} dlnr. \quad (2.2)$$

This parameter C controls the overall scaling of the distribution. The quantity $\frac{dV(r)}{d\,lnr}$ is normalized if C = 1.0. r_m is the volume median, or modal radius; half the particles are smaller and half larger than r_m. The modal radius is the radius of maximum frequency of the distribution. The median and modal radii are identical for lognormal distributions. S is called the geometric standard deviation, which is related to the standard deviation σ of the natural logarithm of the radius lnr (i.e. the radius in log space) by $S = e^{\sigma}$. The dimensionless quantity S gives the spread (or width) of the distribution. The parameters r_m and S are constants for a given size distribution. The values of S (must be ≥ 1) lie in the range 1.5-2.5 for realistic atmospheric aerosols (Zender 2010). For monodisperse particles, S ≈ 1. The factor $\sqrt{2\pi}$ on the denominator comes from the normalization

property of the Gaussian function i.e., $\int_{-\infty}^{+\infty} \exp\left(-\frac{x^2}{2}\right) dx = \sqrt{2\pi}$. The common units for the volume distribution dV/dlnr are $\mu m^3\ \mu m^{-2}$. The reason behind the use of volume concentration is that the optical effects of atmospheric aerosols are more related to their volume rather than their number (Whitby 1978).

The columnar particle number size distribution n(r) in the units of number of particles per unit area per size interval in the whole atmosphere column is given by

$$n(r) = \int_0^z N(r,z)dz, \tag{2.3}$$

where $N(r,z)$ is the local number concentration (number per unit volume) per size interval. Assuming spherical particles, we have

$$\frac{\text{total particle volume}}{\text{area of air}} = \int_{r_{min}}^{r_{max}} \frac{dV(r)}{dlnr}\, dlnr = \int_{r_{min}}^{r_{max}} \frac{4}{3}\pi r^3 n(r)dr = \int_{r_{min}}^{r_{max}} \frac{1}{r}\frac{dV(r)}{dlnr}\, dr. \tag{2.4}$$

Hence, $n(r)$ is related to the volume size distribution observed by an AERONET Cimel sun-photometer as (Sayer et al. 2012)

$$n(r) = \frac{3}{4\pi r^4}\frac{dV(r)}{dlnr}. \tag{2.5}$$

Eq. 2.5 is used to integrate the individual particle single scattering properties derived from the Mie theory for spherical homogeneous particles (Bohren and Hoffman 1983), or other for non-spherical particles.

Fig. 2.1 depicts examples of measured aerosol bimodal lognormal volume size distributions at the University of Nevada, Reno (UNR), which consist of fine and coarse mode aerosols. The bimodal size distribution can be given by a linear combination of two lognormal functions given

by Eq. 2.1 for fine and coarse modes. Fig. 2.1 (left) is a size distribution for a smoke event in Reno on 26 August 2013 at 17:00 Local Standard Time (LST) measured with AERONET (aerosol robotic network) Cimel sun-photometer. The strong predominance of the fine mode implies the presence of small smoke particles. Fig. 2.1 (right) is the aerosol size distribution derived from the MFRSR (multi-filter rotating shadow-band radiometer) data on 24 April 2013 at 14:29 LST during a dust-storm event in Reno. The strong predominating feature of the coarse mode particles over fine (or accumulation) mode is a typical characteristic of a dust outbreak episode (Sicard et al. 2014). The volumetric parameters such as volume median radius, standard deviation and volume concentration for each mode of both dates are reported in Table 2.1. The values of the standard deviation are taken to be 0.42 and 0.61 for the fine and coarse modes, respectively (Dubovik et al. 2002). For the smoke event, the ratio of fine to coarse volume concentration was 10.0, and for the dust event, the coarse to fine volume concentration ratio was 5.3.

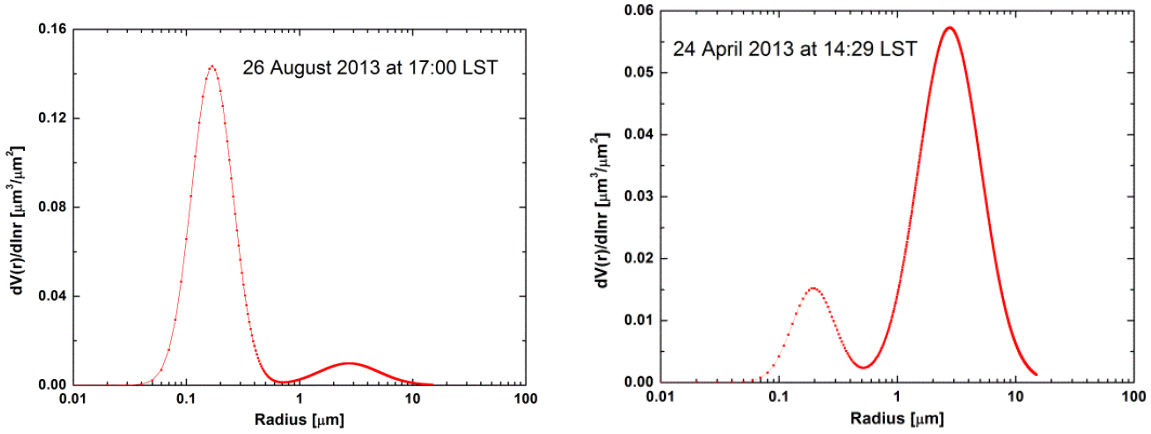

Figure 2.1 Bimodal lognormal aerosol size distributions observed in Reno: (left) during the Rim fire on 26 August 2013 at 17:00 LST measured with the AERONET Cimel sun-photometer and (right) during a dust storm on 24 April 2013 at 14:29 LST derived from the MFRSR data.

Table 2.1 Size distribution function parameters for the Rim fire and dust cases

Particle mode	Concentration ($\mu m^3\ \mu m^{-2}$)	Median radius (μm)	Standard deviation
Coarse			
26 August 2013	0.015	2.734	0.61
24 April 2013	0.088	2.772	0.61
Fine			
26 August 2013	0.151	0.169	0.42
24 April 2013	0.016	0.196	0.42

2.2 Spectral bulk scattering properties

For a given size distribution n(r), the bulk (or mean) scattering properties at a specific wavenumber ν are obtained by integrating the single scattering properties for individual particles over particle size distribution as follows (Yang et al. 2005; Baum et al. 2006):

$$\langle Q_{ext}(\nu)\rangle = \frac{\int_{r_{min}}^{r_{max}} Q_{ext}(r,\nu)A(r)n(r)dr}{\int_{r_{min}}^{r_{max}} A(r)n(r)dr}, \tag{2.6}$$

$$\langle Q_{sca}(\nu)\rangle = \frac{\int_{r_{min}}^{r_{max}} Q_{sca}(r,\nu)A(r)n(r)dr}{\int_{r_{min}}^{r_{max}} A(r)n(r)dr}, \tag{2.7}$$

$$\langle Q_{abs}(\nu)\rangle = \langle Q_{ext}(\nu)\rangle - \langle Q_{sca}(\nu)\rangle, \tag{2.8}$$

$$\langle \omega(\nu)\rangle = \frac{\langle Q_{sca}(\nu)\rangle}{\langle Q_{ext}(\nu)\rangle}, \tag{2.9}$$

$$\langle g(\nu)\rangle = \frac{\int_{r_{min}}^{r_{max}} g(r,\nu)Q_{sca}(r,\nu)A(r)n(r)dr}{\int_{r_{min}}^{r_{max}} Q_{sca}(r,\nu)A(r)n(r)dr}, \tag{2.10}$$

$$r_{eff} = \frac{3}{4}\frac{\int_{r_{min}}^{r_{max}} V(r)n(r)dr}{\int_{r_{min}}^{r_{max}} A(r)n(r)dr}, \tag{2.11}$$

where $\langle Q_{ext}(\nu)\rangle$, $\langle Q_{sca}(\nu)\rangle$, $\langle Q_{abs}(\nu)\rangle$, $\langle \omega(\nu)\rangle$, and $\langle g(\nu)\rangle$ are the mean extinction efficiency, scattering efficiency, absorption efficiency, single scatter albedo, and asymmetry parameter, respectively. The term r_{eff} is the effective particle radius, or the area-weighted mean radius of an aerosol distribution which characterizes the radiation extinction properties of the distribution. V(r) is the volume of the individual particles and A(r) is the geometric projected area of a particle perpendicular to the incident plane. Similarly, $Q_{ext}(r,\nu)$, $Q_{sca}(r,\nu)$, and $Q_{abs}(r,\nu)$ are the extinction, scattering and absorption efficiencies, respectively, for the individual particles at a specific wavenumber. These quantities are computed using the Mie theory (which is described shortly in brief). The scattering asymmetry parameter is defined as the average value of the cosine of the scattered angle, weighted by the intensity of the scattered radiation as a function of angle. Its value is 1 for perfect forward scattering, -1 for perfect backscatter, and 0 for isotropic scattering.

The scattering phase function $\langle P(\theta,\nu)\rangle$ specifies the fraction of radiation scattered in a certain direction which is given by

$$\langle P(\theta,\nu)\rangle = \frac{\int_{r_{min}}^{r_{max}} P(\theta,r,\nu)Q_{sca}(r,\nu)A(r)n(r)dr}{\int_{r_{min}}^{r_{max}} Q_{sca}(r,\nu)A(r)n(r)dr}. \quad (2.12)$$

The Henyey-Greenstein (H-G) phase function is the most widely used 'model' phase function, and is given by (Petty 2006)

$$P_{H-G}(\theta,\nu) = \frac{1-\langle g\rangle^2}{(1+\langle g\rangle^2-2\langle g\rangle\cos\theta)^{\frac{3}{2}}}, \quad (2.13)$$

where θ is the angle between the original direction of the incident photon $\boldsymbol{\Omega}'$ and the scattered direction $\boldsymbol{\Omega}$, such that $\cos\theta = \boldsymbol{\Omega}'.\boldsymbol{\Omega}$. This function is isotropic for g = 0. For g > 0, the function can reproduce the observed forward peak in the phase functions of real particles.

The parameters Q_{ext}, Q_{sca}, Q_{abs}, and g for a single homogeneous sphere is obtained from the Mie theory in the form of an infinite series (Hansen and Travis 1974):

$$Q_{ext} = \frac{2}{X^2} \sum_{j=1}^{\infty} (2j + 1)\, \mathrm{Re}\left(a_j + b_j\right), \tag{2.14}$$

$$Q_{sca} = \frac{2}{X^2} \sum_{j=1}^{\infty} (2j + 1)\left(a_j a_j^* + b_j b_j^*\right), \tag{2.15}$$

$$Q_{abs} = Q_{ext} - Q_{sca}, \tag{2.16}$$

$$g = \frac{4}{X^2 Q_{sca}} \sum_{j=1}^{\infty} \left[\frac{j(j+2)}{(j+1)}\, \mathrm{Re}\left(a_j a_{j+1}^* + b_j b_{j+1}^*\right) + \frac{(2j+1)}{j(j+1)} \mathrm{Re}\left(a_j b_j^*\right)\right]. \tag{2.17}$$

The heart of the Mie scattering problem lies in the computation of coefficients a_j and b_j, which are functions of the size parameter x (where $x = \frac{2\pi r}{\lambda}$, and λ is the incident wavelength) and the complex refractive index, and involve spherical Bessel functions. The series converges whenever the number of terms j in the series is slightly larger than x, i.e., j is an integer closest to $(x + 4x^{\frac{1}{3}} + 2)$ (Petty 2006). Higher order terms correspond to light rays missing the sphere. The infinite series actually represents the multipole expansion of the scattered light. The coefficients a_j specify the amounts of electric multipole radiation whereas b_j specify the magnetic multipole radiation. For small particles with a small refractive index, only the electric dipole radiation is significant, and Rayleigh scattering takes place. Fig. 2.2 illustrates the asymmetry parameter for Rayleigh and Mie scatterings. For large particles all multipoles with $j \leq x$ contribute. For much larger particles, usually $x > 2000$, computation of the Mie theory suffers both a computer-time issue and a numerical precision issue due to round-off errors as a consequence of the large value of j.

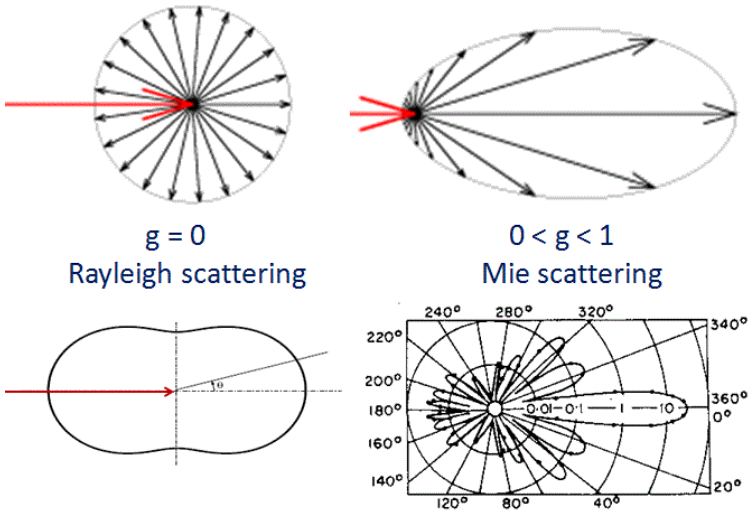

Figure 2.2 Illustration of the phase function for various values of the asymmetry parameter (courtesy: D. Mitchell).

2.3 Physical characteristics of the aerosol problem

This section presents a simple idea about the physical characteristics of the aerosols such as total volume of the aerosols per unit area of the atmospheric column above an instrument. Assume an aerosol-laden atmosphere of volume V observed by an instrument at the surface, whose area is A and height is Z as shown in Fig. 2.3 (left).

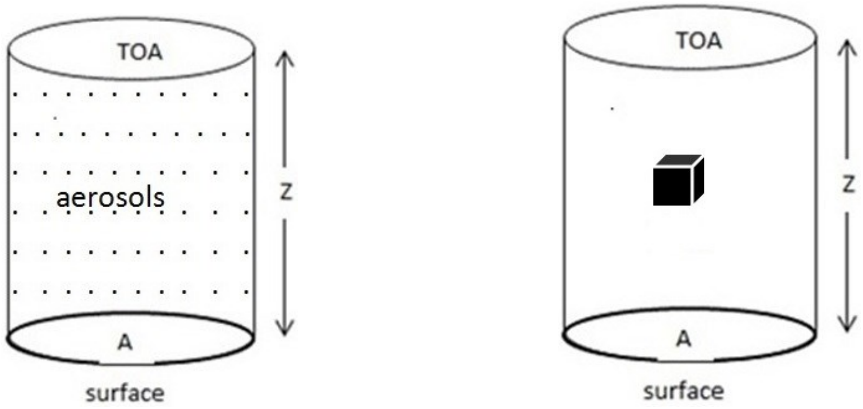

Figure 2.3 Aerosol-laden atmosphere above an instrument at the surface: aerosols distributed over the whole column of the atmosphere (left) and a cube representing the total volume of the aerosols in a unit area (A=1 m^2) of the atmosphere (right).

Referring to the fine mode concentration on 26 August 2013 (Table 2.1), we know that the total volume of all the aerosols present in a column of atmosphere of 1 μm^2 area is 0.151 μm^3, which is equivalent to the volume of 151 mm^3 in an area of 1 m^2. This is, in fact, the volume of all aerosol particles when gathering them together in an area of a unit square meter (Fig. 2.3, right, where A is assumed to be 1 m^2). This volume then represents a cube of side 5.3 mm in this particular case. Is it not a tiny volume of matter dispersed into the whole column of the atmosphere, which we are dealing with?

2.4 Pedagogical model for IR radiative forcing by aerosols

We consider a simplified atmosphere containing water vapor and coarse mode aerosols such as mineral dust (Fig. 2.4) where dust resides only in the boundary layer (0-3 km). Let T be the surface temperature and T_a be the atmospheric temperature.

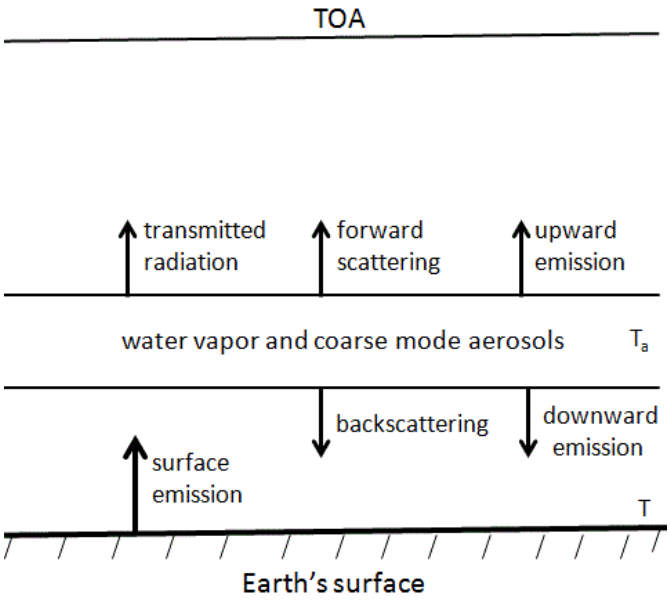

Figure 2.4 A simplified atmosphere containing water vapor and coarse mode aerosols.

The radiance at the TOA is given by

$$R_{TOA}(\nu) = B(T,\nu)\exp\left[-\left(\tau_{abs}^{H_2O} + \tau_{ext}^{dust}\right)\right] + B(T_a,\nu)\left[1 - \exp\left\{-\left(\tau_{abs}^{H_2O} + \tau_{abs}^{dust}\right)\right\}\right] + B(T)\,\tau_{sca}^{dust}\left(\frac{1+g}{2}\right)\exp\left(-\tau_{abs}^{H_2O}\right), \quad (2.18)$$

where ν is the wavenumber; B is the Planck's function; $\tau_{abs}^{H_2O}$ is the absorption optical depth of water vapor; τ_{ext}^{dust} , τ_{abs}^{dust}, and τ_{sca}^{dust} are the extinction, absorption and scattering optical depths, respectively of coarse mode aerosol such as dust; and $\left(\frac{1+g}{2}\right)$ represents the probability of scattering in the forward direction. Similarly the radiance at the BOA is given by

$$R_{BOA}(\nu) = B(T_a, \nu)\left[1 - \exp\left\{-\left(\tau_{abs}^{H_2O} + \tau_{abs}^{dust}\right)\right\}\right] + B(T)\,\tau_{sca}^{dust}\left(\frac{1-g}{2}\right)\exp\left(-\tau_{abs}^{H_2O}\right), \quad (2.19)$$

where $\left(\frac{1-g}{2}\right)$ represents the probability for backward scattering. The second term in Eq. 2.19, therefore, signifies the surface IR backscattering by atmospheric dust.

The spectral radiative forcing at the TOA, $\Delta R_{TOA}(\nu)$ is obtained by subtracting $R_{TOA}(\nu)$ with dust from $R_{TOA}(\nu)$ without dust. Therefore,

$$\Delta R_{TOA}(\nu) = B(T)\exp\left(-\tau_{abs}^{H_2O}\right)\left[1 - \exp\left(-\tau_{ext}^{dust}\right)\right] - B(T_a)\exp\left(-\tau_{abs}^{H_2O}\right)\left[1 - \exp\left(-\tau_{abs}^{dust}\right)\right] -$$

$$B(T)\,\tau_{sca}^{dust}\left(\frac{1+g}{2}\right)\exp\left(-\tau_{abs}^{H_2O}\right). \quad (2.20)$$

Assuming τ_{ext}^{dust} and τ_{abs}^{dust} are far less than 1, then Eq. 2.20 can be written as

$$\Delta R_{TOA}(\nu) = \exp\left(-\tau_{abs}^{H_2O}\right)\left[B(T)\,\tau_{ext}^{dust} - B(T_a)\,\tau_{abs}^{dust}\right] - B(T)\,\tau_{sca}^{dust}\left(\frac{1+g}{2}\right)\exp\left(-\tau_{abs}^{H_2O}\right). \quad (2.21)$$

Using $\omega = \frac{\tau_{sca}^{dust}}{\tau_{ext}^{dust}}$ i.e., single scattering albedo, we have

$$\Delta R_{TOA}(\nu) = \exp\left(-\tau_{abs}^{H_2O}\right)\left[B(T)\,\tau_{ext}^{dust}\left\{1 - \frac{\omega(1+g)}{2}\right\} - B(T_a)\,\tau_{abs}^{dust}\right]. \quad (2.22)$$

In the limit, $\omega \approx 0$, i.e., zero scattering approximation

$$\Delta R_{TOA}(\nu) = \tau_{abs}^{dust}\exp\left(-\tau_{abs}^{H_2O}\right)[B(T) - B(T_a)]. \quad (2.23)$$

We see that, for a large value of $\tau_{abs}^{H_2O}$ (i.e. moist atmosphere), the dust radiative forcing at the TOA, $\Delta R_{TOA}(\nu)$ becomes small. Also, the forcing decreases with increasing atmospheric temperature T_a. In the limit, $\omega \approx 1$ i.e., zero absorption approximation

$$\Delta R_{TOA}(\nu) = \exp\left(-\tau_{abs}^{H_2O}\right)B(T)\left(\frac{1-g}{2}\right)\tau_{sca}^{dust}. \quad (2.24)$$

Apparently the backscattering of the surface-emitted IR by the dust causes the radiative forcing to be important. If $\Delta R_{TOA}(\nu) > 0$, less IR leaves at TOA in the presence of dust and hence the atmosphere gets heated. Using $\tau_{abs}^{dust} = (1-\omega)\tau_{ext}^{dust}$, Eq. 2.22 can be re-written generally as

$$\Delta R_{TOA}(\nu) = B(T)\,\tau_{ext}^{dust}\exp\left(-\tau_{abs}^{H_2O}\right)\left[1-\frac{\omega(1+g)}{2}-(1-\omega)\frac{B(T_a)}{B(T)}\right]. \quad (2.25)$$

The spectral radiative forcing at the BOA, $\Delta R_{BOA}(\nu)$ due to dust is obtained by subtracting $R_{BOA}(\nu)$ without dust from $R_{BOA}(\nu)$ with dust i.e.

$$\Delta R_{BOA}(\nu) = B(T_a)\exp\left(-\tau_{abs}^{H_2O}\right)\left[1-\exp\left\{-(1-\omega)\,\tau_{ext}^{dust}\right\}\right] + B(T)\,\omega\,\tau_{ext}^{dust}\left(\frac{1-g}{2}\right)\exp\left(-\tau_{abs}^{H_2O}\right).$$

Assuming small τ_{ext}^{dust} , we have

$$\Delta R_{BOA}(\nu) = B(T)\,\tau_{ext}^{dust}\exp\left(-\tau_{abs}^{H_2O}\right)\left[\omega\left(\frac{1-g}{2}\right)+(1-\omega)\frac{B(T_a)}{B(T)}\right]. \quad (2.26)$$

Notice that $\frac{B(T_a)}{B(T)} \sim \frac{T_a^4}{T^4}$, and $\frac{T_a^4}{T^4} \approx \left(1-\frac{\Delta T}{T}\right)^4 \approx 1-4\frac{\Delta T}{T}$. Then

$$\Delta R_{BOA}(\nu) \approx B(T)\,\tau_{ext}^{dust}\exp\left(-\tau_{abs}^{H_2O}\right)\left[\omega\left(\frac{1-g}{2}\right)+(1-\omega)\left(1-4\frac{\Delta T}{T}\right)\right]. \quad (2.27)$$

For the zero aerosol absorption and emission case, $\omega = 1$,

$$\Delta R_{BOA}(\nu) = B(T)\,\tau_{ext}^{dust}\exp\left(-\tau_{abs}^{H_2O}\right)\left(\frac{1-g}{2}\right). \quad (2.28)$$

Even though the dust aerosols do not absorb IR at all, the backscattering of IR by the aerosols contributes to IR radiative forcing. Also, the aerosol IR radiative forcing enhances in the drier atmosphere. This offers positive feedback on the climate warming. For a warmer planet, $B(T)$ goes up and contributes to the positive feedback. For $\omega \approx 0$,

$$\Delta R_{BOA}(\nu) = B(T_a)\,\tau_{abs}^{dust}\exp\left(-\tau_{abs}^{H_2O}\right). \quad (2.29)$$

Eq. 2.29 is the zero scattering approximation, which can be used to investigate the perturbation due to any other greenhouse gas. The approximate forcings given in Eqs. 2.25 and 2.26 were also presented by Dufresne et al. 2002, though without the dependence on water vapor optical depth.

3 INSTRUMENTS AND EXPERIMENTAL TECHNIQUES

3.1 Fourier Transform Infrared Spectrometer

Downwelling thermal IR emission spectra of the atmosphere are measured using a passive, ground-based Fourier transform infrared (FTIR) spectrometer (Fig. 3.1) at a spectral range of 500-2000 cm^{-1} (5-20 µm), with a narrow field-of-view (45 mrad, full angle) at 0° to zenith. The instrument uses a commercial Michelson interferometer (Model MB 100) manufactured by Bomem, Inc., (Quebec, Canada). It contains a liquid-nitrogen-cooled, narrow band Mercury-Cadmium-Telluride (MCT; HgCdTe) detector, which is sensitive to LW radiation from 5-20 µm. A rotating gold-plated scene mirror is used to direct the emission from each target: blackbodies and sky, into the interferometer. The instrument measures interferogram (a unique type of signal, which has all of the IR frequencies encoded into it), from which complex radiance spectra are computed using Fourier transforms. The complex spectra from the two high-emissivity, well-characterized blackbodies at known temperatures are used to calibrate the atmospheric spectrum. The two blackbodies are identically designed, with one kept at about 50°C while the other is allowed to cool down to -10°C. More details on the construction and specifications of the spectrometer, including calibration procedure, are provided by Adhikari 2012. We provide that the instrument has good radiometric calibration.

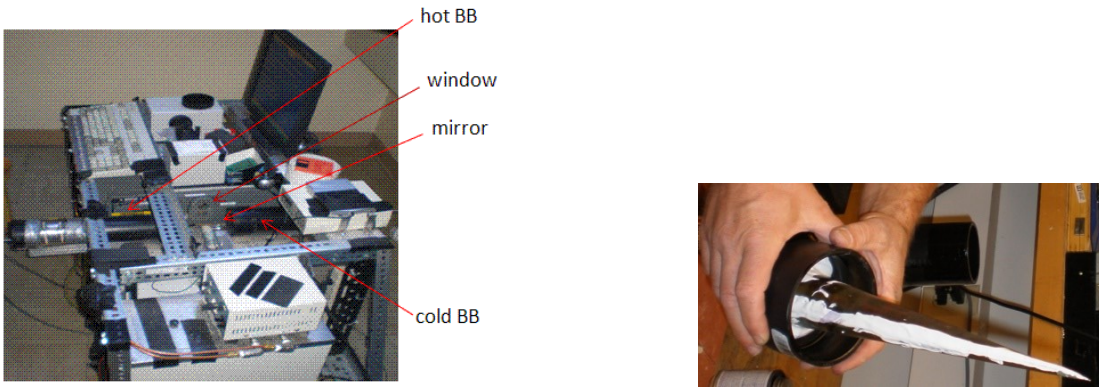

Figure 3.1 Fourier transform infrared (FTIR) spectrometer (left) and the exterior of a conical high-emissivity blackbody calibration target (right).

The FTIR was installed in the observatory of the four-story physics building at UNR. Measurements were initiated only under cloud-free conditions to study aerosol effects. The instrument was exposed to the external environment for about an hour allowing the IR source and the spectrometer temperature to stabilize after turning the power on. The spectrometer was operated in the emission mode at a resolution of 1 cm^{-1} over a range of 500-2000 cm^{-1} and pre-amplifier gain at 16×.

The measurement sequence typically consisted of viewing the cold calibration target (≈ -10°C), then viewing the hot target (≈ 50°C), and finally the atmosphere, each for 20 scans of the interferometer, resulting in an approximate 8-min temporal resolution. The calibration spectra from just before and after each atmospheric observation were used to calibrate the atmospheric emission spectra and to reduce the possible temperature drifts. For making the analysis of the spectra convenient, we measured radiance and the corresponding spectrally resolved brightness temperature obtained from the inverse of Planck's blackbody function. We chose 00:00 and 12:00 Coordinated Universal Time (UTC) hours of the days to measure the FTIR spectra as the radiosonde from the National Weather Service in Reno was launched during the periods. Using the same hours of the day provide appropriate profiles of atmospheric temperature, pressure, and dew point to model the observed spectra.

Fig. 3.2 shows the typical clear sky radiance and brightness spectra computed from the FTIR spectrometer for 01 August 2013 at 17:00 LST. Each cloud-free spectrum includes the collective downwelling emissions from the greenhouse gases and aerosols.

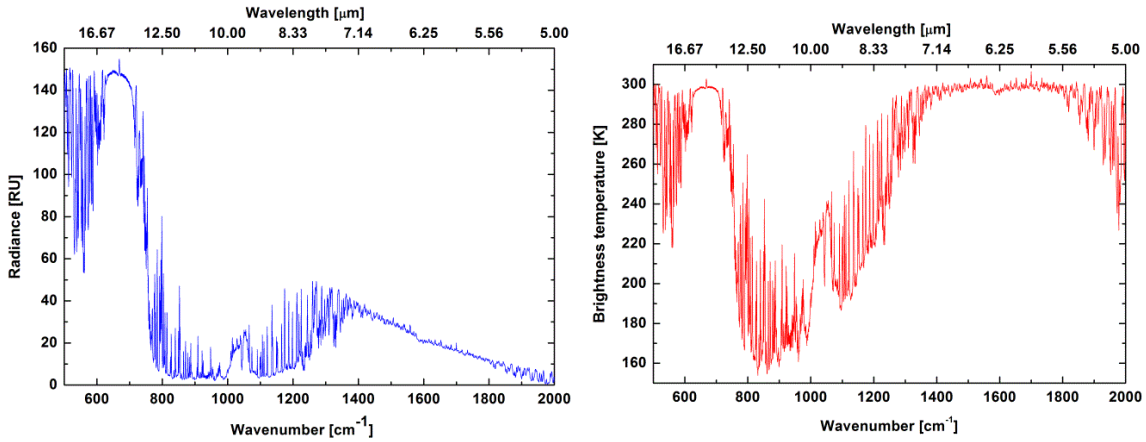

Figure 3.2 Typical examples of clear sky radiance (left) and brightness temperature (right) spectra observed with FTIR at UNR on 01 August 2013 at 17:00 LST. A radiance unit (RU) is 1 mW/(m^2 Sr cm^{-1}). Radiance spectra are converted into brightness temperature spectra using an inverse Planck function in the wavenumber domain (Adhikari 2012).

3.2 AERONET Cimel sun-photometer

The Aerosol Robotic Network (AERONET) Cimel sun-photometer (Fig. 3.3) is an automated, solar-powered, ground-based, and passive sun photometer which is used for characterization and quantification of the atmospheric aerosols in a vertical column, and air quality monitoring purpose. The Cimel sun-photometer is installed outside on the roof of the four-story physics department building at UNR. The instrument is part of NASA's AERONET.

Figure 3.3 Cimel CE-318 sun-photometer.

The instrument measures both the direct-beam solar/aureole and diffuse sky radiances at multiple wavelengths ranging from the ultra-violet (UV) through near-infrared (NIR): 0.34, 0.38, 0.44, 0.50, 0. 67, 0.87, 1.02 and 1.64 μm at a narrow full angle field of view of 1.2° with two filtered detectors: silicon photodiode for the UV and visible wavelengths, and Indium-Gallium-Arsenide (lnGaAS) for the NIR wavelengths (Holben et al. 1998). These detectors are fitted on the two 33 cm collimators.

The sky radiance observations are made in the almucantar (or horizontal) and principal (or vertical) plane. The almucantar measurement is made at constant zenith angle and airmass where as the principal plane measurement is made in the principal plane of the sun where the angular distances from the sun are scattering angles regardless of the zenith angle. The instrument provides the cloud-screened observations of columnar spectral aerosol optical depth (AOD) and water vapor column content at a temporal resolution of about 10-15 min (Sayer et al. 2013). The aerosol microphysical properties such as volume size distribution (in 22 logarithmically-spaced bins with radii from 0.05-15 μm) and spectral complex refractive index, and optical properties such as single scatter albedo, asymmetry parameter, and scattering phase functions are retrieved using an inversion algorithm developed by Dubovik and King 2000 and Dubovik et al. 2006, for spherical and non-spherical particles, respectively.

The aerosol optical depth is obtained from the Lambert-Beer law,

$$I(\lambda) = I_0(\lambda)\exp(-\tau(\lambda)/\mu), \quad (3.1)$$

where $\tau(\lambda) = \left[\tau_{\text{gases}}(\lambda) + \tau_{\text{aerosols}}(\lambda) + \tau_{\text{water vapor}}(\lambda) + \tau_{\text{ozone}}(\lambda)\right]$ is the total vertical atmospheric optical depth at a given wavelength λ, $I_0(\lambda)$ is the solar irradiance at the top of the atmosphere, and $I(\lambda)$ is the direct-sun irradiance measured by the instrument at the ground. The term 'gases' generally refers to Rayleigh scattering by the air molecules such as N_2, O_2, etc., in this analysis. The quantity μ is given by $\mu = \cos\theta$ where θ is the solar zenith angle measured with respect to vertical, which is calculated internally based on the time, and longitude and latitude of

the observation station. The relation $\mu = \cos\theta$ holds as long as the sun is fairly high in the sky i.e., $\theta \leq 70°$; otherwise a modified expression should be used to account for the curvature of the Earth (Kasten and Young 1989)

$$\mu = [\cos\theta + 0.50572\ (96.07995 - \theta)^{-1.6364}]. \quad (3.2)$$

The reciprocal of μ is referred to as optical airmass factor (dimensionless quantity) which represents the optical path length and describes the enhancement of the slant path over the vertical for which air-mass factor is one. The airmass factor is, therefore, close to one at noon and as large as 57 during sun-rise and sun-set.

Eq. 3.1 can be changed into linear form by taking natural logarithms on both sides. The slope and y-intercept of the $I(\lambda)$ versus $1/\mu$ plot give τ_λ and $I_0(\lambda)$, respectively (Petty 2006, Eq. 7.39,). This procedure is called Langley linear regression analysis. The quantity τ_{gases} is approximated using the Rayleigh optical depth formula given by Hansen and Travis 1974:

$$\tau_{gases}(\lambda) = 0.008569\left(\frac{1}{\lambda^4} + \frac{0.0113}{\lambda^6} + \frac{0.00013}{\lambda^8}\right)\frac{P}{P_0}, \quad (3.3)$$

where P and P_0 stand for the pressure at the measurement site and the pressure at the sea level (i.e. 1013.24 mbar), respectively, and λ is in μm. The subtraction of $\left[\tau_{gases}(\lambda) + \tau_{water\ vapor}(\lambda) + \tau_{ozone}(\lambda)\right]$ from $\tau(\lambda)$ yields $\tau_{aerosols}$ at a specific wavelength. The aerosol microphysical properties are derived through the inversion of spectral sky radiance at known angular distance from the sun.

Cimel sun-photometer is a wide-spread (more than 600 instruments operating around the world) and scientifically validated instrument. It is extremely sensitive, low-noise, and resistant to changes in temperature and harsh atmospheric condition. Motor-driven filters wheel positions each of the filters in turn. The instrument details and operation can be found at http://www.arm.gov/publications/tech_reports/handbooks/csphot_handbook.pdf?id=79.

Figs. 3.4 and 3.5 are measurements and inversion products of Cimel sun-photometer at the UNR station. Cimel measured the high AOD at each channel (Fig. 3.4; top panel) due to the presence of smoke aerosols from the California Rim fire on 26 August 2013 in the atmosphere over Reno. The AODs are larger for shorter wavelengths than for longer wavelengths. The size distribution plot (Fig. 3.4; bottom panel) shows the predominance of fine mode particles over coarse mode particles on the smoky day.

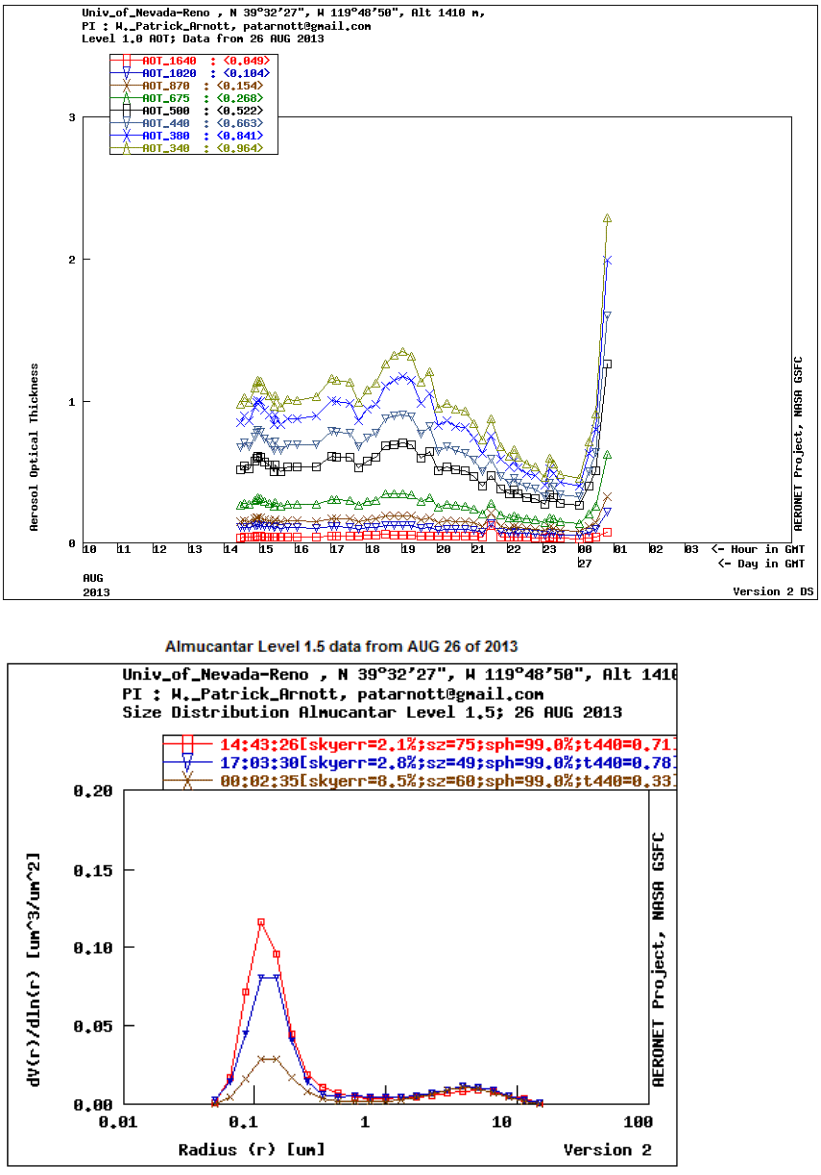

Figure 3.4 Cimel-observed time series spectral AOD (top) and size distribution (bottom) plots for 26 August 2013 in Reno.

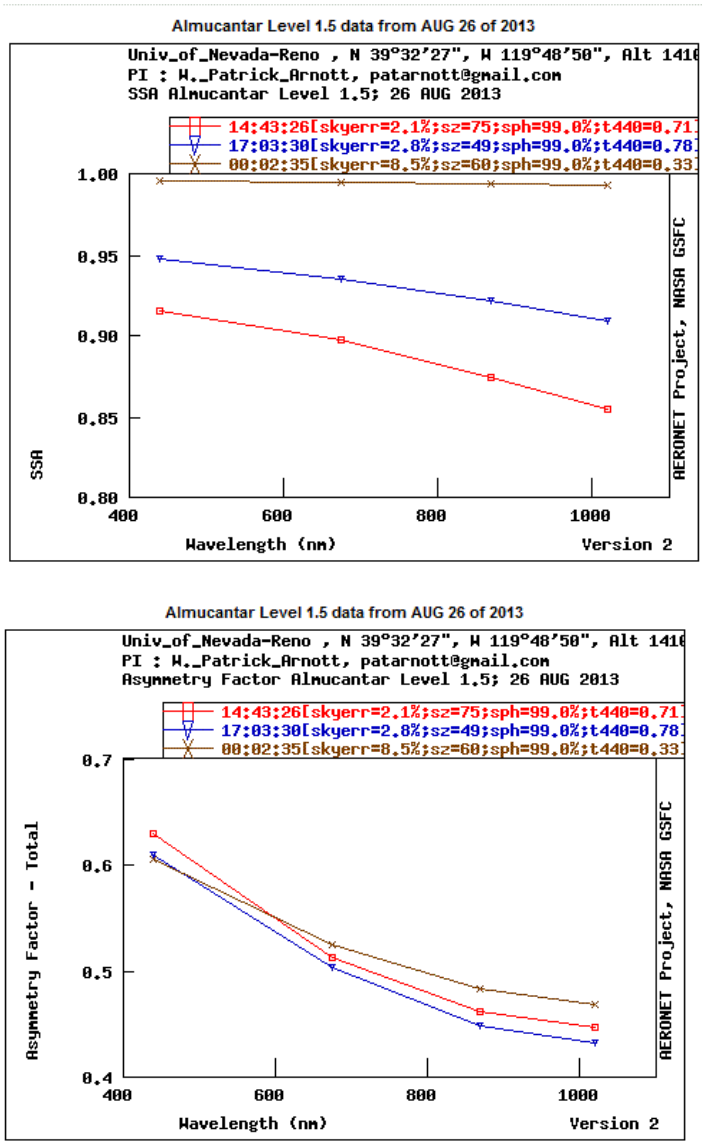

Figure 3.5 Cimel-observed spectral single scatter albedo (top) and asymmetry parameter (bottom) for 26 August 2013 in Reno.

The single scatter albedo (SSA) plot (Fig. 3.5; top panel) shows the variation of SSA with wavelength at different periods of the day 26 August 2013. The SSA usually decreases with increase in wavelength. This is because the fine mode scattering declines with increase in wavelength. We see a similar trend for the asymmetry parameter (or factor) (Fig. 3.5; bottom panel) as SSA. Shorter wavelengths are scattered more in the forward direction by the given particle size.

3.3 Multi-filter rotating shadow-band radiometer

The multi-filter rotating shadow-band radiometer (MFRSR) is also an automated, electrically-powered, ground-based solar instrument which is used to characterize and quantify the atmospheric water vapor, ozone, and aerosols. Fig. 3.6 displays the full picture of the MFRSR (left) and the cut-view of the instrument (right).

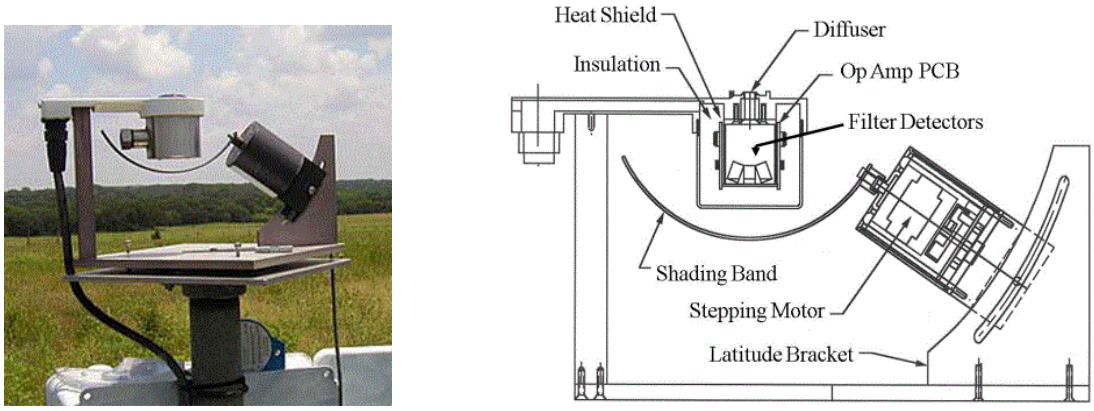

Figure 3.6 Full picture of MFRSR (left) and cut-out view of the MFRSR (right) (Source: GB Hodges and JJ Michalsky, 2011)

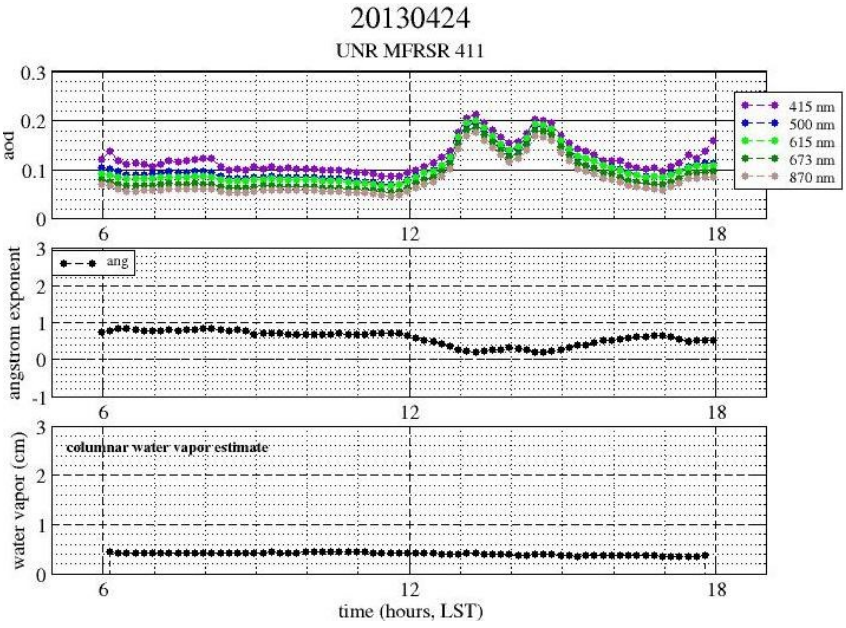

Figure 3.7 MFRSR-observed time series of spectral AOD (top), Angstrom exponent (middle) and water vapor content (bottom) on 24 April 2013 in Reno.

The detail information on its structure and operation can be found at

http://www.arm.gov/publications/tech_reports/handbooks/mfr_handbook.pdf

MFRSR measures the downwelling total (direct plus diffuse)-horizontal and diffuse (or scattered)-horizontal solar irradiances in units of W/(m^2 μm) at six narrowband visible and NIR wavelengths of 0.415, 0.5, 0.615, 0.673, 0.870, and 0.940 μm simultaneously at a temporal resolution of one minute or less with independent interference-filter-silicon photodiode detectors and the automated rotating shadow-band technique (Harrison et al. 1994). This set of wavelengths is sensitive to gases (Rayleigh) scattering, aerosol extinction, water vapor absorption, and ozone absorption as follows: 0.615 μm (ozone and aerosols), 0.940 μm (water vapor), and the rest (mainly to aerosols). Both the total and diffuse irradiance components are measured with the same detector for each channel. An initial measurement is made for the total horizontal irradiance. The shadow-band is then rotated to block out the direct solar beam to measure the diffuse component alone. The direct component is then obtained by subtracting the diffuse component from the total irradiance. The Langley linear regression analysis is performed on the direct-normal component observations to obtain spectral AOD and calibration constants. These AODs can be used to derive the column abundances of atmospheric aerosols, water vapor and ozone, just as with the Cimel instrument.

In order to retrieve the AOD, the 0.415 and 0.870 μm–channel data are used in which the water vapor and ozone absorption are relatively insignificant i.e. $\tau_{\text{water vapor}} = \tau_{\text{ozone}} \approx 0.0$. Then, $\tau_{\text{aerosol}}(\lambda) = \tau(\lambda) - \tau_{\text{gases}}(\lambda)$.

The Angstrom exponent α is measured using 0.5 μm and 0.87μm wavelengths

$$\alpha = \frac{-\ln\left[\frac{\tau_{\text{aerosol}}(0.5)}{\tau_{\text{aerosol}}(0.87)}\right]}{\ln\left[\frac{0.5}{0.87}\right]}. \qquad (3.4)$$

This parameter α provides basic information on the aerosol size. For example, α is 1 to 3 for fine-mode anthropogenic pollutants, and α ~ 0 for coarse mode particles (Reid et al. 1999). Fig. 3.7

represents a typical time series plots for the spectral AOD, Angstrom exponent, and water vapor content measured by the MFRSR on 24 April 2013 in Reno. The higher AOD values during afternoon indicate the arrival of dust plume in Reno. The smaller values of α during the same hours indicate the predominance of coarse mode mineral dust particles over Reno. The low values of columnar precipitable water signify that Reno was very dry all day. The MFRSR data was used to obtain the dust case study size distribution because the Cimel data was not available. The MFRSR complements the Cimel (Air 2014).

4 RADIATIVE TRANSFER MODELS

4.1 Line-by-line radiative transfer model and discrete ordinate radiative transfer solver

Fig. 4.1 represents the schematic flowchart of the radiative transfer models used in this work.

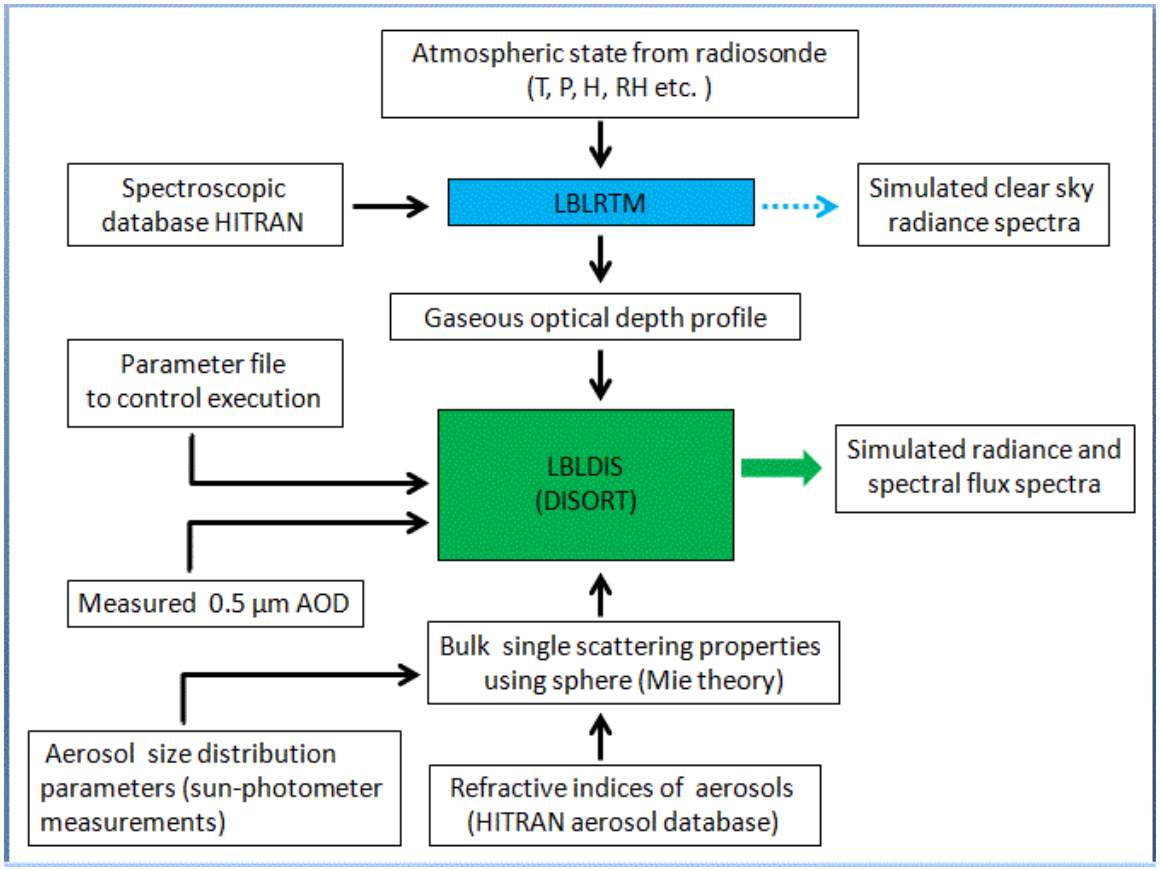

Figure 4.1 Flowchart for model description

We have used two radiative transfer models: Line-By-Line Radiative Transfer Model (LBLRTM; Clough and Iacono 1995) and the combination of LBLRTM and Discrete Ordinates Radiative Transfer Solver (DISORT; Stamnes et al. 1988), called LBLDIS (Turner 2003; Turner 2005).The LBLDIS takes scattering, absorption, and thermal emission of the clouds and aerosols into account and provides the radiative transfer. Both models assume the Earth-atmosphere as being composed of vertically inhomogeneous plane-parallel layers with homogeneous layers and the location in the atmosphere is specified by the optical depth τ as shown in Fig. 4.2.

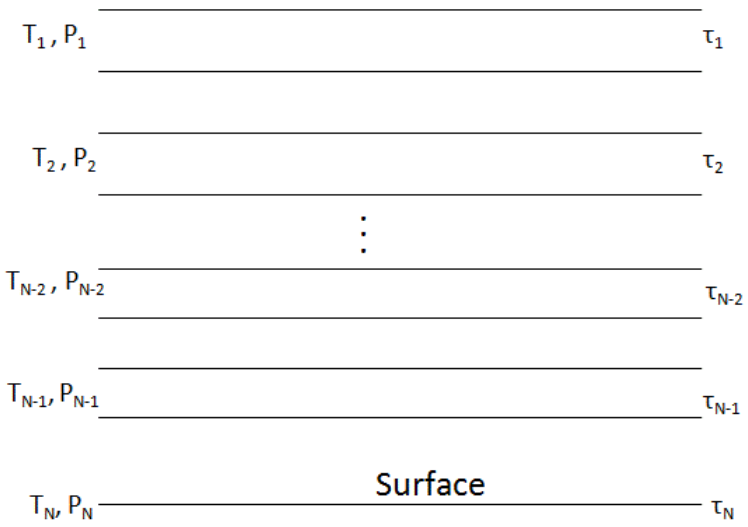

Figure 4.2 Schematic representation of the atmospheric plane-parallel multilayered medium. T and P are temperature and pressure, respectively, and τ is optical depth.

The LBLRTM, along with the line parameter database and the continuum model, is available from the Atmospheric and Environmental Research (AER) Incorporated's website http://rtweb.aer.com. LBLRTM is a highly accurate, computationally efficient, and flexible line-by-line radiative transfer model which was derived from the FASCODE (Fast Atmospheric Signature Code), and developed at AER Inc., (Clough et al. 2005). The validations of the model have been performed for a wide variety of atmospheric conditions. Even though the model documentation is available online at http://rtweb.aer.com/lblrtm_frame.html, a brief overview on the LBLRTM is presented here.

The LBLRTM is used to compute spectral gaseous absorption optical depths profiles, and upwelling and downwelling transmittances and radiances emitted by the Earth-atmosphere system. The model uses the HITRAN (http://cfa-www.harvard.edu/hitran) molecular spectroscopic absorption database (Rothman et al. 2005) for the spectroscopic line parameters along with the MT_CKD (Mlawer-Tobin-Clough-Knsizys-Davies) continuum model which includes self and foreign broadened coefficients for water vapor as well as continua absorption by CO_2, N_2, and O_2, half-width dependence on temperature, pressure shift coefficient, and

extinction due to Rayleigh scattering. Voigt line shape is used at all atmospheric levels, with a line cut-off at 25 cm^{-1} from the line center. The model has been extensively validated against clear-sky atmospheric radiance spectra from ultra-violet to microwave, since it has been used to produce a Rapid Radiative Transfer Model (RRTM) employed in the community climate models and other models (Turner 2003). Version 12.2 of the LBLRTM, and version 2.5.2 of MT_CKD continuum model and the HITRAN 2008 line parameters (Rothman et al. 2009) are used in this work.

The LBLRTM package contains the line parameter database with the corresponding line coupling parameters e.g. aer_V_3.2 and the corresponding LNFL program (v_2.6) that converts the ascii line file into an input binary file for LBLRTM. LNFL is a line file creation program that extracts the line parameters for use in LBLRTM and stores in a file called TAPE3. Most of the input and output file names are given as "TAPEx" where x is a one- or two-digit number. TAPE3 produced by LNFL and TAPE5 about the atmospheric profiles are inputs required to run LBLRTM. TAPE27 is one of the output files which contains the radiance spectra in the units $W/(cm^2\ Sr\ cm^{-1})$ with the highest pressure level (lowest altitude) as the first layer. TAPE6 contains the layer information such as altitude, pressure, temperature, and concentrations of various greenhouse gases for a given run. The model can be run in various platforms such as UNIX/LINUX, OS X, SOLARIS, IRIX and AIX. Fig. 4.3 outlines the general features of the LBLRTM model.

The model in our calculation used 119 layers of atmosphere as high as 75 km above the surface

The HITRAN 2008 database (Version 13.0) contains over 2,713,000 lines for 39 different molecules. In order to resolve these individual lines, a nominal spectral sampling rate of less than the mean line half width must be utilized. Such highly resolved radiative transfer calculations are called line-by-line (LBL) calculations.

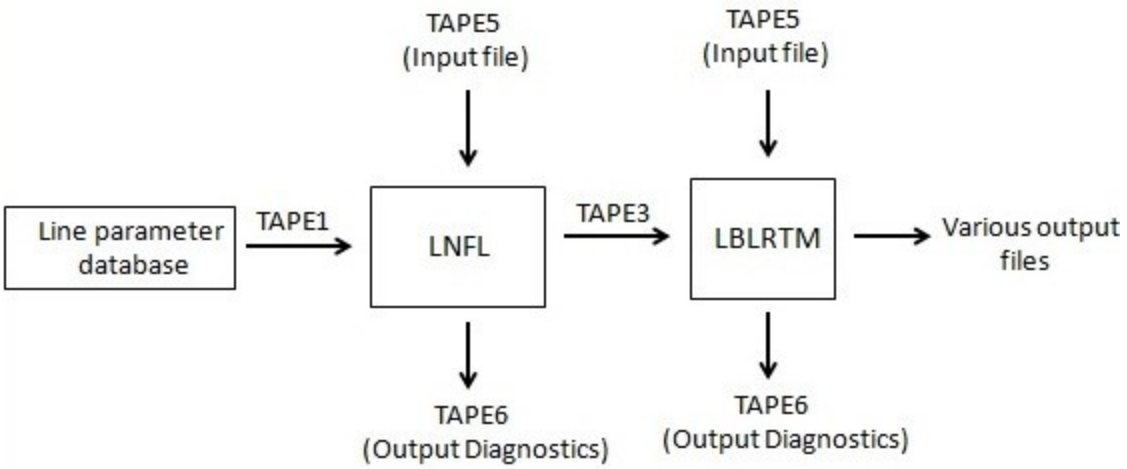

Figure 4.3 Schematic representation of LBLRTM model.
(http://rtweb.aer.com/lblrtm_frame.html**)**

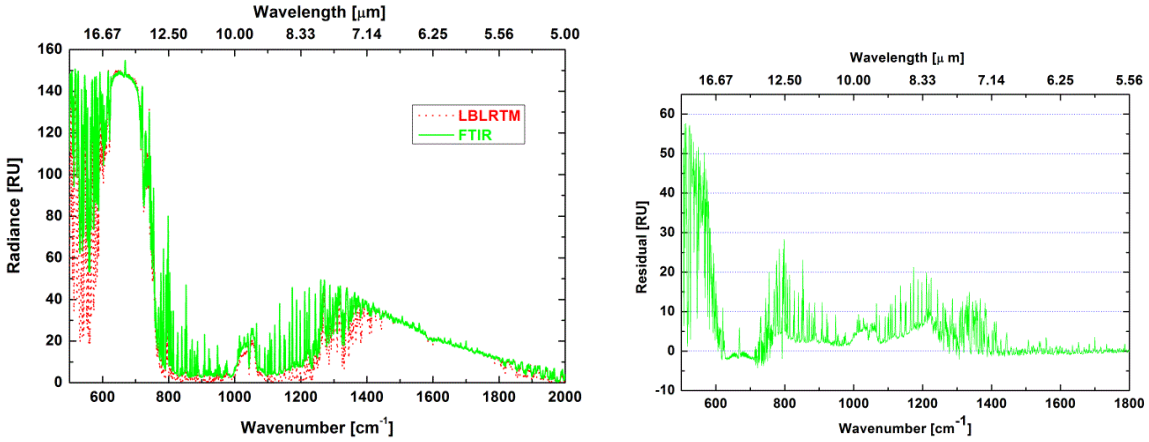

Figure 4.4 FTIR vs LBLRTM radiance (left) and (FTIR-LBLRTM) residual radiance for 01 August 2013 at 17:00 LST in Reno. A radiance unit (RU) is 1 mW/(m^2 Sr cm^{-1}).

Both the FTIR-observation and LBLRTM calculations in Fig. 4.4 are based on 01 August 2013 clear sky emission at 17:00 LST aka 00:00 UTC on 02 August 2013 in Reno. The concurrent radiosonde profiles of temperature, pressure, and humidity were used as an input to represent the atmospheric structure. The radiosonde launch is located at the National Weather Service near Desert Research Institute (DRI) in Reno, about a mile away from the observation station. We used the US Standard Atmosphere (1976) model for the atmospheric profiles beyond the

coverage of the sounding (usually above 30 km). The causes of discrepancy between the measurement and model as seen in Fig. 4.4 (right) are detailed in Chapter 5.

In order to compute the radiation from a cloudy scene and aerosol-loaded atmosphere at high spectral resolution, the LBLRTM is coupled with the DISORT, collectively called LBLDIS. For this purpose, the LBLRTM is used to calculate the monochromatic absorption optical depth of atmospheric gases at each vertical layer for the sounding launched on that day and time of FTIR observation. The single scattering properties of the cloud or aerosol layer such as asymmetry parameter; single scatter albedo; extinction, scattering and absorption efficiencies integrated over an appropriate size distribution function, together with the profiles of gaseous optical depth as a function of wavenumber are input to DISORT to complete the radiative transfer calculation. DISORT is designed to solve the equations of plane-parallel radiative transfer in a vertically inhomogeneous multi-layered atmosphere which is able to compute both the scattered and thermally emitted radiation at different heights and directions. DISORT solves the following Eq. 4.1 describing the full transfer of monochromatic radiation at wavenumber ν through a plane-parallel medium (Stamnes et al. 1988)

$$\mu \frac{dI_\nu(\mu,\phi)}{d\tau} = I_\nu(\mu,\phi) - J_\nu(\mu,\phi), \qquad (4.1a)$$

where $I_\nu(\mu,\phi)$ is the monochromatic (or spectral) intensity along direction μ (cosine of the polar angle, θ), ϕ (azimuthal angle) at optical depth τ_ν measured perpendicular to the surface. $J_\nu(\mu,\phi)$ is the source function for both emission and scattering which is given by

$$J_\nu(\mu,\phi) = (1-\omega)B(\nu,T) + \frac{\omega}{4\pi}\int_0^{2\pi}\int_{-1}^{1} P(\mu,\phi;\mu',\phi')\, I_\nu(\mu',\phi')\, d\mu' d\phi', \qquad (4.1b)$$

where P is the scattering phase function, ω is the single scatter albedo, and B is the Planck's function. Eq. 4.1 is, in fact, the full radiative transfer equation for a plane-parallel atmosphere. This equation is subjected to boundary and continuity conditions that require that the intensity be continuous across layer interfaces. The single scattering properties are taken to be constant

within each layer, but they are permitted to vary from layer to layer as shown in Fig. 4.2. The DISORT algorithm is versatile, and is appropriate for atmospheric applications ranging from the ultra-violet (UV) through to the radar region of the electromagnetic spectrum. The algorithm has been tested against a wide variety of published solutions.

Eq. 4.1 can be used to solve for both the downwelling $I_\nu^\downarrow$ and upwelling $I_\nu^\uparrow$ monochromatic intensities (or radiances). The spectral) flux is obtained by integrating $I_\nu \cos\theta$ over one hemisphere of solid angle (Petty 2006; Eqs. 2.58 and 2.59) i.e.

$$F_\nu^\downarrow = -\int_0^{2\pi}\int_{\pi/2}^{\pi} I_\nu^\downarrow \cos\theta \sin\theta \, d\theta \, d\phi, \quad (4.2a)$$

for downward flux and

$$F_\nu^\uparrow = \int_0^{2\pi}\int_0^{\pi/2} I_\nu^\uparrow \cos\theta \sin\theta \, d\theta \, d\phi, \quad (4.2b)$$

for upward-directed flux. The dimensions of the spectral flux are power per unit area per unit wavenumber. Since I is positive, both the fluxes are positive. The broadband flux over the desired range of wavenumber $[\nu_1, \nu_2]$ is then obtained by integrating the monochromatic flux F_ν over that spectral range i.e.

$$F(\nu_1, \nu_2) = \int_{\nu_1}^{\nu_1} F_\nu d\nu. \quad (4.3)$$

The typical units of the broadband flux are W/m^2.

An ASCII parameter file is the first file that is read by the LBLDIS, which controls its execution. The file contains the number of streams (and Legendre polynomials) to be used by DISORT, polar angles, zenith angle, wavenumber range and the spectral resolution for the calculation, the number of cloud, or aerosol layers, the location of the cloud/aerosol, the cloud/aerosol properties such as effective radius and optical depth for a reference wavenumber e.g., 900 cm^{-1} (11.0 μm). Also included in the file are the location for the LBLRTM output files that contains the gaseous optical depth profiles and the atmospheric state data, SSP database, and information about the surface temperature and emissivity. The parameter file also allows to choosing 'microwindows'

in the given spectral region that are relatively free from greenhouse gaseous absorption lines (microwindows between gaseous absorption lines will minimize the effects of the atmospheric gases such as water vapor and other trace gases), as well as using Henyey-Greenstein function to approximate the scattering phase function. Followed by reading the parameter file, DISORT proceeds to compute the downwelling radiance. Apart from radiance spectrum, the program also calculates the spectral fluxes, which are all stored in the Network Common Data Form (netCDF) output file. The computed radiance and spectral fluxes are then convolved with FTIR's instrument function to compare the calculation with the observation. The spectral fluxes can be used to obtain the broadband flux in W/m^2 by integrating them over the desired spectral range (Eq. 4.3).

Finally, the radiative forcing of the aerosols at the bottom of the atmosphere (BOA) and at the top of the atmosphere (TOA) denoted by ΔF_{BOA} and ΔF_{TOA}, respectively, are calculated by using the following equations (Wendisch et al. 2007; Markowicz et al. 2003)

$$\Delta F_{BOA} = \left[F^{\downarrow}_{BOA}\right]_{aerosol} - \left[F^{\downarrow}_{BOA}\right]_{clear} \quad (4.4)$$

$$\Delta F_{TOA} = -\left\{\left[F^{\uparrow}_{TOA}\right]_{aerosol} - \left[F^{\uparrow}_{TOA}\right]_{clear}\right\} \quad (4.5)$$

The quantity F with superscripts up-arrow and down-arrow represents the upwelling and downwelling broadband fluxes, respectively. The index 'clear' indicates the aerosol and cloud-free condition and the index 'aerosol' represents the inclusion of aerosol in the atmosphere during calculation. Conventionally, positive and negative signs of ΔF imply the aerosol heating and cooling effects, respectively.

5 A CASE STUDY OF CLEAR SKY OVER RENO

5.1 Clear sky measurement and simulation

The clear sky (free from visible clouds and aerosols) radiances are dominated by emission from the greenhouse gases in the atmosphere. The relatively dry atmospheric condition of Reno is favorable for reducing the strong effect of water vapor in the thermal IR region. We present measurements that were carried out in the afternoon at 17:00 LST on 01 August 2013 aka 00:00 UTC on 02 August 2013 and in the morning at 05:00 LST (12:00 UTC) on 02 August 2013. These days were very dry with column precipitable water (PW) of 1.48 and 3.93 mm, respectively. The FTIR-observed radiances were simulated using LBLRTM with the atmospheric state (temperature, moisture profile etc.) from respective radiosondes as an input. In addition to the molecular spectroscopic database, a number of additional parameters (e.g., spectral information, additional atmospheric data, path characteristics, and output format) are also required in the LBLRTM input file.

Figs. 5.1a and 5.1b are Reno's sounding profiles of the temperature and dew point plotted as a function of pressure and altitude on Skew-T Log-P graphs from the National Weather Service (NWS) as processed by the Atmospheric Science department at the University of Wyoming. Fig. 5.1a is the sounding for 17:00 LST, 01 August 2013 and Fig. 5.1b is for 05:00 LST, 02 August 2013. The station identification number and the station name abbreviation for Reno have been shown in the upper left-hand corner of the Skew-T Log-P plots. The arrows on the immediate right of the plot indicate wind direction profiles. The most important features of the sounding plots lie on the temperature profile of the atmospheric boundary layer (BL). In the afternoon (Fig. 5.1a), there is a strong adiabatic condition (temperature decreasing with height) from the surface up to the pressure level of approximately 650 milibars (mb). The temperature curve is approximately parallel to the dry adiabats, indicating a well-mixed layer or dry BL. The thickness of the BL extends to 3 km above the ground. The dry adiabatic condition of the atmosphere

allows the pollutants to be well-mixed over the wide vertical range of the atmosphere reducing pollutants' concentrations significantly near the surface. On the contrary, Fig. 5.1b shows a strong morning inversion (temperature increasing with height) at 12.00 UTC reaching a height corresponding to a pressure of about 800 mb. The inversion layers are extremely stable because the air parcels at the surface are colder and therefore, much denser than those above. The surface's cold air then causes the pollutants to accumulate in the stable environment resulting in an increase in pollutants' concentrations at the surface.

Our measurement is mainly associated with a part of the thermal IR region (500-2000 cm^{-1}; 20-5μm), which plays a major role in the radiative balance of the Earth. Fig. 4.4 (left) depicts the radiance spectra measured with the FTIR (green solid curve) at 17:00 LST on 01 August 2013 and the LBLRTM-simulated radiance spectra (red broken curve). Fig. 5.2a illustrates the FTIR-observed radiance spectra (green solid curve) at 05:00 LST on 02 August 2013 and the simulated radiance spectra (red broken curve). The features of the adiabatic and inverted conditions of the atmosphere can also be seen in the measured and simulated radiance spectra of Figs. 4.4 (left) and 5.2a, respectively as well as the brightness temperature spectra of Fig. 5.2b. The adiabatic temperature structure of the BL in the afternoon changes into the inverted structure in the early morning due to overnight cooling of the Earth's surface.

The brightness temperature at about 668 cm^{-1} (or 15 μm) corresponds to the temperature of the atmosphere at or near the surface and the brightness temperatures far from the wavenumber correspond to the temperatures of the upper levels. The spikes that are seen at 668 cm^{-1} in both spectra of Fig. 5.2b indicate the temperature of the hotter dome-shaped observatory in the afternoon (which is about 300 K) and in the morning (which is about 290 K).

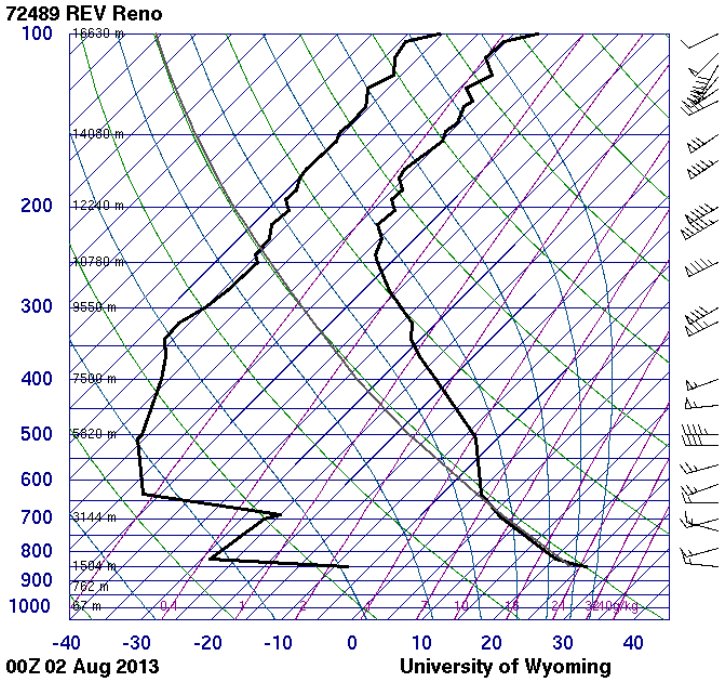

Figure 5.1a Radiosonde data for Reno, NV 01 August 2013, 00:00 UTC. The solid lines on the right and left represent the temperature and dew point temperature, respectively.

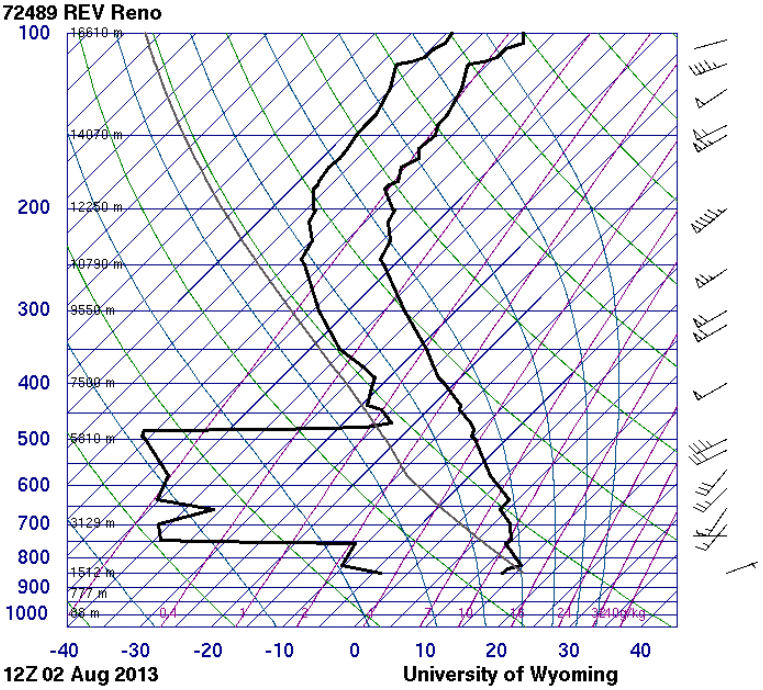

Figure 5.1b Radiosonde data for Reno, NV 02 August 2013, 12:00 UTC. Vertical profiles of temperature and dew point temperature are used for the initialization of the model simulations.

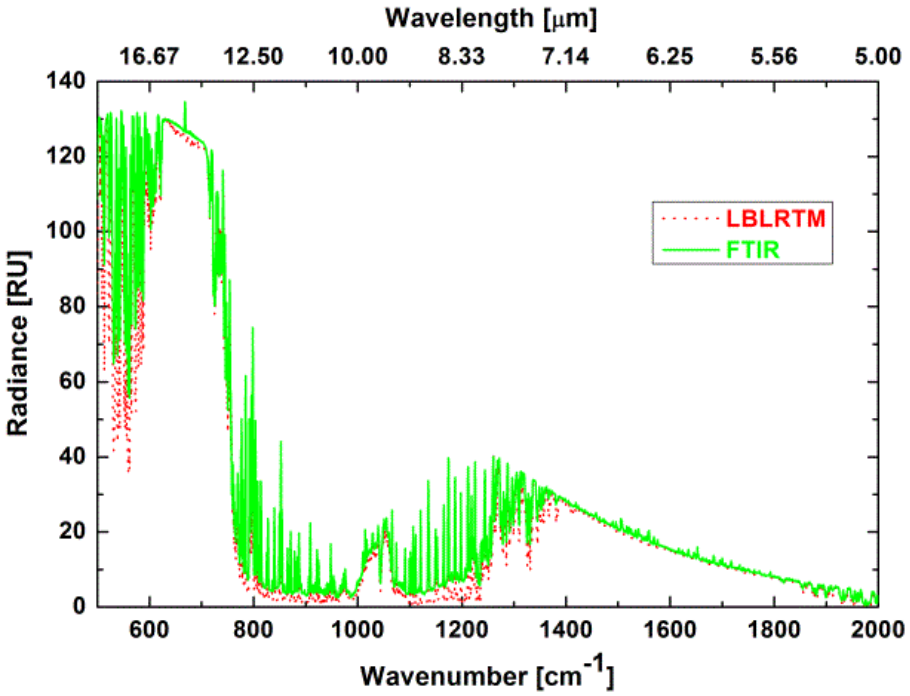

Figure 5.2a A comparison of the measured radiance spectra (green solid curve) for 05:00 LST on 02 August 2013 to the model radiance spectra (red broken curve). A radiance unit (RU) is 1 mW/(m^2 Sr cm^{-1}).

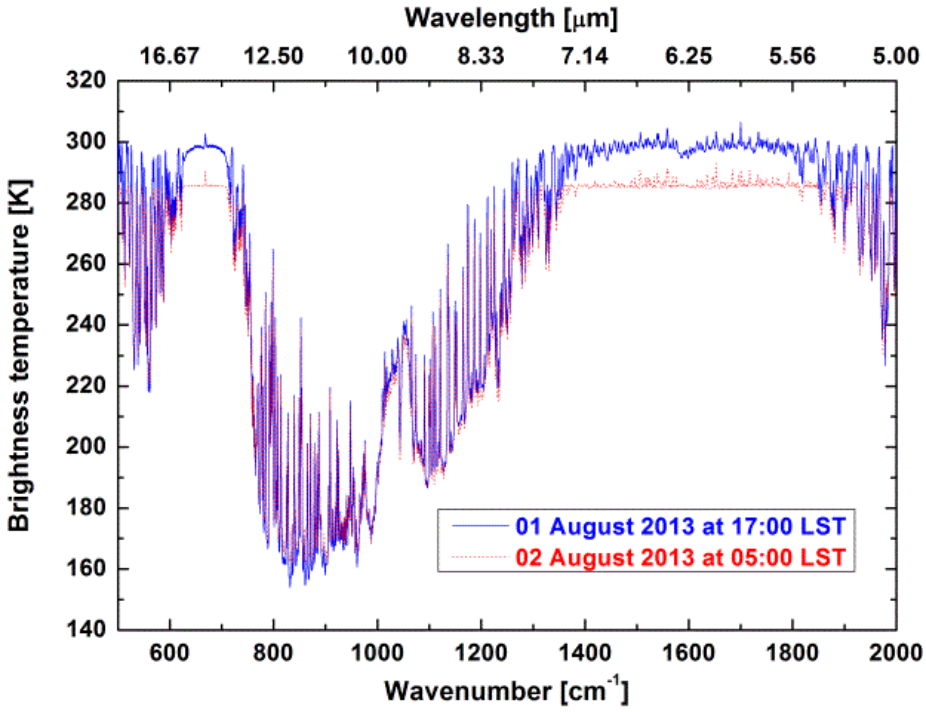

Figure 5.2b Measured brightness temperature spectra on 01 August 2013 at 17:00 LST (blue solid curve) and 02 August 2013 at 05:00 LST (red dotted curve).

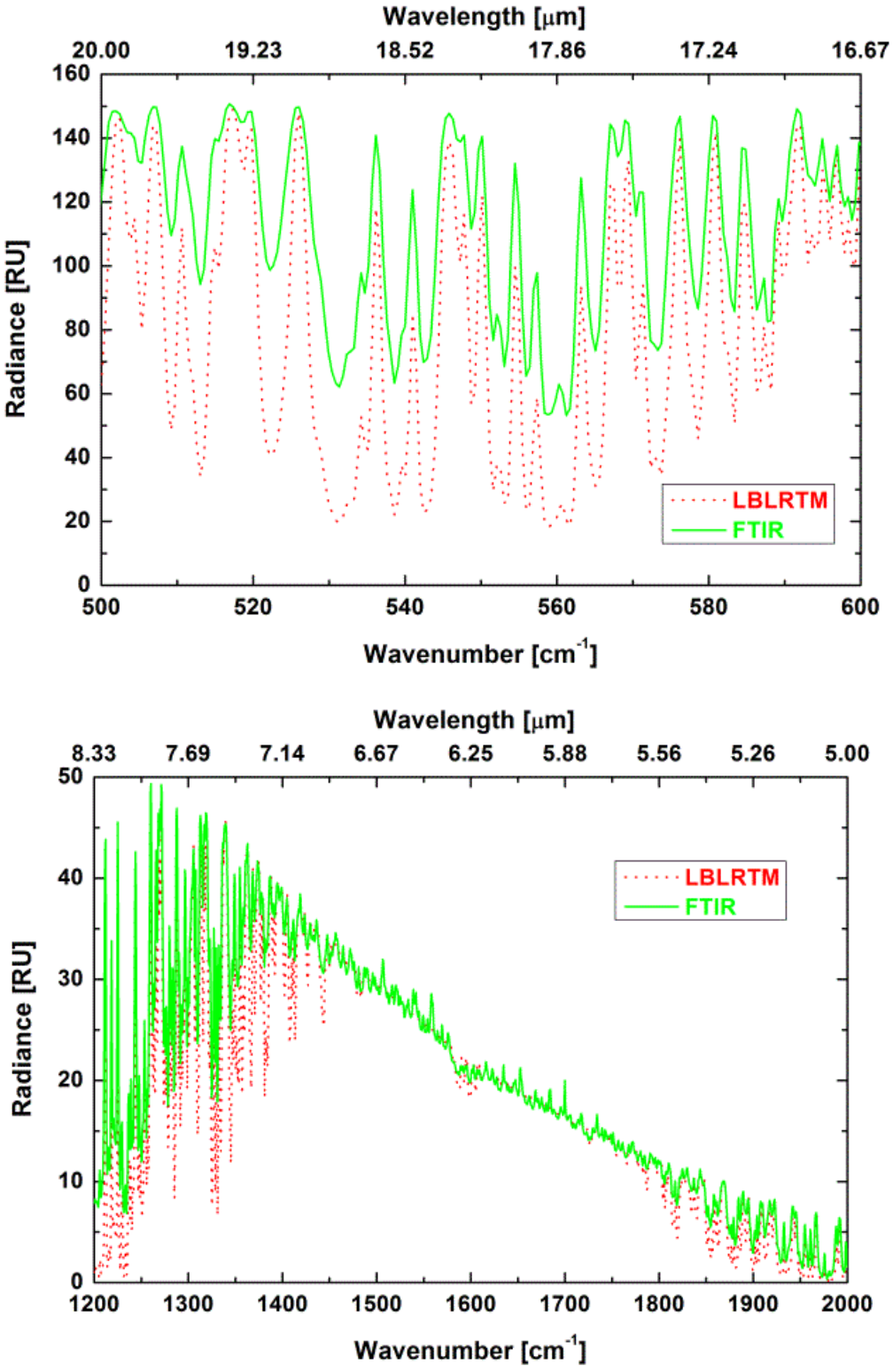

Figure 5.2c Expansion views of Fig. 4.4 (left) for the H_2O vapor bands. The upper panel refers to the region 500-600 cm^{-1} and the lower panel the region 1200-2000 cm^{-1}. A radiance unit (RU) is 1 $mW/(m^2\ Sr\ cm^{-1})$.

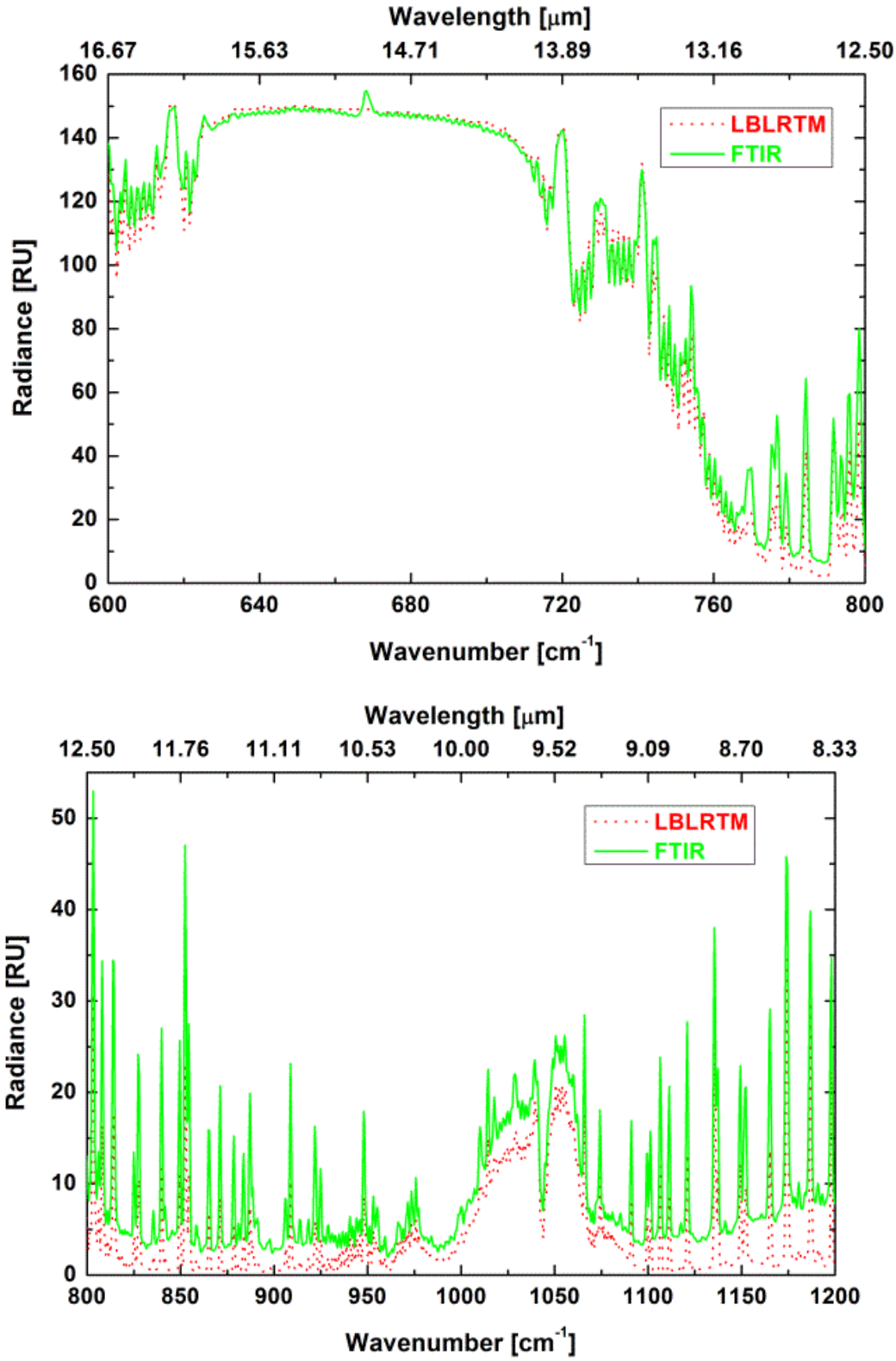

Figure 5.2d Expansion views of Fig. 4.4 (left) for the CO_2 (top) and window (bottom) regions. A radiance unit (RU) is 1 mW/(m^2 Sr cm^{-1}).

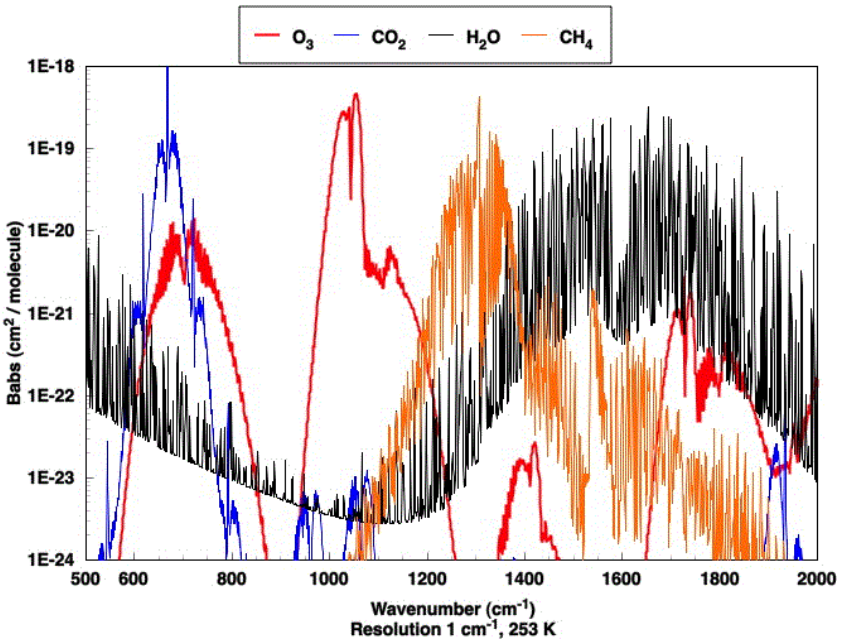

Figure 5.2e Absorption cross-section per molecule of greenhouse gases as a function of wavenumber (courtesy: W. P. Arnott).

The radiance spectra are populated with spectral lines of greenhouse gases such as 15-μm CO_2 band from about 625 to 725 cm^{-1}, 6.3-μm H_2O vapor band from about 1300 to 2000 cm^{-1} and its other band from 500-550 cm^{-1}, and the 8 to 13-μm IR window region from about 800 to 1200 cm^{-1}. The window region contains the 9.6-μm O_3 band from about 1000 to 1100 cm^{-1}. The methane band lies on about 1200 to 1400 cm^{-1}. The H_2O vapor lines are not limited only to the regions mentioned above but are spread throughout the IR spectrum. This information is evident from the Fig. 5.2e which displays the absorption cross section per molecule of various IR active gases as a function of wavenumber. The entire spectra can be studied by splitting them into four main spectral regions.

Both panels of Fig. 5.2c are the expanded views of Fig. 4.4 (left) in the H_2O vapor spectral bands. The amplitude of H_2O vapor lines in the spectral regions 500-600 cm^{-1} and 1200-2000 cm^{-1} depend on the absolute H_2O vapor amounts. The higher the H_2O vapor amount in the lower atmosphere, the more saturated the lines will be. Those saturated lines have variations as we see

in the 1450-2000 cm^{-1} region. The high-variation lines such as in the 500-600 cm^{-1} region are caused by decreased emission strength between the lines, which results from a small amount of H_2O vapor in the atmosphere. This particular region, therefore, indicates the very dry atmosphere of Reno. The radiosonde measured an extreme low amount of precipitable water of 1.48 mm at that time. At $\nu > 1400$ cm^{-1}, the atmosphere is almost opaque due to a fundamental bending mode of the H_2O vapor molecule, and the temperature spectrum yields the temperature of the air as shown also in Fig. 5.2b.

The top panel of Fig. 5.2d represents an expansion view for the CO_2 band and the bottom panel of the same figure is that for the IR window region. In the spectral range 625-715 cm^{-1}, the transmittance of the atmosphere is very low due to absorption by CO_2. CO_2 is an abundant and well-mixed IR active gas in the atmosphere. Thus the air exhibits properties of a blackbody at the temperature of the BL of the atmosphere and the temperature spectrum yields this temperature (see Fig. 5.2b). Since CO_2 exhibits properties of a blackbody in this region, an approximation of the temperature of the surface can be read off the temperature spectrum as the upper boundary in this spectral range. The central portion of the 15-μm band at 668 cm^{-1} is strongly absorbed, and the emission is black at the surface ambient temperature. The distinctive spike at the line 668 cm^{-1} is present only in the measured spectrum. It is attributed to the strong absorption/emission of CO_2 gas present near the instrument and relatively high temperature of the dome-shaped observatory. On each side of the band center, the instrument receives signals from the higher (colder) atmosphere, and hence the instrument measures less radiance. This feature accounts for the decrease in the absorption/emission efficiency of CO_2 away from the band center and emission from the colder atmosphere. That is why the CO_2 absorption/emission region allows the recovery of altitude temperature profile (Adhikari 2012).

The region 800-1200 cm^{-1} is the IR window of the atmosphere with very little emission. The absorption lines in the atmospheric window are caused by H_2O vapor, ozone, CFC-11, CFC-12

and HNO_3. The prominent feature (seen in the lower panel of Fig. 5.2d) between 1000 cm^{-1} and 1100 cm^{-1} is caused by ozone. The spectra are very sensitive to the tropospheric ozone in the center of the ozone band. At $\nu > 1100$ cm^{-1} the transmittance of the atmosphere decreases due to stronger absorption lines of H_2O vapor, CH_4, and N_2O.

We now discuss the discrepancies between the FTIR measurements and the corresponding LBLRTM simulations. Broadly viewing, both the measurement and model seem to have a good agreement qualitatively with each other in the whole range of measurement (Figs. 4.4 (left) and 5.2a), however, there exists a substantial discrepancy quantitatively between them as evident from the residual plot of Fig. 4.4 (right) and the expansion views (Figs. 5.2c and 5.2d).

A large disparity between the simulated and measured spectra seen in the water vapor absorption band (500-600 cm^{-1}) is associated with the large temporal and spatial variability of water vapor in the atmosphere. The water vapor profile from the radiosonde, which was input to the model, may not exactly represent the profile right above the instrument. In the 15-μm CO_2 absorption band, the absorption almost gets saturated and, therefore, we can hardly detect the differences between the model and measurement. The disagreement in the window region (800-1200 cm^{-1}) may be associated with various factors: the water vapor continuum may not be well represented in the line parameter database, the US standard 1976-ozone profile used in the model may not accurately represent the ozone profile of the measurement site, using emissivity of one for calibration-blackbodies may overestimate the radiance during calibration, and aerosols present in the so-called clear atmosphere may likely contribute to the radiance. FTIR calibration and measurement uncertainty is discussed further in Appendix A. Beyond 1200 cm^{-1}, there is a contribution from CH_4, CCL_4, F11, F12 etc. The model also ignores contribution from these species and shows less agreement with the measurement. Overall, these results show a reasonable agreement between the observed and simulated radiance. The discrepancy is likely due to the lack of aerosol in the model. The next two chapters include aerosol.

6 A CASE STUDY OF THE CALIFORNIA RIM FIRE EVENT IN AUGUST 2013

6.1 Observations of the Rim fire event in Reno

The Rim fire event took place at Sierra Nevada region and parts of California on 17 August 2013 and lasted until 06 September 2013. It was the biggest wildfire in the Sierra Nevada and the third largest in California's history, and burned about 1041 km^2. The extreme drought conditions, the widespread heat wave, and winds favored the rapid spread of the fire. The biomass burning in a forest fire emits and releases large amounts of trace gases such as CO_2, CH_4, N_2O, CO, NO_2, O_3 etc., and aerosols including both fine and coarse particulate matter (Urbanski et al. 2009). The smoke and haze from the Rim fire and the American fire in the Tahoe National Forest caused poor air quality conditions and visibility in Reno (which lies about 240 km North of the fire) as shown in Figs. 6.1 and 6.2. The Washoe County Health District Air Quality Management Division reported the air quality of Reno to be in the unhealthy range during the fire event due to the high concentration of fine particulate matter $PM_{2.5}$ (particles smaller than 2.5 μm in diameter). These are microscopic particles that can travel deep into our lungs and cause people varying degrees of health problems. Li et al. 2003, using transmission electron microscopy, observed that the smoke aerosols from a biomass burning grass in southern Africa contained mostly (70-83%) the potassium salt particles (KCL, K_2SO_4, and KNO_3), and lesser amounts of soot, sea-salts, and organic particles. In contrast, pine forest aerosol composition from the Rim Fire is predominantly organic carbon (Lewis et al. 2008).

A 48-hour backward trajectory analysis of air mass flow arriving in Reno on 26 August 2013 (Fig. 6.3) was performed for three different altitudes (500m, 1 km, and 3 km) using the online version 4 of Hybrid Single Particle Lagrangian Integrated Trajectory (HYSPLIT) model, developed by the Air Resources Laboratory (ARL) of the National Oceanic and Atmospheric Administration (NOAA). HYSPLIT applications include tracking and forecasting the release of pollutants, air-parcel trajectories, volcanic ash, dust, and smoke from wildfires. It uses gridded

meteorological data to drive the trajectories and concentrations either forward or backward in time at a regular time interval (Draxler et al. 2013).

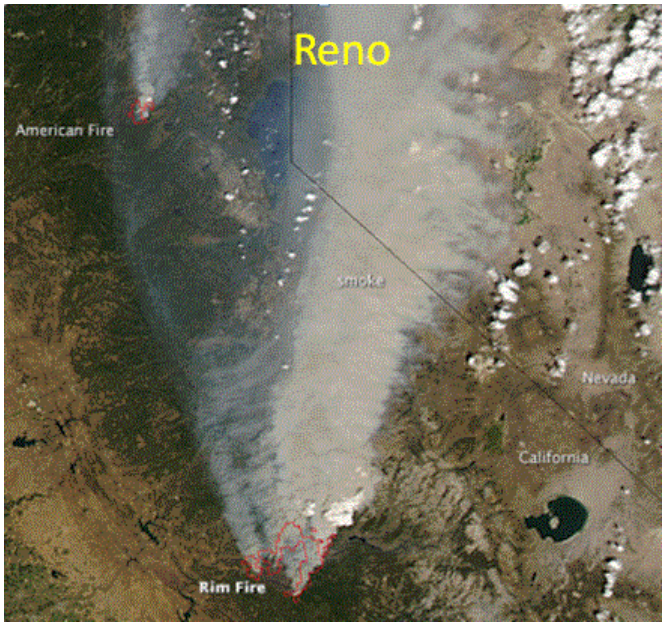

Figure 6.1 Satellite image of the Rim fire on 26 August 2013 (Credit: NASA image by Jeff Schmaltz, LANCE/EOSDIS Rapid Response). Red outlines indicate hot spots where MODIS detected unusually warm surface temperatures associated with fire.

Figure 6.2 Smoke from the Rim fire (about 240 km away) hangs over Reno. The visibility is highly reduced.

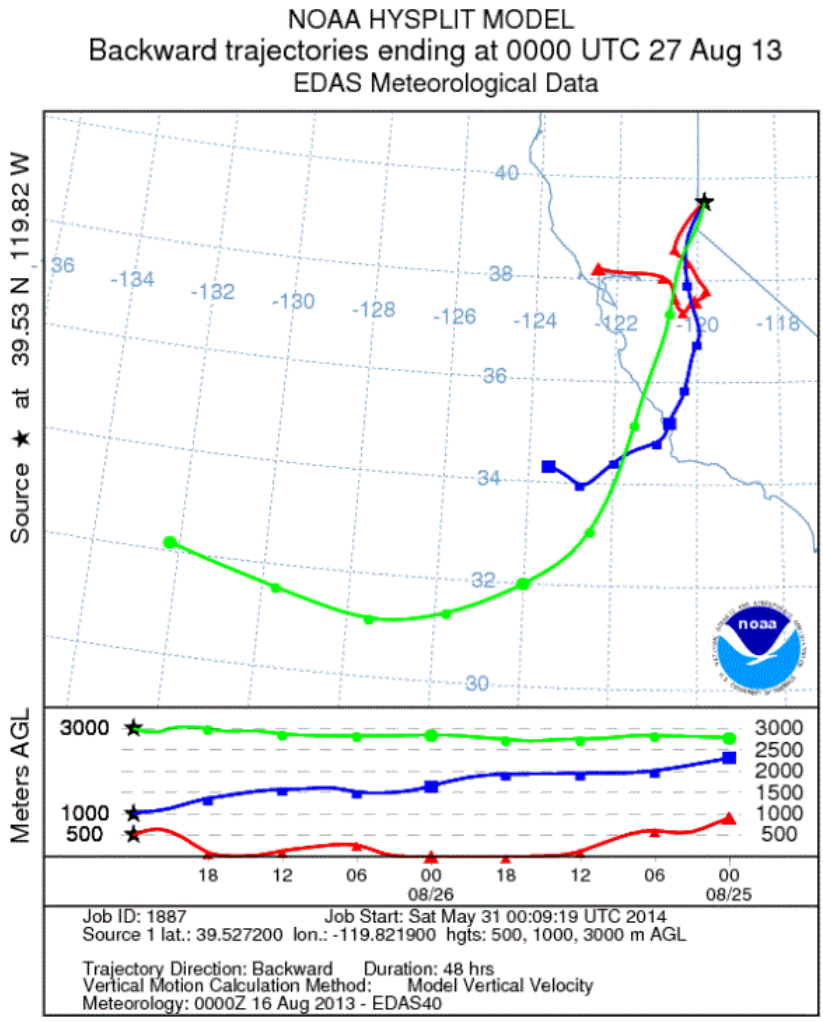

Figure 6.3 NOAA-HYSPLIT 48-hour back trajectories for the air mass ending at 500 m (red curve), 1 km (blue curve), and 3 km (green curve) above Reno at 17:00 LST on 26 August 2013; asterisk indicates the ending point in Reno.

In Fig. 6.3, the red, blue and green lines represent the air-parcel trajectories at the levels of 500 m, 1 km, and 3 km above the surface, respectively. The ending time (27 August 2013 00:00 UTC aka 26 August 2013 17:00 LST) and location (Reno: 39.53° N, 119.82° W) are marked with asterisks in each line. This model is able to clearly demonstrate when and where the air parcels came from. It is obvious that the southwesterly air flow transported the smoke plume from the Rim fire toward Reno. The smoke particles are assumed to be vertically distributed as high as 3 km above

the surface because the boundary layer was well mixed up to that altitude from the surface (source: Reno sounding on 26 August 2013 at 17:00 LST aka 27 August 2013 at 00:00 UTC).

6.2 Microphysical and spectral optical properties of the Rim fire smoke aerosols

The size distribution of 26 August 2013 at 17:00 LST in Reno (Fig. 2.1[left]) is dominated by the fine mode particles with a radius less than 1μm. Even though the size of the fire-emitted smoke particles depend largely on the burning conditions such as burnt material, combustion efficiency, stage of combustion, and chemical and physical transformations that take place during transport, the freshly emitted smoke particles contain mainly fine mode particles (< 1 μm) with approximately 80-90 % of their mass and a small fraction of coarse mode particles (2-20 μm) (Hodzic et al. 2007).

Fig. 6.4 shows the time series of the SW spectral AOD (top panel) and Angstrom exponent parameter (bottom panel) for 26 August 2013. The total AOD at 500 nm (or 0.5 μm) was 1.26 at 17:00 LST. The large value of observed visible optical depth validates the presence of a substantial amount of particles in the atmosphere, which results in the significant extinction of solar radiation. The Angstrom exponent α calculated between two wavelengths, 0.44 μm and 0.87 μm, was 2.4 at that time. The large value of α (≥ 1) is associated with smaller particles mainly issued from combustion processes such as urban or biomass burning aerosols. The sudden drop of α around 21:30 UTC in Fig. 6.4 (bottom panel) could, most likely, be associated with the transient cloud passed by the instrument. Eck et al. 1999 showed that α varies substantially as a function of wavelength for accumulated mode dominated aerosols. The sudden increase in the AOD as well as α values during late afternoon indicates the arrival of a small-sized smoke plume over Reno. The daily mean aerosol AOD usually varies from low (0.05-0.1) to much higher values (0.5-0.8) which are the characteristics of clean and polluted atmospheric conditions, respectively. The AOD values at shorter wavelengths are significant on that day. The AOD values

are low for longer wavelengths. This implies the relative insensitivity of longer wavelengths to small-sized particles.

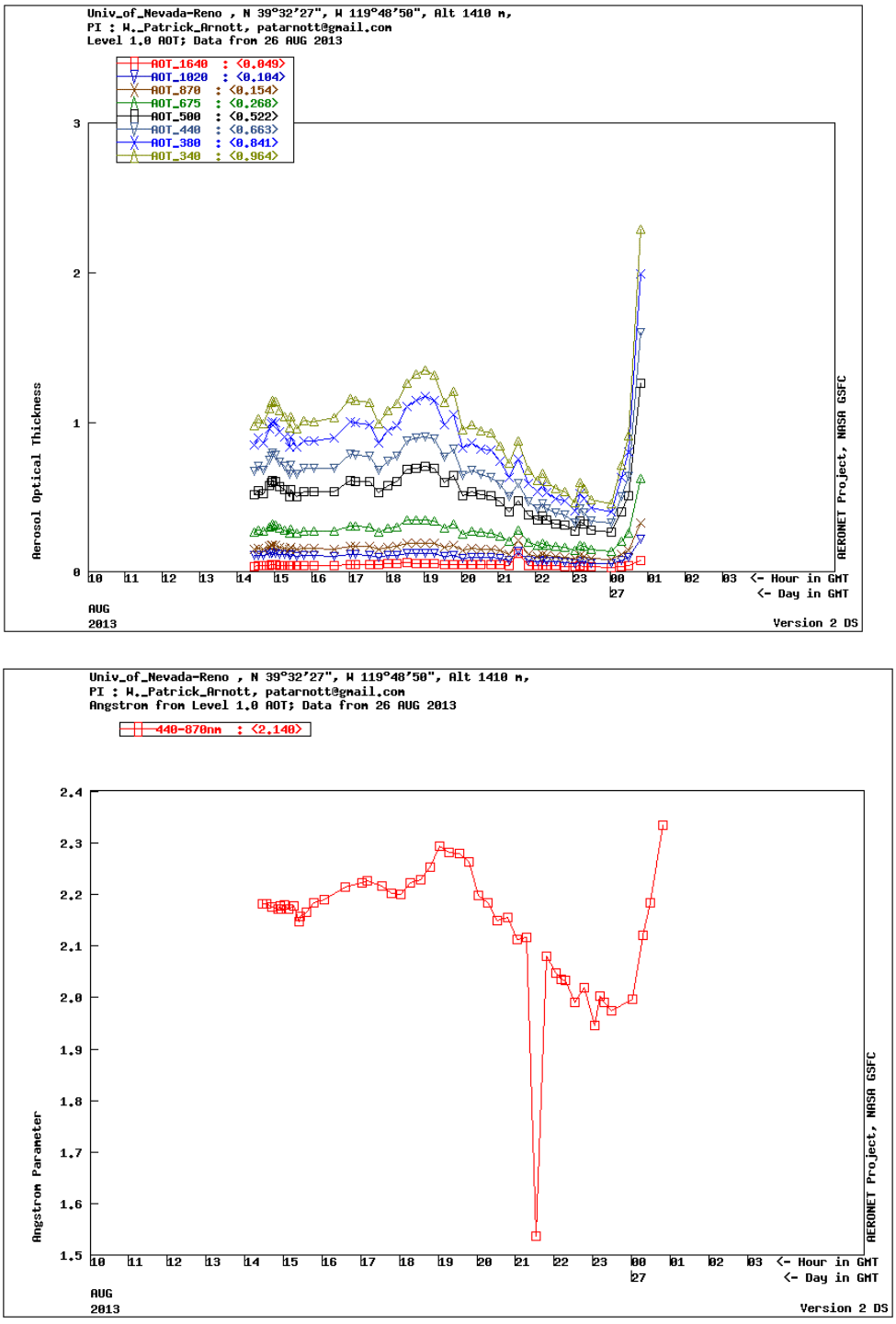

Figure 6.4 Time series of aerosol optical depth (top) and Angstrom exponent (bottom) observed with Cimel sun-photometer on 26 August 2013 (UTC).

The typically measured visible optical thickness at 0.5 μm $\tau_{0.5}$ is translated into the thermal IR optical depth τ_{IR} on the basis of the following relation for the bimodal size distribution:

$$\tau_{IR}^{bimodal} = \tau_{0.5} \frac{\beta_{ext,IR}^{bimodal}}{\beta_{ext,0.5}^{bimodal}}, \quad (6.1)$$

where $\beta_{ext} = \int_{r_{min}}^{r_{max}} Q_{ext}\, A(r)\, n(r)\, dr$ is the extinction coefficient. This quantity is calculated using the Mie theory at both IR and 0.5 μm wavelengths. For unimodal size distribution, either coarse mode or fine mode, the Eq. (6.1) is modified as

$$\tau_{IR}^{unimodal} = \tau_{0.5} \frac{\beta_{ext,IR}^{unimodal}}{\beta_{ext,0.5}^{bimodal}}. \quad (6.2)$$

The IR optical depths at 1100 cm^{-1} were found to be 0.036, 0.030, and 0.006, respectively, for the bimodal and unimodal fine mode and coarse mode size distributions with $\tau_{0.5} = 1.26$.

The optical properties describe the interaction between the aerosols and radiation, which are usually measured in terms of extinction, scattering and absorption efficiencies; single scatter albedo; and asymmetry parameter. These quantities for the smoke aerosols were derived from microphysical quantities such as complex refractive index and size distribution by means of the Mie theory, since the smoke haze particles are largely spherical (Martins et al. 1998). The data for the spectral complex refractive index were taken from the HITRAN aerosol database for both fine mode smoke particles and coarse mode dust particles (i.e., kaolinite).

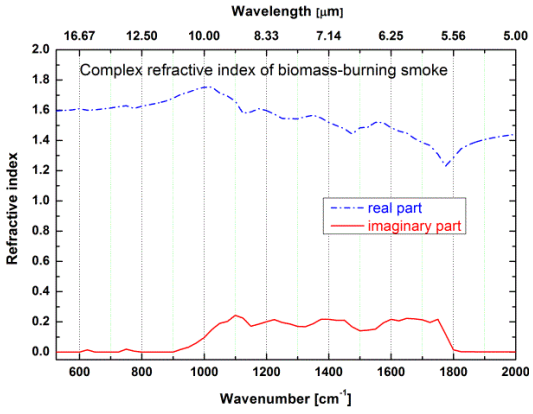

Figure 6.5 Complex spectral refractive index for burning vegetation (source: HITRAN aerosol database; southerlnd_khanna_biomass.dat)

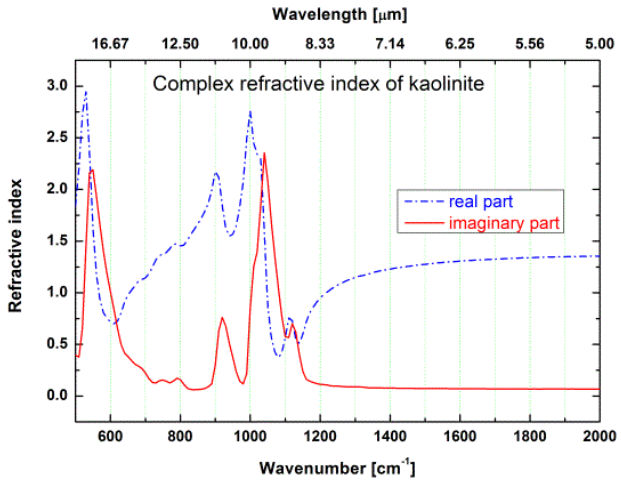

Figure 6.6 Complex spectral refractive index for kaolinite (source: HITRAN aerosol database; querry_minerals.dat)

Figs. 6.5 and 6.6 show the complex spectral refractive index, $N(\lambda) = n_r(\lambda) + i\, n_i(\lambda)$, where n_r is the real and n_i is the imaginary parts, of burning vegetation and kaolinite dust ($Al_2Si_2O_5[OH]_4$), respectively. The original refractive indices in each case were interpolated to get values for our measured wavelengths. The real part of the refractive index determines the (phase) speed of the electromagnetic wave, while the imaginary part, also called the absorption index, is related to the absorption coefficient β_λ through $\beta_\lambda = \frac{4\pi n_i}{\lambda}$ (Liou 1992). The absorption by the particles is, therefore, proportional to the imaginary index of refraction. As seen in Fig. 6.5, the strongest smoke absorption takes place in the range 1000-1800 cm^{-1} and the strongest dust absorption takes place in the regions 500-600 cm^{-1} and 900-1100 cm^{-1} (Fig. 6.6). Real part of the refractive index is mostly responsible for the scattering process.

In this analysis, the fine mode was assumed to consist of solely biomass burning smoke particles and the coarse mode to consist of only kaolinite, and hence the refractive indices were applied accordingly while computing single scattering properties. Furthermore, the single scattering properties were computed using a lognormal size distribution function for all three cases: bimodal distribution consisting of both fine and coarse modes, and unimodal including the fine mode and

coarse mode separately. Unimodal distributions were used to identify the radiative forcing by fine and coarse mode aerosols.

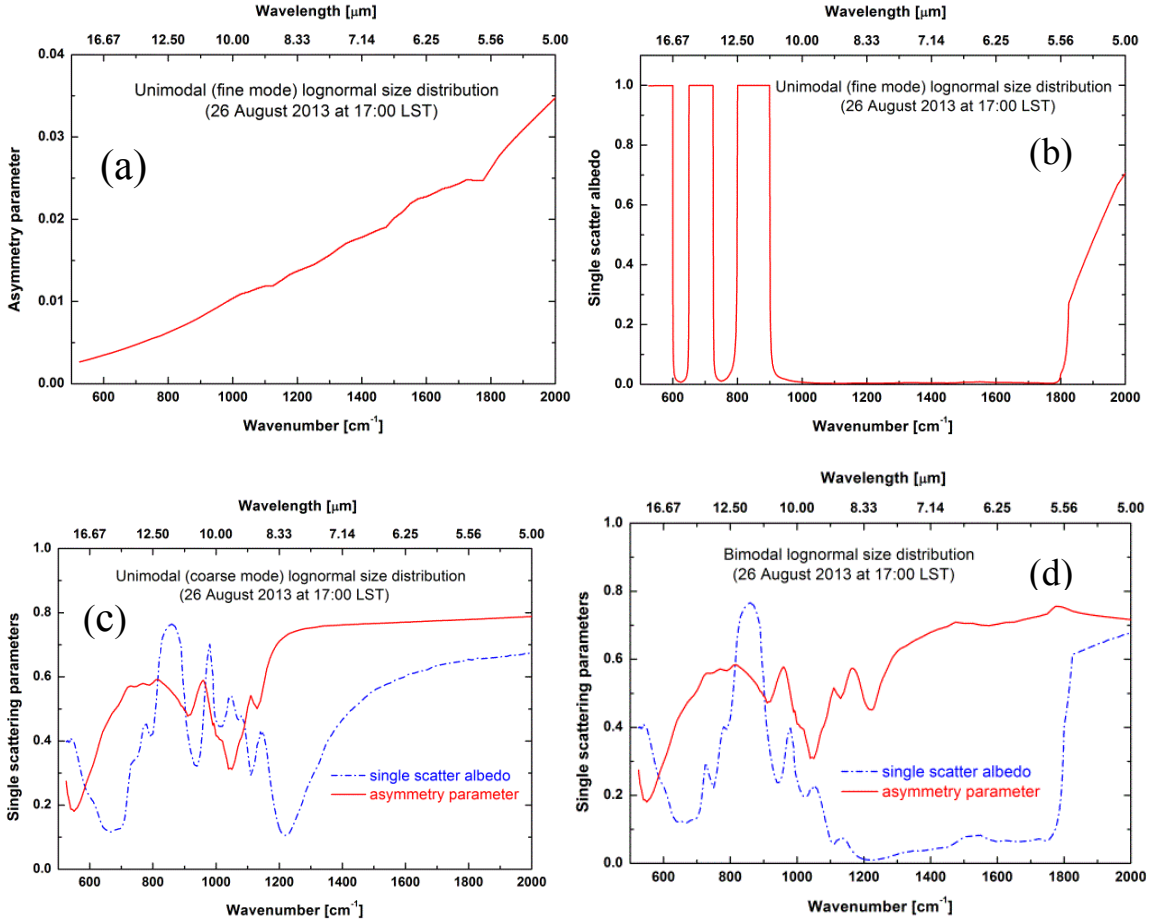

Figure 6.7 Asymmetry parameter (a) and single scatter albedo (b) for fine mode. Parameters for the coarse mode and bimodal size distributions are shown in (c) and (d), respectively, for 26 August 2013 at 17:00 LST.

Figs. 6.7 and 6.8 demonstrate the various single scattering properties of the atmospheric particles present in Reno on 26 August 2013 at 17:00 LST. The asymmetry parameter for the fine mode (Fig. 6.7a) is very small, consistent with the Rayleigh regime, and it decreases monotonically with increasing wavelength. The values of the asymmetry parameter for the coarse and bimodes are much larger than those for the fine mode. The single scatter albedo (ω) of the fine particles (Fig. 6.7b) is quite low in the region where the imaginary refractive index is strong (1000-1800

cm^{-1}), and is a function of wavelength in the region where the absorption is low. The value of ω depends substantially on the imaginary part of the refractive index, while the asymmetry parameter is only weakly sensitive to imaginary part. Since the size parameter of the smoke particles (fine mode) is very small compared to the wavelength, the scattering efficiency is insignificant and the extinction efficiency is close to the absorption efficiency (Fig. 6.8a). All the extinction is due to absorption (ω ≈ 0). Similar features exist in the cross-section parameters as well (not shown). The contribution of the scattering to the extinction increases for the bimodal case (Fig. 6.8c), and is much more significant for the coarse mode (Fig. 6.8b).

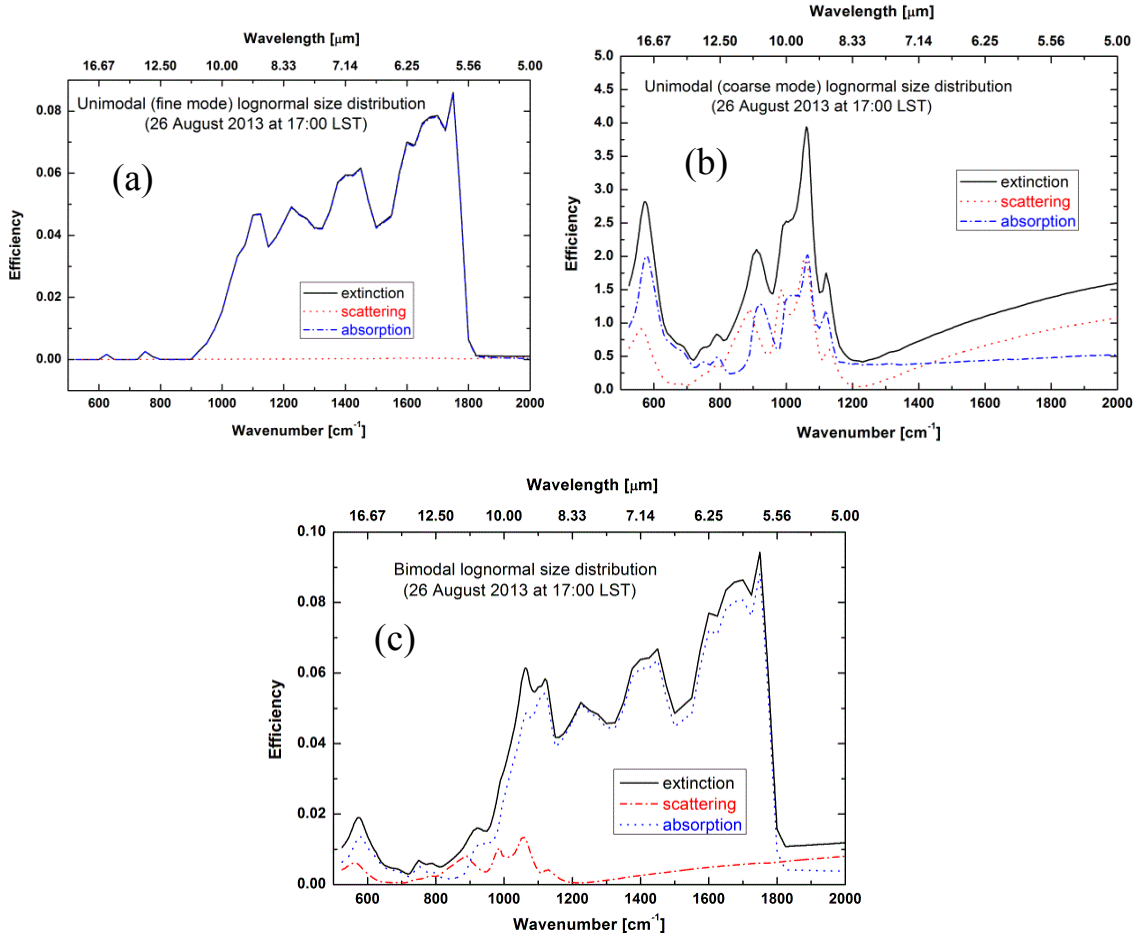

Figure 6.8 Extinction (black solid curve), scattering (red dotted curve), and absorption (blue dashed curve) efficiencies for fine mode (a), coarse mode (b), and bimodal (c) size distributions for 26 August 2013 at 17:00 LST.

The fine mode efficiency plot (Fig. 6.8a) also shows that the scattering effect is negligibly small as compared to the absorption. That is why the zero-scattering approximation can be valid in this case. However, the assumption might produce a large uncertainty while including the coarse mode. The large efficiency values in Fig. 6.8b show that the coarse mode is capable of strongly interacting with LW radiation.

6.3 Thermal radiative properties of the smoke aerosols

This section presents the LBLDIS outputs such as spectral upwelling and downwelling fluxes computed with and without smoke aerosols, and IR radiative forcing (both spectral and broadband) due to the biomass burning particles at the BOA and TOA, in the thermal IR range of 5-20 μm, for fine mode, coarse mode, and bimodal cases, using 119 vertical layers between the ground and 75 km. The smoke layer was assumed to be uniformly distributed up to a height of 3 km above the ground. The gaseous absorption optical depth profile was calculated using the sounding on 26 August 2013 at 17:00 LST (27 August 2013 at 00:00 UTC) in Reno.

According to Fig. 6.9, the coarse mode contribution to the thermal IR fluxes is smaller than the fine and bimodal contribution, and all are non-negligible, especially in the window region (8-12 μm). The bimodal condition accounts for both the fine mode with refractive index of biomass burning vegetation and the coarse mode with the refractive index of mineral dust kaolinite. The increase in the downwelling flux at the BOA (Fig. 6.9a) is caused by the additional downward flux from the aerosol layers. The upwelling flux at the TOA (Fig. 6.9 b) is generally decreased by the aerosols, except when the aerosol is at higher temperature than the surface, such as temperature inversion condition (Markowicz et al. 2003). The aerosol in the nearest 3 km above the ground emits more radiation back to the ground than would be present in clear sky conditions.

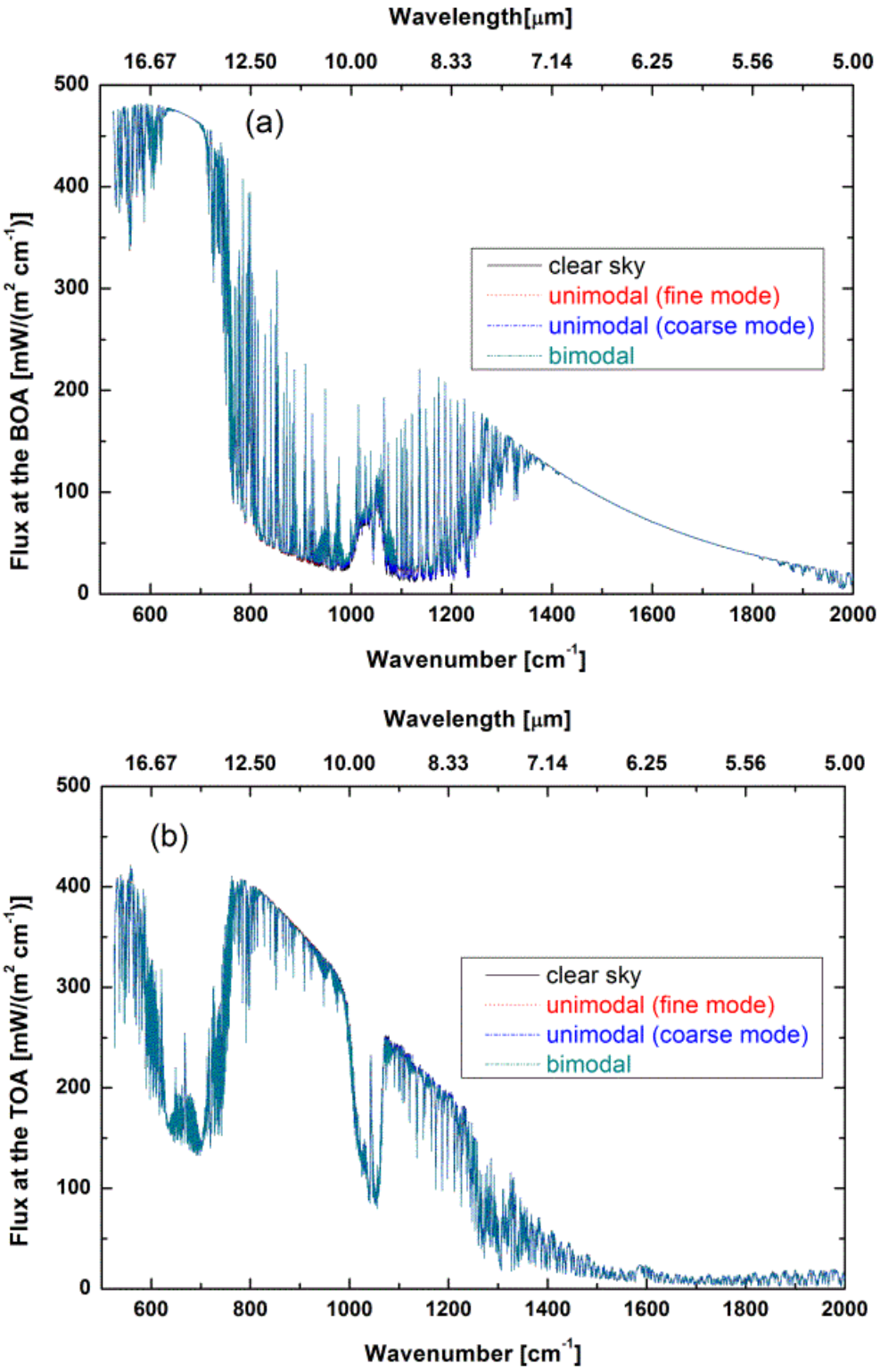

Figure 6.9 Downwelling flux at the BOA (a) and upwelling flux at the TOA (b) for clear sky (black solid curve), fine mode (red dotted curve), coarse mode (blue dashed dot curve), and bimodal (cyan dashed dot-dot curve) conditions.

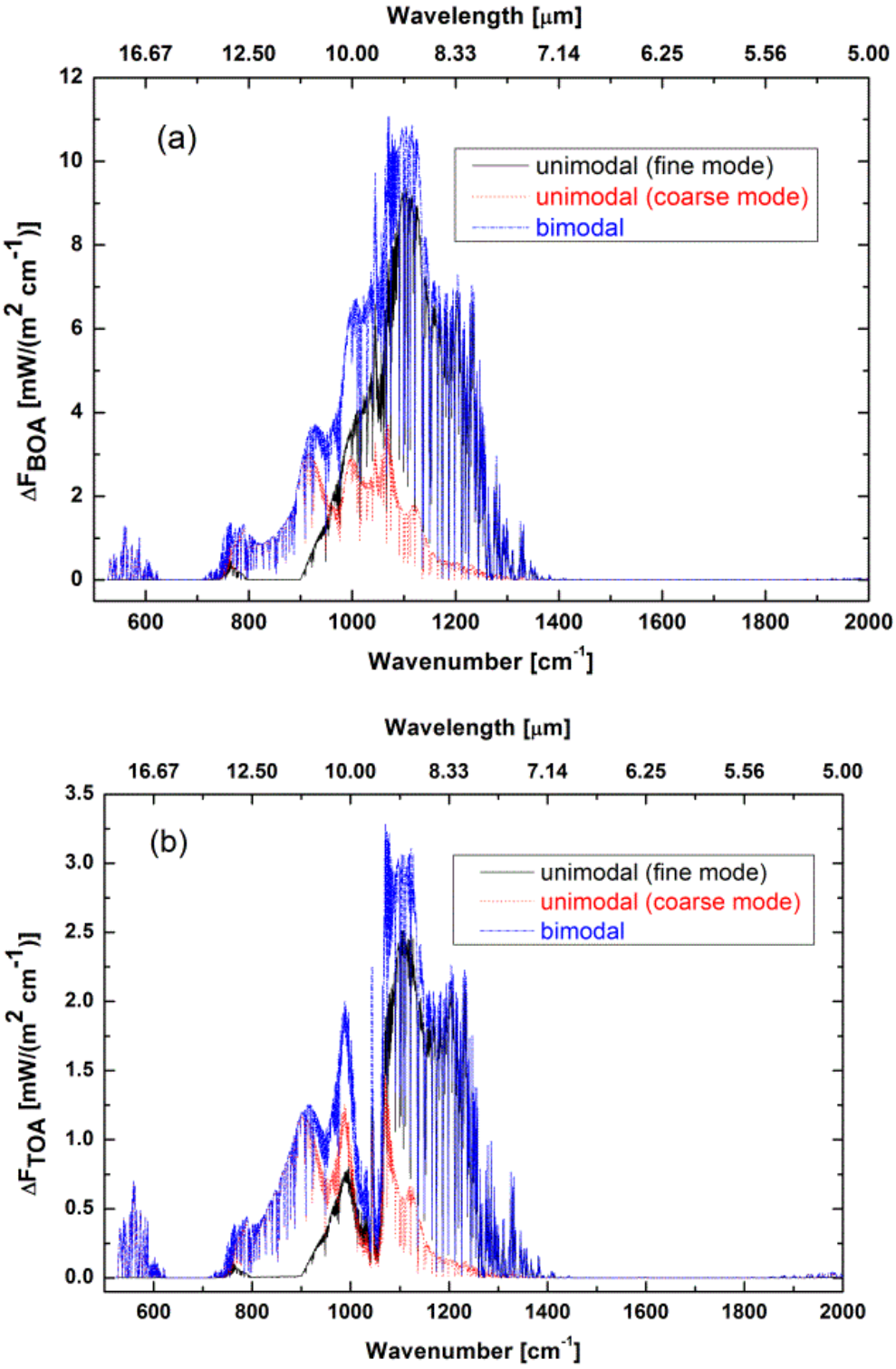

Figure 6.10 Spectral radiative forcing at the BOA (a) and TOA (b) due to fine mode (black solid curve), coarse mode (red dotted curve), and bimodal (blue dashed dot curve) particle size distributions.

Table 6.1 Broadband radiative forcings due to fine mode, coarse mode, and bimodal size distributions in different regions of the thermal IR spectrum

Mode	Spectral range [cm^{-1}]	ΔF_{BOA} [W/m^2]	ΔF_{TOA} [W/m^2]
Unimodal (fine mode)	525-2000	+ 1.57	+ 0.40
	800-1250	+ 1.49	+ 0.37
	525-625	+ 2.10e-04	+ 8.73e-05
Unimodal (coarse mode)	525-2000	+ 0.73	+ 0.27
	800-1250	+ 0.67	+ 0.24
	525-625	+ 2.42e-02	+ 1.59e-02
Bimodal	525-2000	+ 2.28	+ 0.67
	800-1250	+ 2.15	+ 0.61
	525-625	+ 2.45e-02	+ 1.60e-02

Fig. 6.10 and Table 6.1 show the spectral and broadband radiative forcings, respectively, due to the smoke-dominated aerosols, both at the BOA and TOA. These values were calculated using Eqs. 4.4 and 4.5 mentioned in Chapter 4. It is clear that the absorption and emission of the thermal IR radiation by the wildfire emission particles cause a positive radiative forcing (warming) both at the BOA and TOA. These values of the LW forcings are small but not ignorable, because these values are comparable to the direct radiative forcing of + 1.66 [± 0.17] W/m^2 due to increase in CO_2 concentration, from 280 to 379 parts per million by volume (ppmv) since the preindustrial era of 1750 until 2005 (IPCC 2007; Forster et al. 2007). The magnitude of direct aerosol radiative forcing depends strongly on the aerosol optical characteristics, size distribution, and concentration. Sicard et al. 2014 found that for fine mode particles, all extinction is due to absorption and scattering effect has no impact on the IR radiative forcing, consistent with the findings here.

The observation of wildfire smoke properties is complicated by the occurrence of different types of aerosol compounds in it.

Our results are not consistent with the assumption made by Turner 2008, which states that the thermal IR observations are essentially insensitive to biomass burning aerosols as they tend to be fine mode particles, as indicated in Fig. 6.11. The particles lie in the Rayleigh scattering regime and the scattering as well as emission contribution to the downwelling radiance in the longwave is negligible. This makes the IR retrievals of smoke aerosols very difficult.

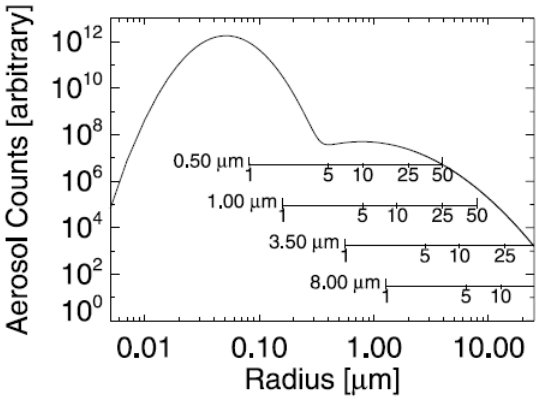

Figure 6.11 Arbitrary bimodal aerosol size distribution with the size parameter for various wavelengths (0.5, 1.0, 3.5, and 8.0 µm) indicated with the horizontal bars (Turner 2008, Figure 5)

Fig. 6.11 was taken from Turner 2008 which illustrates the spectral sensitivity to the size of particles. It is seen that the SW radiation such as 0.50 and 1.00 µm are sensitive to both fine mode (< 1 µm) and coarse mode (> 1µm). In contrast, the LW radiation such as 3.50 and 8.00 µm are not sensitive to the fine mode at all. Our results are based on a heavy aerosol load (concentration of 0.151 $\mu m^3\ \mu m^{-2}$) of fine mode smoke particles which has a substantial contribution to the LW fluxes and forcings. We conclude that the LW effects of the fine mode smoke aerosol, at high concentration, are not ignorable.

6.4 Radiance measurement and simulation results

Fig. 6.12a displays the downwelling radiance spectra measured with FTIR (black solid curve) at 17:00 LST on 26 August 2013 and concurrent clear sky (red dotted curve) and smoke aerosol (bimodal) simulations (blue dashed dot curve). Fig. 6.12b is an expansion view of (a) in the window region.

There is seen a considerable discrepancy between the FTIR-observed radiance spectra and clear sky simulated spectra, especially in the window region. The simulation with bimodal smoke aerosols helps to slightly reduce the discrepancy. The disagreement between the measured and aerosol-simulated spectra may be associated with uncertainties present in both the FTIR measurement and the model computation. The principal observable sources of uncertainties in FTIR spectrometer are the blackbody emissivity and temperature. The uncertainty associated with those quantities is discussed further in Appendix A. The radiative transfer model is likely to possess a variety of uncertainties. H_2O continuum may not be well-represented in the H_2O absorption line parameters. More importantly, there always exists a big uncertainty while modeling the aerosol characteristics such as aerosol type, its composition, shape, size, and complex spectral refractive index. We lack complete knowledge of the aerosol chemical composition and refractive indices, and cannot rule out the possible presence of trace gases during the fire that could contribute to the downwelling IR. Realistic aerosols usually have a complex structure and non-spherical shape despite our assumption that particles are simple, homogeneous, and spherical. The use of the Mie theory will, therefore, produce uncertainty in the particles' single scattering properties, while treating aerosols as homogeneous spheres.

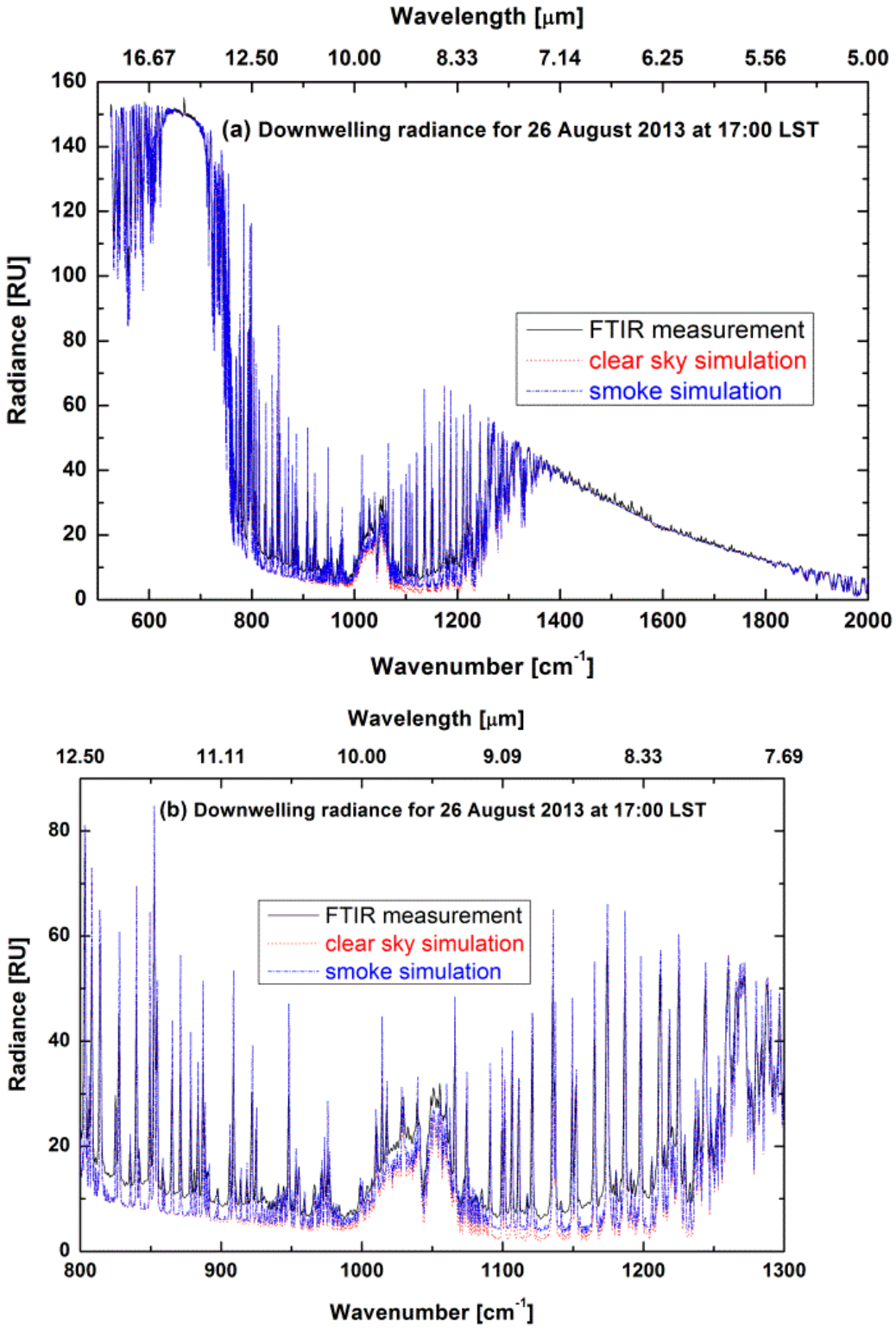

Figure 6.12 (a) Downwelling radiance for 26 August 2013 at 17:00 LST: FTIR measurement (black solid curve), clear sky simulation (red dotted curve), and smoke simulation (blue dotted curve); and (b) expansion view of (a) in the window region.

7 A CASE STUDY OF A DUST STORM EVENT IN RENO ON 24 APRIL 2013

7.1 Observations of dust storm in Reno

The MFRSR-derived size distribution of the dust-dominated particles in Reno on 24 April 2013 at 14:29 LST is shown in Fig. 2.1(right) and the parameters for the size distribution in Table 2.1. The dominating coarse mode distribution is a typical feature of the airborne dust particles. The occurrence of the dust plume is also evident from the Cimel sun-photometer observations of the aerosol optical depth (AOD) (Fig. 7.1, top) and the Angstrom exponent (Fig. 7.1, bottom). During this period, the AOD rises sharply, and the Angstrom exponent drops off to a minimum. The small value of the Angstrom exponent is consistent with the larger-sized particles such as dust. The total AOD at 500 nm (or 0.5 μm) at that time was observed to be about 0.19 with both Cimel and MFRSR, which was twice the AOD observed during non-dust morning hours on the same day. The Angstrom exponent α calculated between two wavelengths, 500 and 870 nm, was 0.23. This also indicates the dominance of large size mineral dust particles, in the atmosphere.

The ARL HYSPLIT backward trajectory analysis (Fig. 7.2, top) was performed at three levels: 500 m, 1 km, and 3 km, for a 46-hour period to analyze the dust storm event in Reno. The air flow was seen to arrive in Reno from the north-east around 14:29 LST on 24 April 2013. We believe that the air flow brought the dust plume to Reno all the way from the Humboldt sink, located in the north-east of Reno at a distance of about 138 km (Fig. 7.2, bottom).

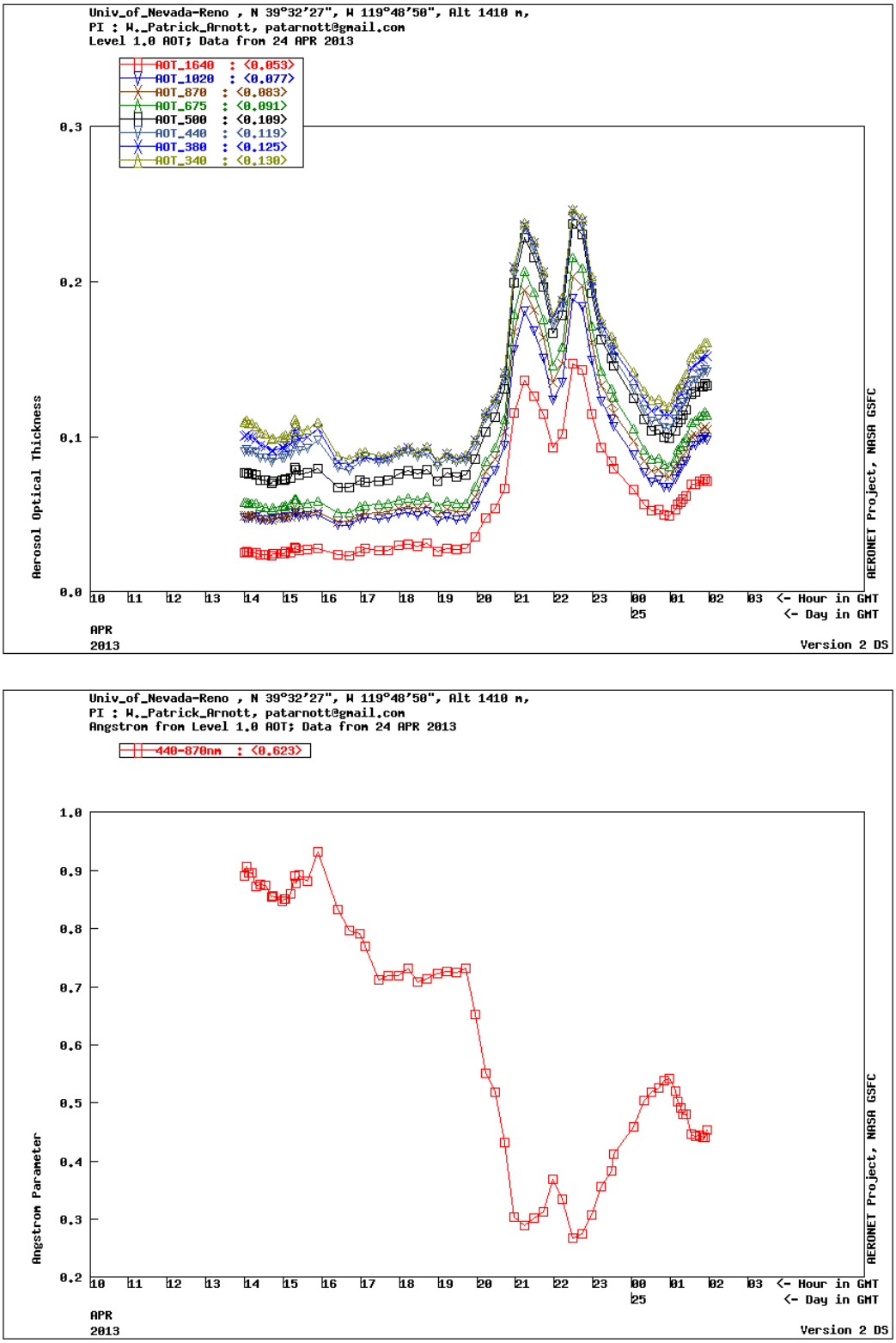

Figure 7.1 Cimel-observed time series spectral AOD (top) and Angstrom exponent (bottom) on 24 April 2013 (UTC).

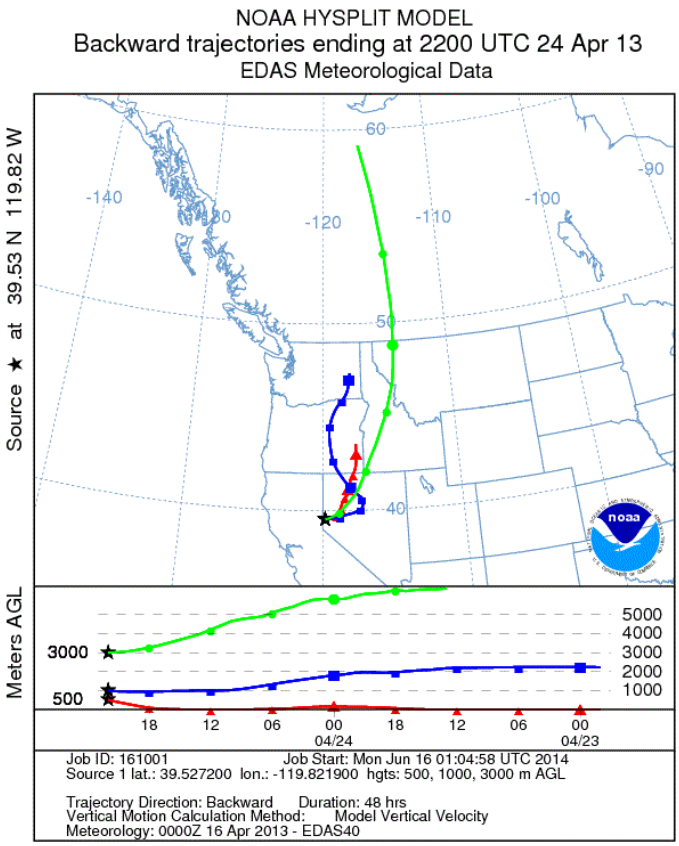

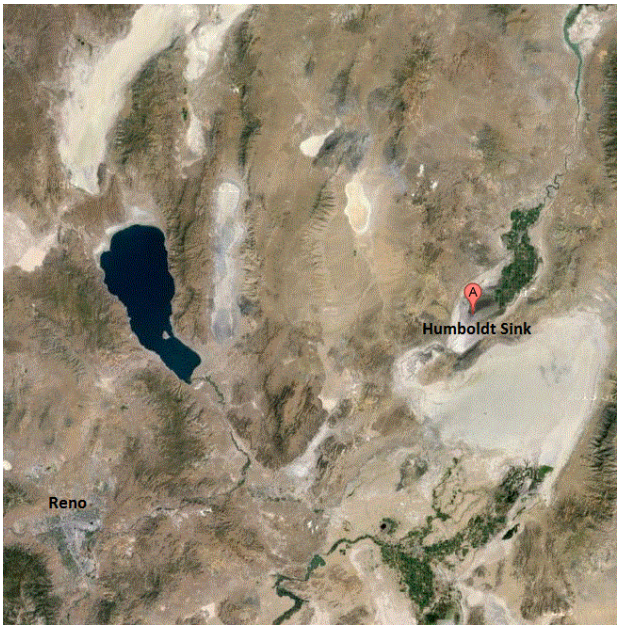

Figure 7.2 (top) NOAA-HYSPLIT 46-hour back trajectories for the air mass ending at 500 m (red curve), 1 km (blue curve), and 3 km (green curve) above Reno at 15:00 LST on 24 April 2013; asterisk indicates the ending point in Reno, (bottom) map showing the locations of Reno (Cimel station) and Humboldt Sink (assumed dust source).

7.2 Microphysical and spectral optical properties of airborne mineral dust aerosols

As shown in Fig. 2.1(right), coarse mode is representative of the dust particles present in the atmosphere over Reno on 24 April 2013 at 14:29 LST. Though the dust particles are composite in structure, we only used kaolinite in our modeling because it is usually known to be the most abundant and a major constituent of the airborne mineral aerosols in terms of its mass fraction (Turner 2008). Although using only kaolinite to model optical properties of the dust can lead to underestimating or overestimating the extinction coefficients (and optical depth) for a given loading, there is no general technique for modeling the optical characteristics of composite particles and there is not enough data on regional and global scales to quantify the mineralogical composition of dust (Sokolik et al. 1999). The coarse mode dust particles were, therefore, assumed to consist only of the kaolinite mineral whose spectral complex refractive index (Fig. 6.6) was used to compute the optical properties. The fine mode of the size distribution was considered to consist of small combustion particles such as biomass burning aerosols and the corresponding refractive index (Fig. 6.5) was used to compute the scattering properties. The refractive index is an intrinsic factor that controls the single scattering properties of a particle. The mineral dust is strongly absorptive in the spectral region at which the imaginary refractive index is high. The imaginary refractive index (solid red curve), which is associated with the absorption of the dust particles, peaks at wavenumbers, 550, 900, and 1050 cm^{-1}. Absorption at 1050 cm^{-1} may be ambiguous due to the ozone absorption near the same wavenumber.

Assuming the dust particles as homogeneous spheres, the spectral optical properties were computed using the Mie theory. The non-sphericity effect of dust particles on the radiative flux is small enough for a good first approximation at the IR wavelengths (Yang et al. 2007; Dufresne et al. 2002). These individual particle properties are then integrated using the unimodal (fine and coarse mode separately) and bimodal lognormal size distribution over the particle size range 0.05-50 μm to compute the mean (or bulk) optical properties. The effective radii were found to be

0.179, 2.269, and 0.812 μm respectively for the fine mode, coarse mode, and bimodal size distributions.

Figs. 7.3 and 7.4 display the optical properties of the modeled particles during the dust event. The optical parameters show strong variations with wavelength. The single scatter albedo (SSA) and asymmetry parameter of the fine mode (Fig. 7.3 [a] and [b], respectively) exhibit the similar features as discussed in the section 6.2. Both the parameters for the coarse mode (Fig. 7.3 [c]) and bimodes (Fig. 7.3 [d]) are very sensitive to the lower wavenumbers (i.e., higher wavelengths) and their variation on shorter wavelengths decreases in each case. The asymmetry parameter (red solid curve) increases at shorter wavelengths as expected, despite some specific ties to absorption bands. The SSA (blue broken curve) also shows fluctuations due to specific absorption features in the mineral. The SSA of the mineral is not very low since it has a large value of both the imaginary and real parts of the refractive index. The value of SSA depends significantly on the imaginary part of the refractive index, while the asymmetry parameter depends weakly on the imaginary part (Sokolik 1993). Aerosols have the asymmetry parameter of about 0.5 in the region 8 to 12 μm and tend to scatter in all direction, with a little more in the forward direction. The bimodal optical characteristics closely resemble the coarse mode optical features because the coarse mode predominates the given size distribution.

Fig. 7.4 shows various specific features in the efficiency spectra of the particles. For the fine mode (Fig. 7.4 [a]), the scattering efficiency (red dotted curve) is very close to zero and all the extinction is due to absorption. For the coarse mode (Fig. 7.4 [b]) and bimodes (Fig.7.4 [c]), the extinction efficiency increases as the SSA and the asymmetry parameter increase. At some wavelengths such as near 8 and 14 μm, the SSA is close to zero and most of the extinction is due to absorption. These are ‘Christiansen Bands’ (Arnott et al. 1994) where the real part of the refractive index (see Fig. 6.6) is unity. At longer wavelengths, the absorption exceeds the scattering, while the opposite effect happens at shorter wavelengths.

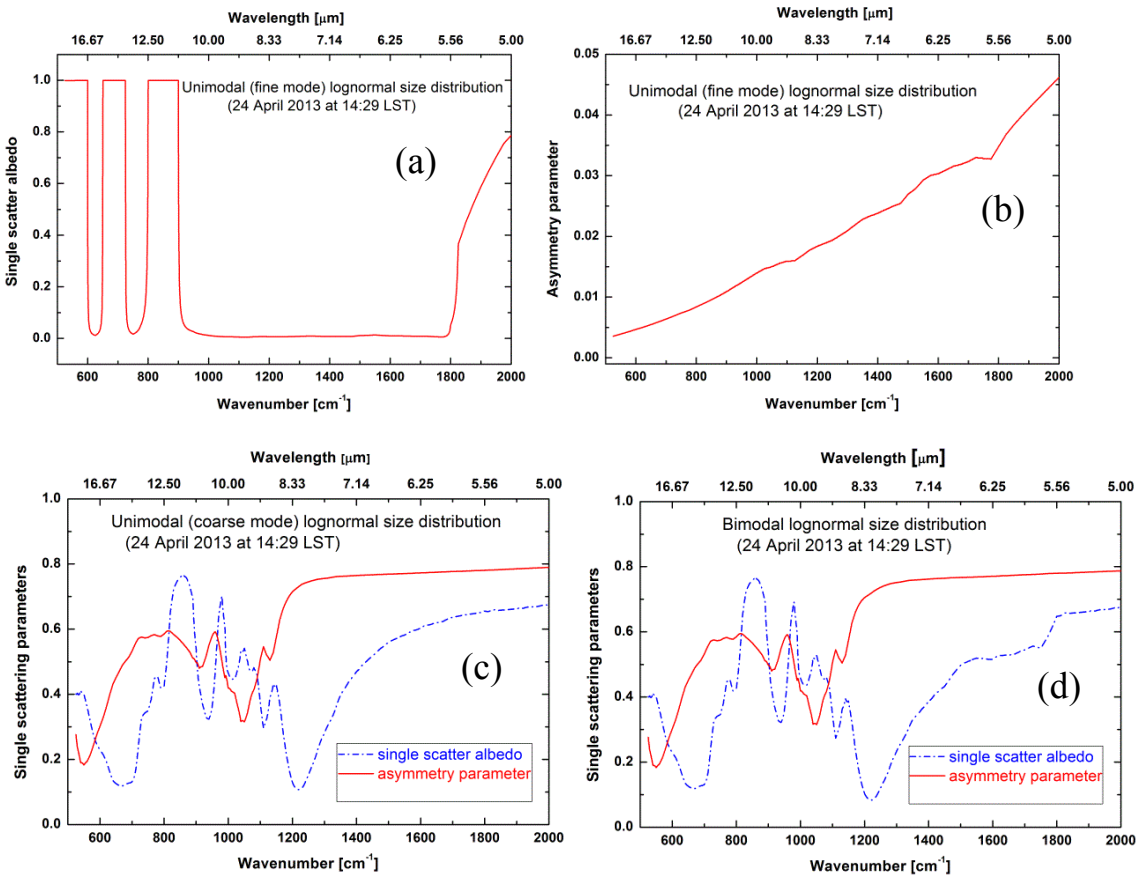

Figure 7.3 Single scatter albedo and asymmetry parameter for fine mode (a) and (b), respectively. The parameters for coarse mode (c), and bimodal (d) size distributions: single scatter albedo (blue broken curve) and asymmetry parameter (red solid curve).

The absorption efficiency (blue dashed curve) mimics the features in the mineral's imaginary refractive index spectrum (Fig. 6.6), i.e. the peaks of absorption efficiency lie at the similar wavenumber where the peaks of the imaginary refractive index are located. Both the efficiencies and cross-sections (not shown) are found to be higher for the coarse mode than for the fine and the bimodal size distributions. The aerosol absorption and scattering of the thermal IR enhances the greenhouse effect of dust.

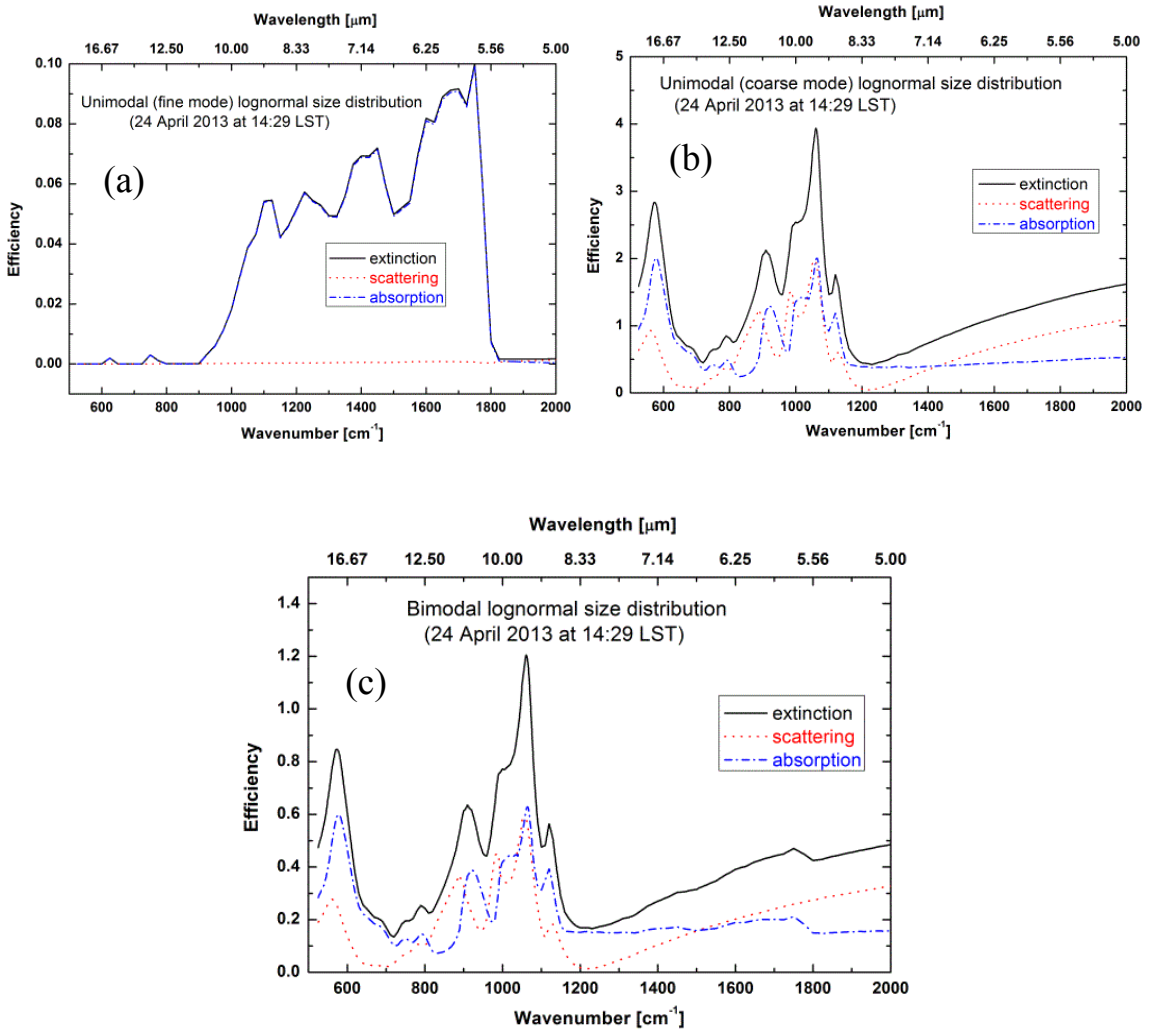

Figure 7.4 Extinction (black solid curve), scattering (red dotted curve), and absorption (blue dashed curve) efficiencies for the fine mode (a), coarse mode (b), and bimodal (c) size distributions.

7.3 Thermal radiative properties of the mineral dust aerosols

Like in the case study of the fire event, the radiative properties such as spectral fluxes, and the spectral as well as broadband radiative forcings both at the TOA and BOA due to the dust-dominated aerosols, for unimodal (fine and coarse mode) and bimodal size distributions, were computed using LBLDIS. Figs. 7.5 and 7.6, and Table 7.1 represent the LBLDIS outputs. In each case, the atmospheric characteristics (pressure, temperature, water vapor profiles, etc.) were taken

from the sounding profile of 24 April 2013 at 17:00 LST. The dust was assumed as a homogeneous layer being vertically distributed up to an altitude of 3 km above the ground. A dust layer at an altitude of 0-3 km may be the most representative case (Tegen et al. 1996).

The upwelling flux at the TOA (Fig. 7.5[b]) would essentially be the flux emitted by the Earth's surface if the gas is perfectly transparent in the thermal IR domain such as the atmospheric IR window region (8-12 μm) and the downwelling flux at the BOA (Fig. 7.5[b]) would be zero in that region. Since the Earth's surface is the principal source of thermal IR and it is usually at higher temperature than the atmosphere in the afternoon, the upwelling flux is larger than the downwelling flux in the IR window region. The presence of highly absorbing mineral dust in the atmosphere nearby the surface leads to the decrease in upward flux, but enhances the downward flux substantially, especially in the window region. This is obvious with the unimodal coarse mode (blue dashed dot curve) and bimodal (cyan dashed dot-dot curve) simulations in each spectrum of Fig. 7.5. Since the dust layer is located near the surface, the increase in the downward flux due to the aerosols is larger than the decrease in the upward flux. Also, the impact of the fine mode particles (red dotted curve) on both the downward and upward fluxes is negligible as compared to the coarse mode and bimodal particles.

It appears clearly from Fig. 7.6 and Table 7.1 that most of the forcing by the dust aerosols takes place in the window region. More than 76 % of the total radiative forcing at the BOA and TOA lies in that region. The radiative forcing at the BOA is much larger than that at the TOA. This is because the absorbing and scattering aerosol layer lies closer to the Earth's surface, the main source of the IR radiation, and IR is reflected, absorbed, and emitted back to the surface by the aerosol layer. The aerosol layer reduces the upwelling IR radiation emitted by the Earth surface via absorption and scattering, thereby decreasing the flux reaching at the TOA. Since the aerosol is at a lower temperature than the surface, the flux increase due to aerosol emission as well as forward scattering cannot compensate this flux loss. The aerosol layer residing at higher altitude

has lower temperature; thus its emission of LW radiation is smaller. The BOA radiative forcing decreases with the height of the aerosol layer, whereas the TOA forcing increases with the height of the aerosol layer (Liao and Seinfeld 1998).

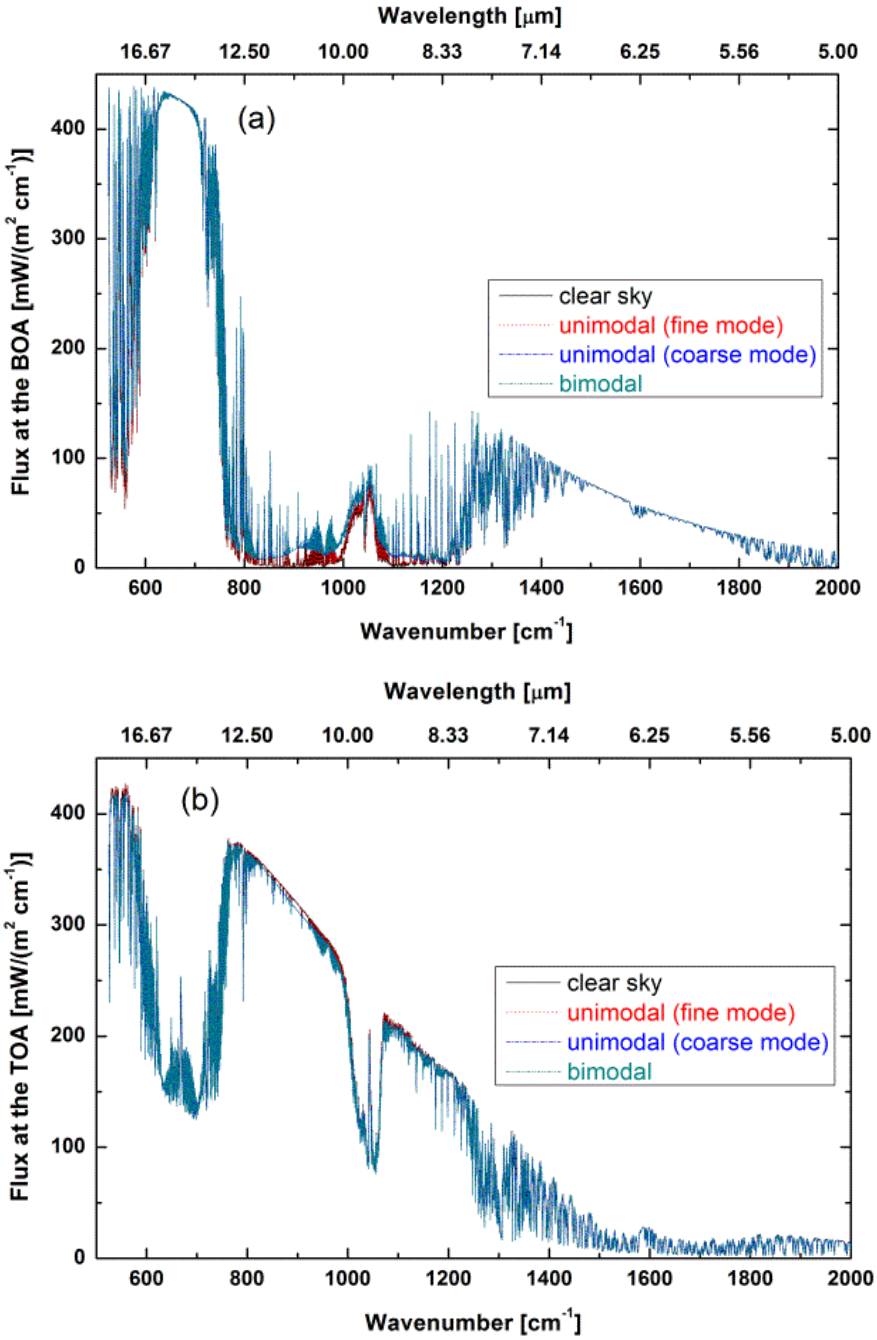

Figure 7.5 Spectral downwelling flux at the BOA (a) and upwelling flux at the TOA (b) for the clear sky (black solid curve), fine mode (red dotted curve), coarse mode (blue dashed dot curve), and bimodal (cyan dashed dot-dot curve) size distributions.

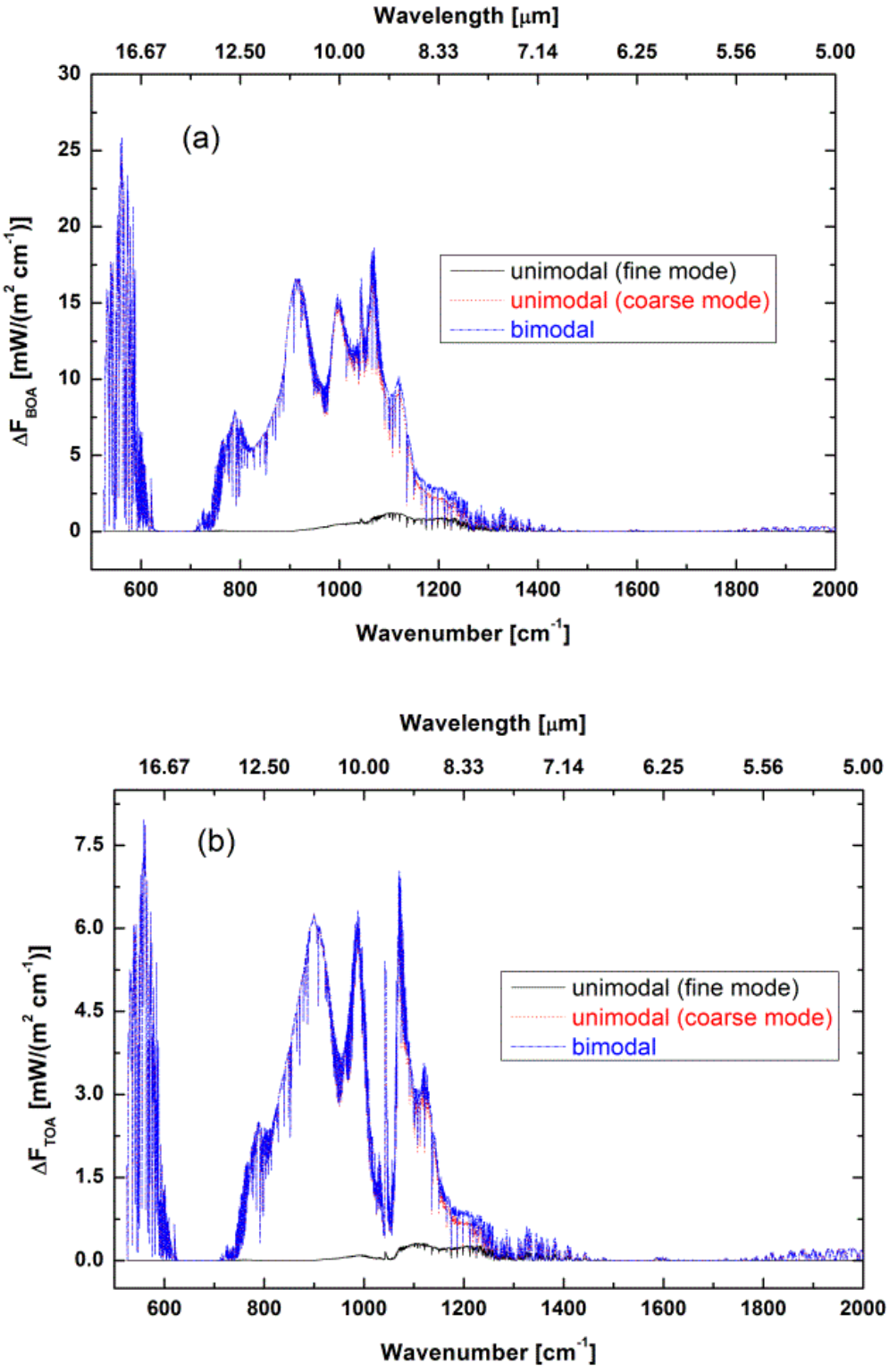

Figure 7.6 Spectral radiative forcing at the BOA (a) and TOA (b) due to aerosols of fine mode (black solid curve), coarse mode (red dotted curve), and bimodal (blue dashed dot curve) size distributions.

Table 7.1 Broadband radiative forcings due to aerosols at different spectral regions for the dust case study

Particle mode	Spectral range [cm^{-1}]	ΔF_{BOA} [W/m^2]	ΔF_{TOA} [W/m^2]
Unimodal (fine mode)	525-2000	+ 0.25	+ 0.06
	800-1250	+ 0.22	+ 0.05
	525-625	+ 8.10e-05	+ 2.24e-05
Unimodal (coarse mode)	525-2000	+ 5.02	+ 1.71
	800-1250	+ 3.78	+ 1.32
	525-625	+ 0.86	+ 0.27
Bimodal	525-2000	+ 5.20	+ 1.76
	800-1250	+ 3.93	+ 1.35
	525-625	+ 0.86	+ 0.27

The coarse mode alone contributes more than 95 % of the total bimodal radiative forcing at the BOA and TOA. Since the absorption and scattering efficiencies increase with increasing particle size, the IR radiative forcing both at the BOA and TOA increases with particle size (Sicard et al. 2013). The significant positive values of the radiative forcing cause the heating effect in the LW spectral region.

Aerosol emission has little to no impact on the spectral fluxes at, or near the major gas absorption bands such as CO_2 [15 μm], H_2O [6.3 μm] and O_3 [9.6 μm] due to the dominant emission from these gases. The aerosol radiative forcing is large in the atmospheric window region, but almost zero in the major gas absorption bands. The thermal IR radiation near the surface is mostly dominated by the emission from water vapor and CO_2. There is also a significant impact of the large particles on the radiative forcing in the 15 to 20 μm range. Since the emission is dominated

by coarse mode particles, there appears no significant difference between the radiative forcing due to the unimodal coarse mode and bimodal size distribution.

Sicard et al. 2014 observed the LW radiative forcing of + 6.02 W/m^2 at the BOA and + 3.58 W/m^2 at the TOA for their mineral dust model. Also, they found that the LW BOA radiative forcing varied between +2.8 and +10.2 W/m^2 with a mean value of + 6.0 W/m^2, while the LW TOA radiative forcing varied between + 0.6 and + 5.8 W/m^2 with a mean value of + 2.6 W/m^2, for 11 dust outbreaks observed in Barcelona over the period 2007-2012. These values depend on a variety of factors such as mineral dust model (refractive index, size distribution, vertical distribution, fine and coarse mode radii and their concentration, etc.), surface temperature, surface albedo, AOD at 500 nm, spectral range (ours is 5-20 μm, theirs is 4-50 μm), aerosol height or aerosol temperature, the radiative transfer model used (line-by-line, or narrow/broadband model), and finally the humidity of the atmosphere. Despite several degrees of freedom just mentioned, our model results are comparable to the results of Sicard et al. 2014.

7.4 Sensitivity of dust IR radiative forcing to atmospheric humidity

Eq. 2.29 explains the influence of water vapor content in the atmosphere on the radiative forcing due to coarse mode aerosols such as airborne mineral dust particles. The water vapor absorption optical depth $\tau_{abs}^{H_2O}$ increases with humidity, which results in the decrease in the both BOA and TOA radiative forcing. An analysis has been conducted to examine the theoretical prediction and to quantify the effect.

We chose a typical aerosol size distribution (Fig. 7.7) observed with the AERONET sun-photometer on 24 April 2013 at 08:00 LST. This is early morning before the dust event described in the previous section. The aerosol characteristics of this distribution (Table 7.2) were then used to compute the BOA and TOA radiative forcings using two different atmospheric sounding profiles, a very dry sounding of 24 April 2013 at 17:00 LST having precipitable water (PW) of

1.32 mm (Fig. 7.8) and the same sounding with the relative humidity (RH) profile increased by 10% for each layer of the sounding so that the sounding becomes less dry or 'wetter' (not shown).

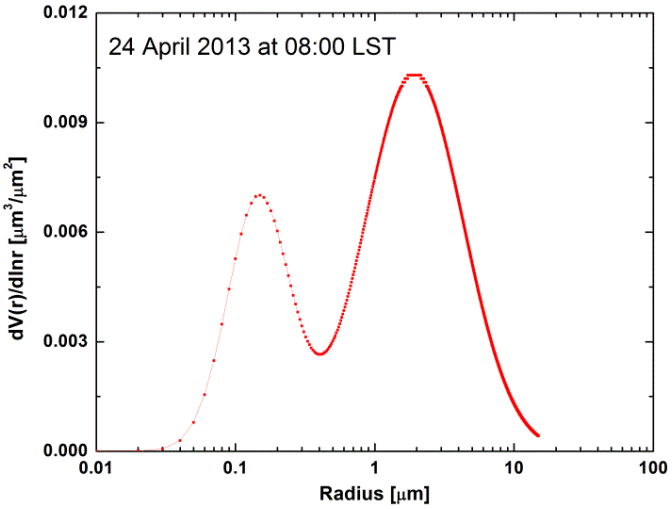

Figure 7.7 AERONET-observed size distribution on 24 April 2013 at 08:00 LST. This size distribution is assumed to be a representative of typical aerosol size distributions in Reno.

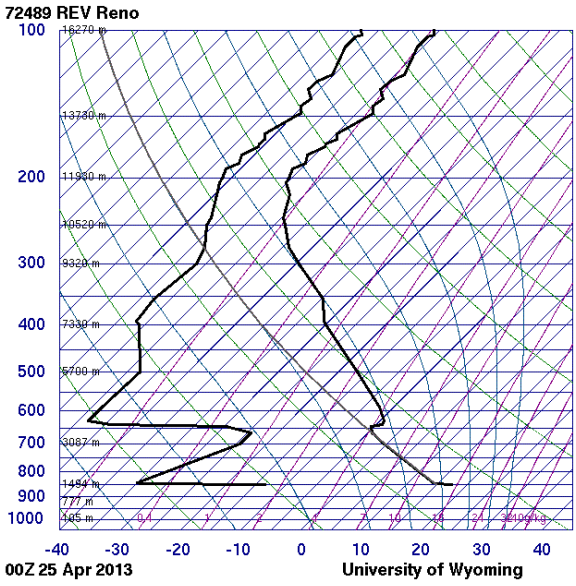

Figure 7.8 Reno's sounding profile on 24 April 2013 at 17:00 LST (PW=1.32 mm).

Table 7.2 Size distribution parameters for Fig. 7.7

Particle mode	Concentration ($\mu m^3\ \mu m^{-2}$)	Median radius (µm)	Standard deviation
Coarse	0.021	1.922	0.811
Fine	0.009	0.147	0.517

The aerosol was again modeled exactly the same way as discussed in sections 7.2 and 7.3, with AOD of 0.08 at 500 nm, to derive the optical and radiative properties. The 500 nm refractive index was taken from the Cimel retrieval and was $n_r = 1.48$ and $n_i = 0.0082$. Table 7.3 summarizes the broadband (5-20 μm) radiative forcings due to the coarse mode particles for the dry and wetter atmospheres.

Table 7.3 Radiative forcings due to aerosols in the dry and humid atmospheres

Type of atmosphere	ΔF_{BOA} [W/m^2]	ΔF_{TOA}[W/m^2]
Dry	1.30	0.40
Wetter	1.28	0.39

The BOA forcing decreases by 1.54 % and the TOA forcing by 2.5 % for the wetter atmosphere with respect to the dry atmosphere. These values reduced by 4.6 % and 5.0 %, respectively, when the RH of the dry sounding was increased by 50% in each layer. Hence the radiative forcings due to aerosols are somewhat larger in the dry atmosphere than in the moist atmosphere i.e., 'the drier the atmosphere, the stronger the LW radiative forcing of dust aerosol' (Liao and SeinFeld 1998). Also, the effect of dryness of the atmosphere is seen more on the TOA forcing than on the BOA forcing.

An increase in RH will significantly enhance the water vapor emission in the thermal IR and increase in aerosol optical depth by particle growth. A higher humid atmosphere makes the modeling of the aerosols more complex and difficult since the water vapor can significantly modulate the aerosol properties such as size distribution, refractive index, extinction efficiency, etc. (Lubin et al. 2002). Because the aerosol microphysical as well as radiative properties depend substantially on the humidity, dry-desert atmospheric condition of the Great Basin in the USA can be more appropriate, as a natural laboratory, to study the climatic effect of dry-aerosols. One

very important observation is that 24 April 2013 is just a typical day in Reno. Yet the TOA radiative forcing by coarse mode aerosol is 0.4 W/m^2. The LW radiative impact is important even on typical days.

7.5 Aerosol IR backscattering effect on the longwave radiative forcing

Fig. 7.9 illustrates the effect of scattering and absorbing aerosols versus scattering only aerosols on the Earth's radiation field.

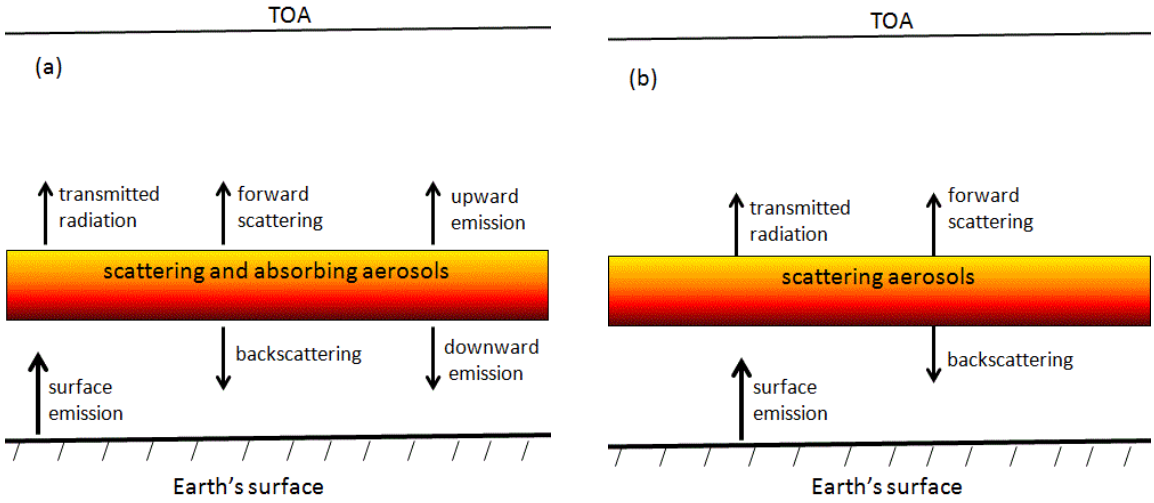

Figure 7.9 Aerosol IR scattering effects: model atmospheres with scattering and absorbing aerosols (a) and scattering only aerosols (b).

In the presence of scattering and absorbing aerosols in the atmosphere (Fig. 7.9a), the LW radiation emitted by the surface is reflected back and absorbed and reemitted through a combined process of scattering and emission. The result will be an increase in both the upwelling and downwelling LW fluxes. This causes BOA forcing to increase, but the TOA forcing to decrease. On the other hand, if scattering only aerosols are present in the atmosphere (Fig. 7.9b), the emission contribution to the fluxes becomes zero. In this case, both the upwelling and downwelling fluxes decrease. Consequently, BOA forcing decreases, but **the TOA forcing increases**. The backscattering of the upwelling LW flux emitted by the Earth's surface is the

main effect of the aerosol scattering, and this effect is most prominent in the IR window region (Dufresne et al. 2002)

In order to quantify the aerosol IR backscattering effect on the IR radiative forcing, the imaginary refractive index of the coarse mode aerosol (mineral kaolinite) of Fig. 2.1[right] was set to a very small value of 1.0e-08 at all IR wavelengths (5-20 μm) so that the mineral dust could represent scattering only aerosols. The dust case study of section 7.3 was reworked with non absorbing aerosol. The single scattering properties of the aerosols were reevaluated with the adjusted imaginary refractive index, which were used to compute the BOA and TOA radiative forcing. The dry sounding of 24 April 2013 at 17:00 LST was used for the gaseous optical depth profile. The LBLDIS outputs of the broadband IR radiative forcing for the scattering aerosols are displayed in Table 7.4.

Table 7.4 Aerosol IR backscattering effect on the thermal IR radiative forcing

Spectral band (cm^{-1})	ΔF_{BOA} [W/m^2]	ΔF_{TOA} [W/m^2]
525-2000	3.15	2.63
800-1250	2.54	2.13
525-625	0.12	0.10

A comparison of the radiative forcing values for the coarse mode in Table 7.1 and Table 7.4 indicates that the aerosol backscattering effect contributes as much as 67% of the total forcing at the BOA, and 58 % of the total forcing at the TOA. The IR scattering effect of the coarse mode aerosols, therefore, plays an important role on the radiative forcing even though the aerosols have a very small, or no absorption at all. This result is consistent with our theoretical analysis in section 2.4. Comparing the bottom right cell of Table 7.1 with the right column in Table 7.4, it is to be noted that scattering only-coarse mode aerosol have a larger TOA radiative forcing than absorbing aerosol because of the argument of Fig. 7.9.

8 DISCUSSION, CONCLUSIONS, AND FUTURE WORK

8.1 Discussion

A few case studies were performed using measurements and radiative transfer models to study the thermal infrared (IR) properties of the atmospheric greenhouse gases and aerosols such as biomass burning smoke particles and wind-blown mineral dust particles, and estimate the direct longwave (LW) aerosol radiative forcing in the spectral region (5-20 μm) in cloud-free atmospheric conditions. The aerosol properties are based on the size distribution of the particles observed with the AERONET Cimel sun-photometer at UNR. These properties are highly dependent on the multitude of factors such as morphology, size, chemical and mineralogical composition of the aerosols.

Simulations of the aerosol IR optical and radiative properties possess a large uncertainty owing to several reasons: poor knowledge of the composition of aerosols and their spectral refractive indices, uncertainties in the vertical distribution of aerosols in the atmosphere, uncertainties in the aerosols properties due to their very complex structure and highly variable characteristics over time and space in terms of their life span in the atmosphere and modification to their physical (shape, size) and chemical (composition) properties during transport, lack of local and regional data of the aerosol properties in the LW spectral region, and errors in the visible optical depth estimates. The poor representation of a modeled aerosol may eventually lead to a significant inaccuracy in the final computational outcomes. For example, assumption of spherical geometry for dust aerosols in computing their optical properties would result in an error in dust radiative forcing (Yang et al. 2007). Since spherical geometry has the maximum amount of tunneling (interaction of a particle with radiation outside its area cross-section), any deviation from spherical shape reduces tunneling efficiency, which leads to an underestimation of the extinction of any particle (Mitchell et al. 2001). According to Tegen et al. 1996, the net (solar plus thermal IR) radiative forcing due to dust can be either positive or negative depending on the size

distribution of the dust particles, their optical depth, mineralogical composition, and vertical distribution. Despite many uncertainties, many LW radiative features of the aerosols have been resolved in this work.

8.2 Conclusions

Study of the aerosol IR optical properties are important to radiative transfer simulations, climate modeling, and remote sensing implementation. We found that the LW radiative forcing by the fine mode smoke aerosols is small and positive; however, it is as large as the IR radiative forcing due to the increase in CO_2 concentration since 1750. The LW radiative forcing due to large, highly absorbing and scattering mineral dust aerosols was found to be significant and positive. The positive radiative forcing of the aerosols in the LW region contributes to partially counteract the strong aerosol cooling effect in the SW region. Since the atmospheric mineral dust can have a large impact on the LW radiative fluxes and because it is wide spread in the Earth's atmosphere, it is essential to include dust aerosol direct IR radiative forcing in regional and global climate modeling simulations (Lubin 2002; Turner 2008). The exclusion of IR scattering of mineral aerosols may lead to an underestimate of the IR radiative forcing both at the BOA (by 15%) and TOA (by 50%) (Dufresne et al. 2002). These facts underscore that the inclusion of accurate IR radiative forcing by the aerosols is vital to the climate models. Our findings have been validated by comparing outputs with the results published previously. In the meantime, two different case studies (smoky and dusty conditions) have shown that the LW radiative forcing by aerosols is highly sensitive to particle size and complex refractive indices of the aerosol constituents.

We have analyzed and quantified the effect of atmospheric humidity on the aerosol LW radiative forcings. It was found that the aerosol IR radiative forcing increases with decreasing atmospheric humidity. This finding supports our argument that the Great Basin in the USA, which usually has

extreme dry atmospheric conditions, can be an appropriate place to study the dry-aerosol climate forcing.

An analysis on the aerosol IR backscattering effect concludes that the effect significantly contributes to both the BOA and TOA IR forcings, even though the aerosols do not exhibit absorption at all in the thermal IR. The general aerosol LW radiative forcing is, therefore, associated with both the absorption and scattering effects of the aerosols. Neglecting aerosol LW scattering will result in an underestimation of LW radiative forcing of aerosols.

8.3 Future work

Our results likely possess a significant uncertainty owing to difficulties in accurate modeling of the aerosols and lack of aerosol properties in the LW region. Very few studies have been carried out in the field related to the topic of this dissertation. More intensive work is, therefore, required to have detailed information about the type, shape and size, and chemical and mineralogical composition of the local and regional aerosols, together with the refractive indices of the aerosol constituents, so that we can adequately characterize the aerosols and infer their LW radiative effects. Complete understanding of the regional aerosol LW radiative properties help us to incorporate our results into regional and global climate model simulations with confidence. As suggested by Sokolik et al. 1993, more accurate investigations are needed to account for the variability of aerosol optical properties, aerosol-cloud interactions, as well as aerosol feedbacks resulting from a changing climate itself, for a clearer understanding of how aerosols impact the climate.

Sea salt aerosols are one example of strongly scattering aerosol in the LW. Therefore the marine environment should be looked at closely for LW impacts by aerosols. Sea surface temperature obtained by IR sensing from satellite may be less accurate (biased low) in windy regions where rough seas may produce large amounts of sea salt aerosols.

REFERENCES

Adhikari, N., 2012: Ground-based remote sensing of the summer atmospheric boundary layer in Reno, Nevada, USA, using infrared spectroscopy, master's thesis, University of Nevada, Reno.

Air, D. S., 2014: In situ and remote sensing characterization of California wildfires and Nevada desert dust, Ph. D. dissertation, University of Nevada, Reno.

Arnott, W. P., Y. Y. Dong, and J. Hallett, 1994: Extinction efficiency in the infrared (2-18 micron) of laboratory ice clouds: Observations of scattering minima in the Christiansen bands of ice. *Applied Optics*, **34**, 541-551.

Baum, B. A., P. Yang, S. Nasiri, A. K. Heidinger, A. Heymsfield, and J. Li, 2007: Bulk Scattering Properties for the Remote Sensing of Ice Clouds. Part III: High-Resolution Spectral Models from 100 to 3250 cm^{-1}. *Amer. Meteor. Soc*., doi: 10.1175/JAM2473.1.

Bohren, C. F., and D. R. Hoffman, 1983: Absorption and Scattering of Light by Small Particles, Wiley, New York.

Clough, S. A., M. W. Shephard, E. J. Mlawer, J. S. Delamere, M. J. Iacono, K. Cady-Pereira, S. Boukabara, P. D. Brown, 2005: .Atmospheric radiative transfer modeling: a summary of the AER codes. *J. Quant. Spectrosc. Radiat. Transfer*, **91**, 233-244.

Clough, S. A., and M. J. Iacono, 1995: Line-by-line calculations of atmospheric fluxes and cooling rates: Application to carbon dioxide, ozone, methane, nitrous oxide, and the halocarbons. *J. Geophys. Res.*, **100**, 16, 519-16, 535.

Draxler, R., B. Stunder, G. Rolph, A. Stein, and A. Taylor, HYSPLIT 4 User's guide, version 4, May, 2013.

Dubovik, O., and M. D. King, 2000: A flexible inversion algorithm for retrieval of aerosol optical properties from Sun and sky radiance measurements. *J. Geophys., Res*., **105**, D16, 20, 673-20, 696.

Dubovik, O., B. Holben, T. F. Eck, A. Smirnov, Y. J. Kaufman, M. D. King, D. Tanré, and I. Slutsker, 2002: Variability of Absorption and Optical Properties of Key Aerosol Types Observed in Worldwide Locations. *J. of the Atmos. Sciences* **59**, doi:10.1175/1520-0469(2002)059<0590:VOAAOP>2.0.CO;2.

Dubovik, O., et al., 2006: The application of spheroid models to account for aerosol particle non-sphericity in remote sensing of desert dust. *J. Geophys. Res.*, **111**, D11208, doi: 10.1029/2005JD006619.

Dufresne, J.-L., C. Gautier, and P. Ricchiazzi, 2002: Longwave scattering effects of mineral aerosols. *Amer. Meteor. Soc.,* **59**, 1959-1966, 2002.

Eck, T. F., B. N. Holben, J. S. Reid, O. Dubovik, A. Smirnov, N. T. O'Neill, I. Slutsker, and S. Kinne, 1999: Wavelength dependence of the optical depth of biomass burning, urban, and desert dust aerosols. *J. Geophys. Res*., **104**, 24, 31, 333-31, 349.

Forster, P., V. Ramaswamy, and co-authors, 2007: Changes in Atmospheric Constituents and in Radiative Forcing. *In:Climate Change 2007*:The Physical Science Basis. Contribution of Working Group I to the Fourth Assessement Report of the Intergovernmental Panel on Climate Change [Solomon, S., and co-authors]. Cambridge University Press, Cambridge, United Kingdom and New York, NY, USA.

Fouquart, Y., B. Bonnel, G. Brogniez, J. C. Buriez, L. Smith, and J. J. Morcrette, 1987: Observations of Saharan aerosols: Results of ECLATS field experiment. Part II. Broadband radiative characteristics of the aerosols and vertical radiative flux divergence. *J. Climat. Appl. Meteor.*, **26**, 38-52.

Gao, B.-C., Y. J. Kaufman, and R. O. Green, 1995: Remote Sensing of Smoke, Clouds, and Fire Using A VIRIS Data N95-23860.

Ge, J. M., J. Su, T. P. Ackerman, Q. Fu, J. P. Huang, and J. S. Shi, 2010: Dust aerosol optical properties retrieval and radiative forcing over northwestern China during the 2008 China-U.S. joint field experiment. *J. Geophys. Res.* **115**, D00k12, doi:10.1029/2009JD013263.

Hansen, J. E., and L. D. Travis, 1974: Light scattering in planetary atmospheres. *Space Sci. Rev.*, **16**, 527-610.

Harrison, L., J. Michalsky, and J. Brendt, 1994: Automated multifilter rotating shadow-band radiometer: an instrument for optical depth and radiation measurements. *Appl. Opt*., doi: 10.1364/AO.33.005118.

Hodzic, A., S. Madronich, B. Bohn, S. Massie, L. Menut, and C. Wiedinmyer, 2007: Wildfire particulate matter in Europe during summer 2003: meso-scale modeling of smoke emissions, transport and radiative effects. *Atmos. Chem. Phys*., **7**, 4043-4064.

Holben, B. N., and coauthors, 1998: AERONET – A Federal instrument network and data archive for aerosol characterization. *Remote Sens. Environ*. **66**:1-16, Elsevier Science Inc.

IPCC, 2013: Summary for Policymakers. In: Climate Change 2013: The Physical Science Basis. Contribution of Working Group I to the Fifth Assessment Report of the Intergovernmental Panel on Climate Change [Stocker, T. F., D. Qin, G.-K. Plattner, M. Tignor, S. K. Allen, J. Boschung, A. Nauels, Y. Xia, V. Bex and P.M. Midgley (eds.)].Cambridge University Press, Cambridge, United Kingdom and New York, NY, USA.

Kasten, F. and A. T. Young, 1989: Revised optical air mass tables and approximation formula. *Appl. Optics* **28** (22), 4735-4738.

Levoni, C., M. Cervino, R. Guzzi, and F. Torricella, 1997: Atmospheric aerosol optical properties: a database of radiative characteristics for different components and classes. *Appl. Opt.,* **36**, 30, 8031-8041.

Lewis, K., W. P. Arnott, H. Moosmuller, and C. E. Wold, 2008: Strong spectral variation of biomass smoke light absorption and single scattering albedo observed with a novel dual-wavelength photoacoustic instrument. *J. Geophys. Res.,* **113**, D16203, doi:10.1029/2007JD009699.

Li, J., M. Posfia, P. V. Hobbs, and P. R. Buseck, 2003: Individual aerosol particles from biomass burning in southern Africa, 2. Composition and aging of inorganic particles. *J. Geophys. Res.*, **108**, doi:10.1029/2002JD002310.

Liao, H., and J. H. Seinfeld 1998: Radiative forcing by mineral dust aerosols: sensitivity to key variables. *J. Geophys., Res*., **103**, D24, 31, 637-31,645.

Liou, K. N., 1992: Radiation and Cloud Processes in the Atmosphere. Theory, Observation, and Modeling, Oxford University Press New York.

Lubin, D., S. K. Satheesh, G. McFarquar, and A. J. Heymsfield, 2002: Longwave radiative forcing of Indian Ocean tropospheric aerosol. *J. Geophys. Res.* **107***,* NO. D19, 8004, 10.1029/2001JD0001183.

Markowicz, K. M., P. J. Flatau, A. M. Vogelmann, P. K. Quinn, and E. J. Welton, 2003: Clear-sky infrared aerosol radiative forcing at the surface and the top of the atmosphere. *Q. J. R. Meteorol. Soc*., **129**, 2927-2947.

Martins, J. V., P. V. Hobbs, R. E. Weiss, and P. Artaxo,1998: Sphericity and morphology of smoke particles from biomass burning in Brazil. *J. Geophys. Res.*, **103**, 32,051-32,057.

Mitchell, D. L., W. P. Arnott, C. Schmitt, A. J. Baran, S. Havemann, Q. Fu, 2001: Photon tunneling contributions to extinction for laboratory grown hexagonal columns. *J. Quant. Spectrosc. Radiat. Transfer*, **70**, 761-776.

Petty, G. W., 2006: A first course in Atmospheric Radiation, second edition, Sundog Publishing.

Raymond M. Hoff and Sundar A. Christopher, 2009: Remote sensing of Particulate Pollution from Space: Have We Reached the Promised Land? *J. Air waste Management Assoc*., **59**, 645-675.

Reid, J. S., T. F. Eck, S. A. Christopher, P. V. Hobbs and B. Holben,1999: Use of the Angstrom exponent to estimate the variability of optical properties of aging smoke particles in Brazil. *J. Geophys. Res.*, **104**, 473-489.

Remer, L. A., Y. J. Kaufman, B. N. Holben, A. M. Thompson, and D. McNamara, 1998: Biomass burning aerosol size distribution and modeled optical properties. *J. Geophys. Res*., **103**, D24, 31, 879-31, 891.

Rothman, L. S., and coauthors, 2009: The HITRAN 2008 molecular spectroscopic database. *J. Quant. Spectrosc. Radiat. Transfer*, **110**, 533-572.

Rothman, L. S., and coauthors, 2005: The HITRAN 2004 molecular spectroscopic database. *J. Quant. Spectrosc. Radiat. Transfer*, **96**, 139-204.

Sayer, A. M., A. Smirnov, N. C. Hsu, and B. N. Holben, 2012: A pure marine aerosol model, for use in remote sensing applications. *J. Geophys. Res*., **117**, D05213, doi:10.1029/2011JD016689.

Sayer, A. M., N. C. Hsu, T. F. Eck, A. Smirnov, and B.N. Holben, 2013: AERONET-based microphysical and optical properties of smoke-dominated aerosol near source regions and transported over oceans, and implications for satellite retrievals of aerosol optical depth. *Atmos. Chem. Phys. Disscuss.*, **13**, 25013-25065.

Schuster, G. L., O. Dubovok, and B. N. Holben, 2006: Angstrom exponent and bimodal aerosol size distribution. *J. Geophys Res*. III, D07207, doi:10.1029/2005JD006328.

Seinfeld, J. H., and S. N. Pandis, 2006: Atmospheric Chemistry and Physics, second edition, AWiley-Interscience Publication, John Wiley & Sons, INC.

Sicard, M., S. Bertolin, M. Mallet, P. Dubuisson, and A. Comeron, 2014: Estimation of mineral dust longwave radiative forcing: sensitivity study to particle properties and application to real cases over Barcelona. *Atmos. Chem. Phys. Discuss*., **14**, 8533-8573.

Sicard, M., S. Bertolin, M. Mallet, P. Dubuisson, and A. Comeron, 2013: Estimation of a radiative transfer model in the longwave spectral range: sensitivity study and application to real cases, Remote Sensing of Clouds and the Atmosphere XVIII; and Optics in Atmospheric Propagation and Adaptive Systems XVI. *Proc. SPIE* vol. **8890** 88900L-1.

Sokolik, I. N., and O. B. Toon, 1999: Incorporation of mineralogical composition into models of the radiative properties of mineral aerosol from UV to IR wavelengths. *J. Geophys. Res.,* **104**, D8, 9423-9444.

Sokolik, I. N., and O. B. Toon, 1996: Direct radiative forcing by anthropogenic airborne mineral aerosols, *Nature*. **381**.

Sokolik, I. N., and G. Golitsyn, 1993: Investigation of Optical and radiative properties of atmospheric dust aerosols. *Atmos. Environment*, **27A**, 16, 2509-2517.

Stamnes, K., S.-C. Tsay, W. Wiscombe, and K. Jayweera, 1998: A numerically stable algorithm for discrete-ordinate-method radiative transfer in multiple scattering and emitting layered media. *Appl. Opt*., **27**, 2502-2509.

Sun, H., Z. Rong, C. Liu, J. Liu, Y. Zhang, P. Zhang, X. Wang, and W. Gao, 2006: Spectral characteristics of infrared radiation from forest fires, *Proc. SPIE.*, 6298, 629808-1.

Tegen, I. and A. A. Lacis, 1996: Modeling of particle size distribution and its influence on the radiative properties of mineral dust aerosol. *J. Geophys. Res.,* **19**, 237-244.

The Michelson series FTIR spectrometer user's guide 1994 Bomem, Inc., quebec, Canada.

Turner, D. D., 2008: Ground-based infrared retrievals of optical depth, effective radius, and composition of airborne mineral dust above the Sahel. *J. Geophys. Res.,* **113**, D00E03, doi:10.1029/2008JD010054.

Turner, D. D., 2005: Arctic mixed-phase cloud properties from AERI lidarobservations: Algorithm and results from SHEBA. *J. Appl. Meteor.,* **42**, 701-715.

Turner, D. D., 2003: Microphysical properties of single and mixed-phase Arctic clouds derived from ground-based AERI observations. Ph.D. thesis, University of Wisconsin-Madison, 167 pp. [Available online at http://www.sscc.wise.edu/library/turnerdissertation.pdf.]

Urbanski, S. P., W. M. Hao, and S. Baker, 2009: Chemical composition of wildland fire emissions. *Develop. Environ. Sc.,* 8, Doi:10.1016/S1474-8177(08)00004-1.

Vogelmann, A. M., P. J. Flatau, M. Szczodrak, K. M. Markowicz, and P. J. Minnett, 2003: Observations of large aerosol infrared forcing at the surface. *Geophys. Res. Lett.*, **30**(12), 1655, doi: 10.1029/2002GL016829, 2003.

Vries., P. J. Jr., 1969: Analysis of Forest Fire Smoke Using Satellite Imagery, Master's thesis, March 1989, NAVAL Postgraduate school, Monterey, California.

Wang, J., S. A. Christopher, U. S. Nair, J. S. Reid, E. M. Prins, J. Szykman, and J. L. Hand, 2006: Mesoscale modeling of Central American smoke transport to the United States: 1. "Top-down" assessment of emission strength and diurnal variation impacts. *J. Geophys. Res*., **111**, D05S17, doi:10.1029/2005JD006416.

Wendisch, M., P. Yang, and P. Pilewskie, 2007. Effects of ice crystal habit on thermal IR radiative properties and forcing of cirrus. *J. Geophys. Res*., **112**, D08201, doi:10.1029/JD007899.

Whitby, K., 1978, The physical characteristics of sulfur aerosols, *Atmos. Environ*., **12**, 135-159.

Yang, P., and coauthors, 2007: Modeling of the scattering and radiative properties of nonspherical dust-like aerosols. *J. Aeros. Sc.* **38**, 995-1014.

Yang, P., Q. Feng, G. Hong, G. W. Kattawar, W. J. Wiscombe, M. I. Mishchenko, O. Dubovik, I. Laszlo, and I. N. Sokolik, 2007: Modeling of the scattering and radiative properties of nonspherical dust-like aerosols. *Aeros. Sc.*, **38**, 995-1014.

Yang, P., H. Wei, H.-L. Huang, B. A. Baum, Y. X. Hu, G. W. Kattawar, M. I. Mishchenko, and Q. Fu, 2005: Scattering and Absorption property database for nonspherical ice particles in the near-through far-infrared spectral region. *Appl. Optics*, **44**, No.26.

Zender, A., 2010: Particle Size Distributions: Theory and Application to Aerosols, Clouds, and Soils, University of California, Irvine (Available at http://dust.ess.uci.edu/facts).

APPENDIX A: AN ANALYSIS ON ERRORS OF FTIR MEASUREMENT

This section presents the FTIR-observed radiance sensitivity to the emissivity and temperature of the cold and hot blackbodies, and other possible sources of error in FTIR measurement. The results of the sensitivity study are displayed in Fig. A.1.

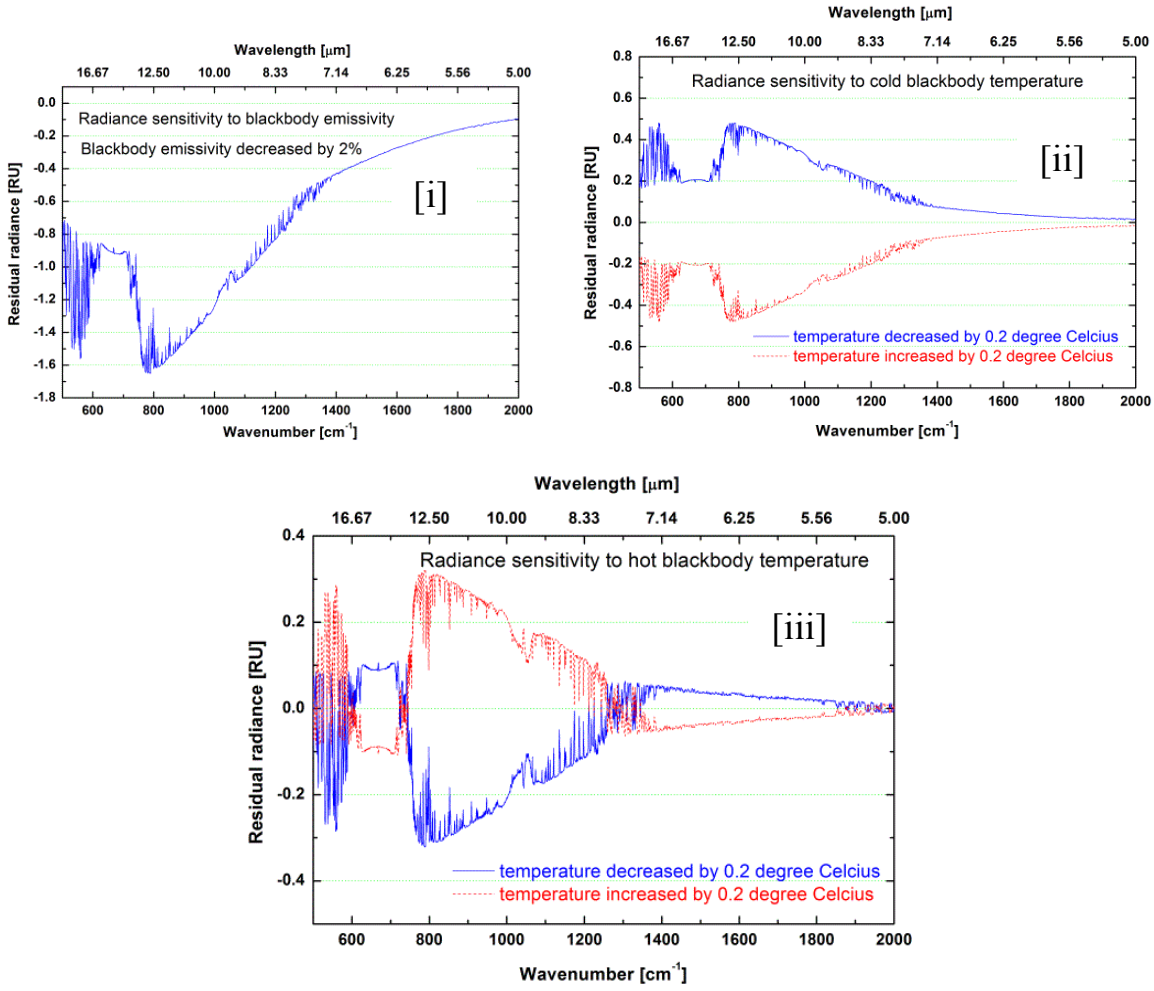

Figure A.1 FTIR-observed radiance sensitivity to: (i) blackbody emissivity (ii) cold blackbody temperature, and (iii) hot blackbody temperature. The emissivity was decreased by 2% from one. The temperatures were changed from a reference value by ± 0.20°C, the thermistor accuracy, for each blackbody. The radiance unit 'RU' is 1 mW/(m^2 Sr cm^{-1}).

The results represent the difference (or residual) radiance between the radiance obtained with some given value of the blackbody emissivity (or temperature) and the radiance obtained with the adjusted value of the emissivity (or temperature) of the blackbodies, as indicated in each plot. The emissivity of each blackbody was reduced by 2 % from the original value of one (Fig. A[i]). Each blackbody temperature was changed by ± 0.20°C, the thermistor accuracy, (Fig. A[ii], for cold blackbody, and Fig. A[iii], for hot blackbody). The blue solid curve and red dashed curve, in both plots [ii] and [iii], indicate the residual radiances corresponding to temperature difference of - 0.2°C and + 0.2°C, respectively.

We can draw the following conclusions based on Fig. A.1: First, the radiance is sensitive to both emissivity and temperature of the blackbodies. Second, the radiance sensitivity is different in different spectral regions. For example, the IR window region (8-13 μm) shows the strongest sensitivity while the 6.3 μm band shows the least sensitivity in the measured 5-20 μm region. Third, the radiance is more sensitive to the cold blackbody temperature than hot blackbody temperature. Finally, the values of the sensitivity look small, but not ignorable.

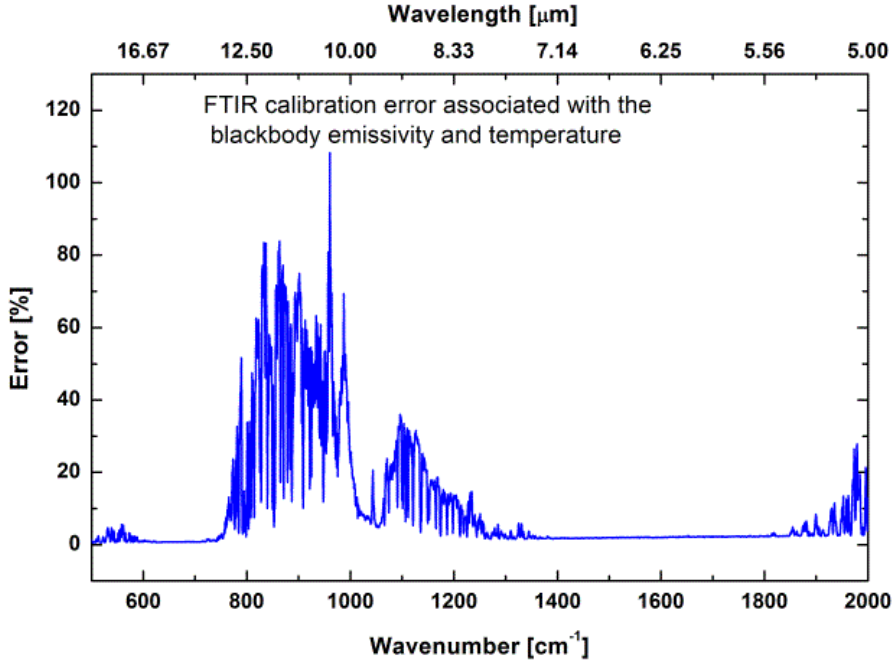

Figure A.2 FTIR calibration error in percentage.

Fig. A.2 depicts the FTIR calibration error in percentage, which was obtained by combining the errors due to blackbody emissivity and temperatures i.e.

$$\text{error}[\%] = \frac{100}{R(\nu)}\left(\Delta^2_{\text{emissivity}} + \Delta^2_{CBB} + \Delta^2_{HBB}\right)^{\frac{1}{2}}$$

where $\Delta_{\text{emissivity}}$ is the error due to 2% decrease in the blackbody emissivity, Δ_{CBB} is the error due to 0.2°C increase in cold blackbody temperature, and Δ_{HBB} is the error due to 0.2°C increase in hot blackbody temperature. $R(\nu)$ is the original radiance value. The error is as high as 108% in the window region, and is mostly contributed by error in the emissivity.

The non-linear response of the detector voltage to the target radiance (as opposed to our assumption of the linear response) and wavenumber dependency of the blackbody emissivity (we have used a fixed value of emissivity for all wavenumbers) can be other inherited sources of error in the instrument. In addition, the liquid-nitrogen-cooled detector may not be cold enough to be able to respond very weak signals from extremely cold targets. The FTIR measurements are, therefore, erroneous, at least, due to these issues. The uncertainties help us approximate the amplitude of the error bars present in the measurement. We performed sensitivity studies only for the emissivity and temperature because these are the principal observable sources of errors in the instrument.

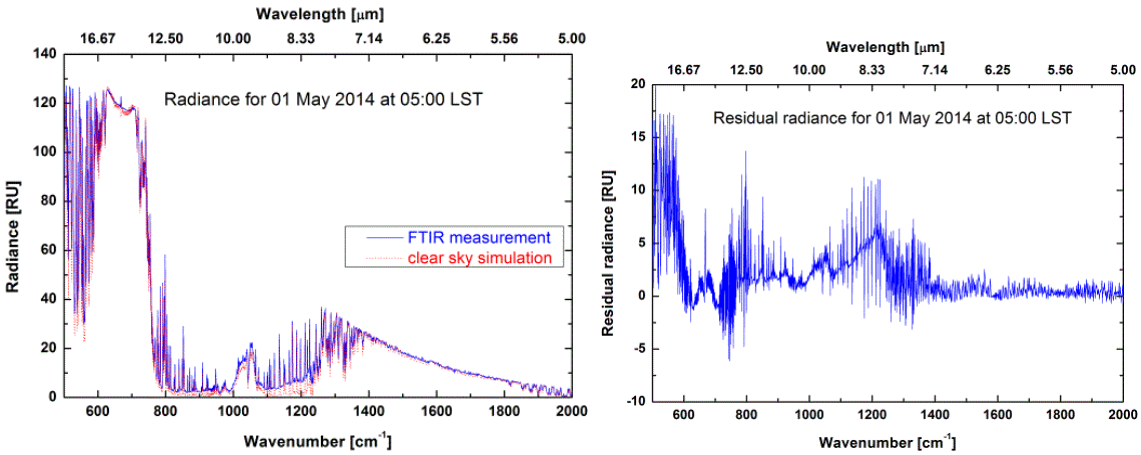

Figure A.3 FTIR measurement vs. clear sky simulation for 01 May 2014 at 05:00 LST (left) and (measurement-simulation) residual radiance (right).

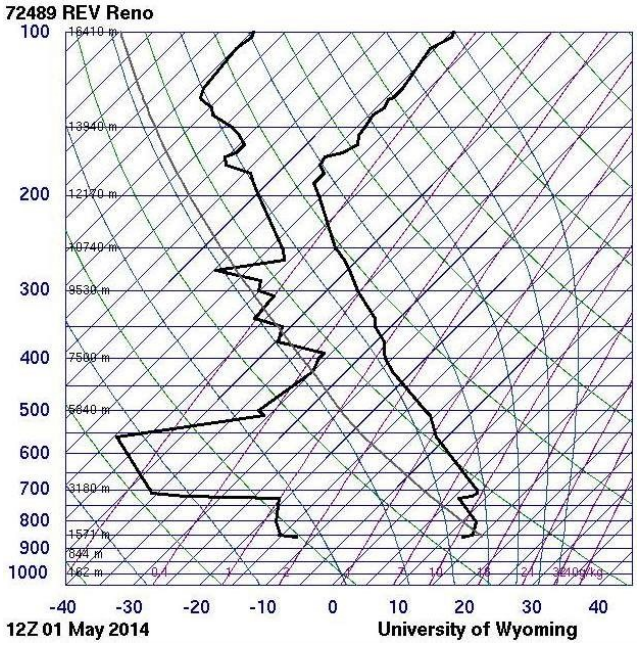

Figure A.4 Reno's sounding for 01 May 2014 at 05:00 LST with precipitable water of 2.55 mm.

Fig. A.3 (left) shows the radiance measurement with FTIR and simulation with LBLRTM (left) for a clear day (01 May 2014 at 05:00 LST). The simulation used the sounding profile of Fig. A.4 which has a precipitable water (PW) of 2.55 mm. The residual radiance between the FTIR measurement and LBLRTM simulation is shown in Fig. A.3 (right). The residual is caused by various factors as discussed in section 5.1 along with the uncertainties just mentioned.

In order to see if the fractional difference between the radiances calculated with and without aerosols is larger than the FTIR calibration error, we overlaid Fig. A. 2 on the theoretical fractional radiance plot calculated for 24 April 2014 at 08:00 LST, a typical day in Reno (Fig. A.5) using the following equation:

$$\text{fractional radiance} = \frac{|R_{\text{aerosol}} - R_{\text{without aerosol}}|}{R_{\text{without aerosol}}} \times 100$$

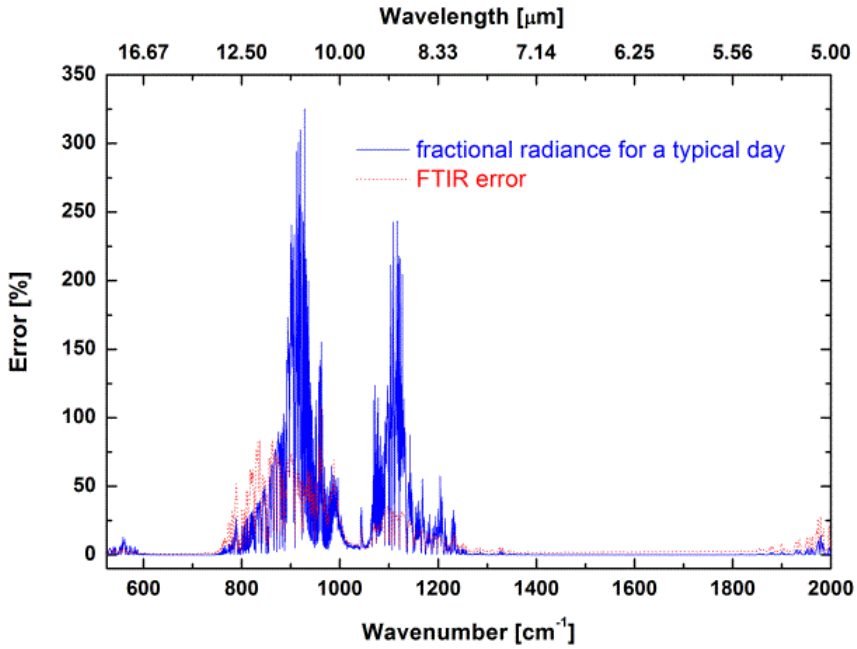

Figure A.5 FTIR calibration error (red dotted curve) of Fig. A.2 is overlaid on the fractional radiance plot for our typical day of 24 April 2013 at 08:00 LST (blue solid curve), both are expressed in percentage.

Since the fractional radiance is larger than the FTIR calibration error for most of the wavenumbers in the IR window region, the instrument can detect the fractional radiance by aerosol on typical days. FTIR calibration error also depends on the atmospheric conditions such as relative humidity. This is because the sensitivity of the photo-detector depends on the strength of the signal from the atmosphere, especially in the window region. A very moist atmosphere has less error than a very dry atmosphere. Similarly, the fractional radiance is also less for a moist atmosphere than for a dry atmosphere. These facts suggest that the FTIR calibration error must be calculated separately for each measurement.